Acta Polytechnica

Editorial Board:

Zdeněk P. Bažant
Northwestern University McCormick School of Engineering, Illinois, USA

Lenka Bodnárová
Brno University of Technology, Czech Republic, Czech Republic

Steffen Bohrmann
Hochschule Mannheim University of Applied Sciences, Germany

Reinhard Harte
Department of Civil Engineering, Bergische Universität, Wuppertal, Germany

Taťána Jarošíková
Faculty of Biomedical Engineering, Czech Technical University in Prague, Czech Republic

Jitka Jírová
Faculty of Transportation Sciences, Czech Technical University in Prague, Czech Republic

Petr Jizba
Faculty of Nuclear Sciences and Physical Engineering, Czech Technical University in Prague, Czech Republic

Pavel Kalina
Faculty of Architecture, Czech Technical University in Prague, Czech Republic

Tomáš Kozik
Department of Technology and Information Technologies, Constantine the Philosopher University in Nitra, Slovakia

František Kraus
ETH Zürich, Switzerland

Libor Makovička
Université de Franche Comté, France, France

Zuzana Masáková
Faculty of Nuclear Sciences and Physical Engineering, Czech Technical University in Prague, Czech Republic

David Murray-Smith
School of Engineering, University of Glasgow, United Kingdom

Drahomír Novák
Faculty of Civil Engineering, Brno University of Technology, Czech Republic

Marián Peciar
Institute of Chemical and Hydraulic Machines and Equipment (FME), Slovak University of Technology in Bratislava, Slovakia

Jan Píchal
Faculty of Electrical Engineering, Czech Technical University in Prague, Czech Republic

Miroslav Sýkora
Klokner Institute, Czech Technical University in Prague, Czech Republic

Zbyněk Škvor (Head of Editorial Board)
Faculty of Electrical Engineering, Department of Electromagnetic Field, Czech Technical University in Prague, Czech Republic

Radek Šulc
Faculty of Mechanical Engineering, Czech Technical University in Prague, Czech Republic

Martin Vohralík
INRIA de Paris, Institut universitaire de technologie, France

Pavel Trtik
Paul Scherrer Institut (PSI), Villigen, Switzerland, Switzerland

Jan Zeman
Faculty of Civil Engineering, Czech Technical University in Prague, Czech Republic

Title of journal: Acta Polytechnica. **Volume:** 62. **Number:** 5.
Periodicity: Bimonthly; 6 issues per year. **Date of issue:** October 31, 2022.
Published by: Czech Technical University in Prague,
Jugoslávských partyzánů 1580/3, 160 00 Praha 6 – Dejvice, Czech Republic.
IČO: 68407700.

Editorial Office: CTU — Central Library,
Technická 6, 160 80 Praha 6, Czech Republic.
`acta@cvut.cz`

Acta Polytechnica is available at `http://ojs.cvut.cz/ojs/index.php/ap`
Each article is assigned a digital object identifier `https://doi.org/10.14311/AP.2022.62.`⟨*4-digit article page number*⟩

ISSN 1805–2363 (online) MK ČR E 4923

Dear Reader

The Acta Polytechnica journal that you have just opened is a scientific journal published by the Czech Technical University in Prague. This journal first appeared in 1961 under the name "Proceedings of the Czech Technical University". The main purpose of the journal was to support publication of the results of scientific and research activities at the Czech technical universities. Five years later, in 1966, the name of the journal was changed to Acta Polytechnica, and it started appearing quarterly. The main title Acta Polytechnica is accompanied by the subtitle Journal of Advanced Engineering, which expresses the scope of the journal more precisely. Acta Polytechnica covers a wide spectrum of engineering topics in civil engineering, mechanical engineering, electrical engineering, nuclear sciences and physical engineering, architecture, transportation science, biomedical engineering and computer science and engineering. The scope of the journal is not limited to the realm of engineering. We also publish articles from the area of natural sciences, in particular physics and mathematics.

Acta Polytechnica is now being published in an enlarged format. Our aim is to be a high-quality multi-disciplinary journal publishing the results of basic research and also applied research. We place emphasis on the quality of all published papers. The journal should also serve as a bridge between basic research in natural sciences and applied research in all technical disciplines.

We invite researchers to submit high-quality original papers. The conditions of the submission process are explained in detail on: `http://ojs.cvut.cz/ojs/index.php/ap`. All papers will be reviewed, and accepted papers are published in English.

We hope that you will find our journal interesting, and that it will serve as a valuable source of scientific information.

Editorial Board

Contents

Acta Polytechnica **62**(5):498–504, 2022
`https://doi.org/10.14311/AP.2022.62.0498`

Published by the `Czech Technical University in Prague`

LOW EARTH ORBIT NANOSATELLITE: INFLUENCE OF HEAT DISSIPATION ON PASSIVE THERMAL ANALYSIS

Amine Akka[a,*], Farid Benabdelouahab[a], Randa Yerrou[b]

[a] *Abdelmalek Essaadi University, Department of Physics, Laboratory of physics and condensed matter, BP. 2121 M'Hannech II. 93030 Tetouan, Kingdom of Morocco*

[b] *Abdelmalek Essaadi University, Department of Physics, ERSN Laboratory, BP. 2121 M'Hannech II. 93030 Tetouan, Kingdom of Morocco*

[*] corresponding author: `a_akka@hotmail.com`

Abstract.

The use of small satellites in ambitious missions presents challenges related to thermal breakdowns as one of the critical issues contributing to their failure. Heat dissipation and thermal management are still the major challenges in nanosatellite systems design. To meet the thermal stability requirements, it becomes statutory to manage passive and active thermal control to reach this goal while a variety of factors, such as high-powered components, sunlight and shadow on orbit, or a tight spacecraft layout, remain imposed.

A spherical nanosatellite thermal analysis was performed to show the effect of energy dissipation in a low earth orbit and the stability of the system with a special attention to batteries, which persist as the weak link among electronics parts. Additionally, a set of different material coatings was used to demonstrate their impact on the nanosatellite's thermal behaviour, hence highlighting their importance while designing such a spacecraft.

Keywords: Nanosatellite, thermal stability, material coatings, heat dissipation, passive thermal control.

1. Introduction

Satellites have always been developed to capitalise on the advantages that provide on all levels of weather monitoring, scientific observation, communication, remote sensing, and surveillance. The novelty with nanosatellites is that these favours are acquired at minimal costs [1–4]. Table 1 [5] clearly shows the benefits of the nanosatellite approach as compared to the traditional satellite approach when designing each satellite.

The need for a better thermal control on nanosatellites with temperature-sensitive components on-board requires many adjustments before launching. A simple shape of nanosatellites will narrow the range of temperatures experienced by internal components, and also outer irradiance coming from the Sun and the Earth if absorptance α and emissivity ϵ, which are the primary means of passive thermal control, are well-chosen, depending on the material used [8–14].

The objective is to sustain the temperature of all subsystems within their operating range. As each part of the satellite is coupled to the structure by conduction, the internal temperature is fairly uniform.

Therefore, the design of the thermal control system depends on the strictest temperature range, namely the batteries [$0\,^\circ$C, $40\,^\circ$C] [15] and operating electronic equipment [$-15\,^\circ$C, $50\,^\circ$C] [16].

The purpose of this paper is to establish a passive thermal analysis to ensure optimal operating conditions for inner components of a spherical nanosatellite, namely by keeping the temperature within the specified limits. The thermal analysis has been carried out with simulation tools based on the finite element approach for various coating materials, with consideration of heat dissipation in steady state conditions and, then also in nominal conditions. Obtained results were very promising, as, in outer space, the possibilities offered by a passive or even active thermal control should be considered to overcome the difficulties encountered, in particular for the sensitive parts of nanosatellites.

2. Materials and methods

2.1. Space thermal environment

The space environment in Figure 1 is very complicated and erratic; therefore, the simulation concerns modelling two extreme cases: The hot case, and the cold case. As their name indicate, those describe the most serious situations where thermal loads are relevant as indicated in Table 2 [17]. Since the orbit is Sun-synchronous [18] and circular at a 400-km altitude "98.13° inclination" with spacecraft pointing-earth, the β angle that determines the time during which the spacecraft is exposed to direct sunlight remains almost constant. When considering the Earth and its atmosphere as a whole, the calculation of the rate of absorption of solar energy, and the terrestrial infrared radiation emission averaged over a certain time

Design approach	**Mission flexibility**	**System performance**	**Risk tolerance**	**Development time**	**Cost**	**System focus**
Traditional/military	Low	High	Low	High	High	Performance
Traditional/commercial	Low	High	Low	High	High	Profit
Traditional/experimental	Low	High	Medium	Medium	High	Science
Nanosatellites	Medium	Low	Medium	Medium	Medium	Cost

Table 1. Comparison of traditional and, nanosatellite design approaches.

Parameters	**Cold Case**	**Nominal Case [6]**	**Hot Case**
Incident Solar Flux [W m^{-2}]	1317 Summer Solstice	1367	1419 Winter Solstice
Albedo Factor	0.22 at $\beta = 0°$	0.28	0.59 at $\beta = 90°$
Earth IR [W m^{-2}]	217	242	261
Heat dissipation [W] [7]	6.594	–	22.438
Temperature and Pressure		Vacuum at 2.7 K	

Table 2. Chosen conditions for simulation purposes.

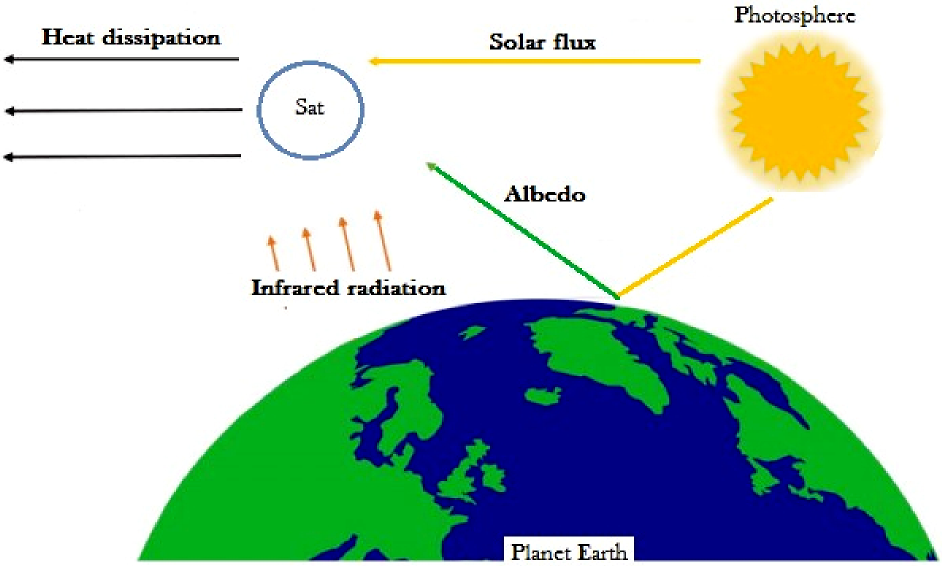

Figure 1. Nanosatellite heat exchange.

interval may unfold the radiative balance of the Earth with the Sun and outer space [19].

In low Earth orbit (LEO), the altitude is less than the diameter of the Earth and satellites can only see a small part of the Earth at any given time. This means that the conditions will change dramatically as the satellites move through different combinations of environments. These changes must be given priority in the design of the thermal control satellite system.

2.2. THERMAL ANALYSIS

The primary objective of the thermal analysis is to ensure the preservation of the satellite's internal components within the specified temperature threshold, especially batteries as mentioned earlier. The steady-state thermal analysis, performed for the nanosatellite in Figure 2, is governed by the equation:

$$A_{sat} \times \epsilon \times \sigma \times T^4 = Q_{sun} + Q_{alb} + Q_{ear} + Q_{int}, \quad (1)$$

where on the left side of Eq. (1), A_{sat} [m^2] is the satellite's total area emitting radiation, which has the same external area as a Cubesat of 10 cm × 10 cm × 10 cm, ϵ [-] is the emissivity, σ [W m^2 K^{-4}] is the Stephan-Boltzmann constant and T [K] is the temperature required, however, on the right side Q_{sun} [W] is the heat input from the solar radiation, Q_{alb} [W] is the heat input from the Albedo radiation, Q_{ear} [W] is the heat transferred due to Earth Infrared, and

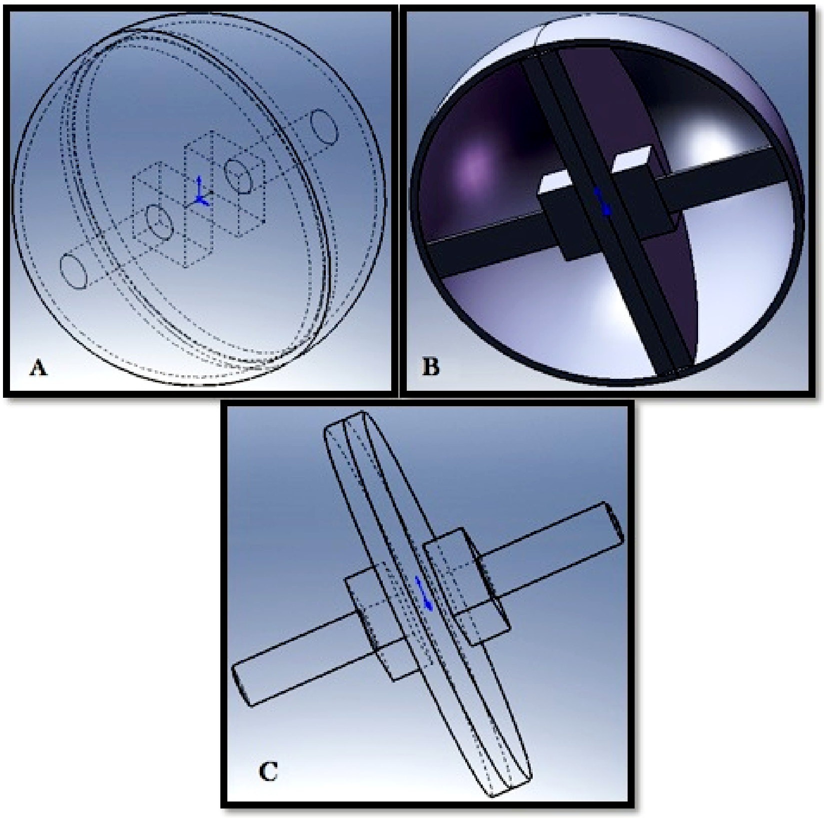

Figure 2. A: Panoramic view, B: Front plane section view, C: Inside view.

Q_{int} [W] is the nanosatellite internal heat load, which refers to the dissipated energy from the electronic components and batteries.

At this stage of analysis, the absorptivity factor α can't be remarked in Eq. (1), yet, dissecting Q_{sun}, Q_{alb}, and Q_{ear} terms clearly shows the impact of the absorptivity on the equilibrium balance. As a matter of fact, the three quantities are defined as follows, Eqs. (2), (3) and (4):

$$A_{sun} \cdot \alpha \cdot J_s = Q_{sun}, \tag{2}$$

where A_{sun} is the projected area receiving solar radiation, α is the absorptance factor, and J_s is the solar constant.

$$A_{alb} \cdot \alpha \cdot J_{alb} = Q_{alb}, \tag{3}$$

where A_{alb} is the projected area receiving albedo radiation, and J_{alb} is the intensity of the albedo radiation.

$$A_{ear} \cdot \epsilon \cdot J_{ear} = Q_{ear}, \tag{4}$$

where A_{ear} is the projected area receiving earth radiation, and J_{ear} is the intensity of the planetary infrared radiation.

As it can be seen in Figure 2, the main component of the nanosatellite, almost totally made of aluminium alloys, is a disc panel, where different electronic cards may be installed, and which is not dissipating power in the upcoming simulation. The disc panel is mounted in the equator enclosed by batteries, the most power-dissipating elements, that are supported by a double tube in the axis of spinning.

Coating	$\boldsymbol{\alpha}$	$\boldsymbol{\epsilon}$
Black Body	1	1
White Paint V200	0.26	0.89
Black Paint H322	0.96	0.86
Brilliant Aluminum Paint	0.70	0.13
Buffed Aluminum	0.16	0.03
Blue Anodised Titanium Foil	0.30	0.31

Table 3. Used coatings for the nanosatellite [23].

It is always accurate to process a perfect thermal, mechanical and electrical design of useful loads at the very beginning of the design process to avoid anomalies that may occur due to the details of the payload packaging. Indeed, there are many challenges that engineers face when designing a spacecraft, namely thermal ones that have made the subject of several research papers for the optimisation of such an analytical approach [20] and even experimental testing [21].

The passive thermal analysis, shown in Table 3, concerned multiple coating materials, in extreme conditions with heat dissipation, but also in nominal conditions with no heat dissipation as mentioned in Table 2. The temperature is calculated by finite element code in accordance with all the boundary conditions [22].

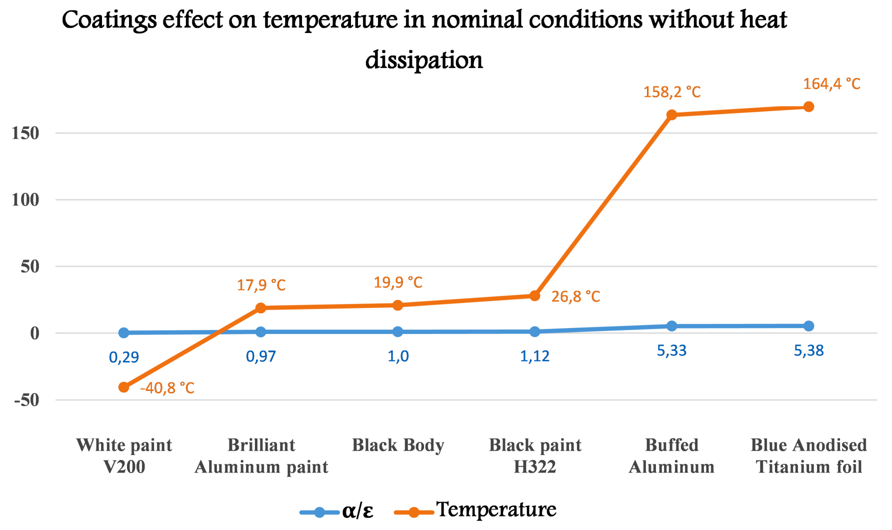

Figure 3. Coating effect on temperature in nominal conditions.

Coating	$\frac{\alpha}{\epsilon}$	**Temp [°C]**
White Paint V200	0.292	−40.8
Brilliant Aluminum Paint	0.967	17.9
Black Body (No coating)	1	19.9
Black Paint H322	1.116	26.8
Buffed Aluminum	5.333	158.2
Blue Anodised Titanium foil	5.384	164.4

Table 4. Temperatures in nominal conditions without heat dissipation.

Coating	$\frac{\alpha}{\epsilon}$	**Min Temp [°C]**	**Max Temp [°C]**
White Paint V200	0.292	13.4	15.4
Brilliant Aluminum Paint	0.967	55.1	57.0
Black Body (No coating)	1	56.7	58.7
Black Paint H322	1.116	62.4	64.3
Buffed Aluminum	5.333	186.5	188.3
Blue Anodised Titanium foil	5.384	186.8	188.6

Table 5. Min and Max temperatures for cold case simulation.

3. Results and discussion

3.1. Nominal case results

Referring to the temperature of the batteries, which should remain within the predefined ranges to maintain the proper functioning of the nanosatellite, we hardly notice that, under the nominal working conditions (Table 4 and Figure 3), three of the six coatings meet the above condition and allow the batteries' to run at acceptable temperatures, namely [17.887 °C, 19.901 °C, 26.848 °C].

For all the results obtained, the temperature of the batteries was the highest and the simulation made it possible to clearly identify the problem and try to start on a good basis when proposing solutions. All these coatings have an $\frac{\alpha}{\epsilon}$ ratio around unity.

For the report of the other coatings, it is obvious that other passive thermal controls should be considered, namely heat-conducting elements, adiabatic spacers, modifying the geometry of the spacecraft, or even active thermal control, but one must keep in mind that the latter should only be used when it is impossible to meet the requirements.

3.2. Cold case results

For the cold case simulation, Table 5 and Figure 4, it is clear that "White paint V200" perfectly follows the temperature required for the proper functioning of the nanosatellite, the three ratios of coatings that follow need only a complement of passive control to fall within the optimal operating temperature range of the batteries. However, for "Buffed Aluminum and Blue Anodised Titanium" coatings, an active thermal control is required because the temperatures have exceeded the limits.

3.3. Hot case results

Finally, for the hot case, Table 6 and Figure 5, the obtained results show that under the conditions defined at the outset, a temperature exceeding 200 °C is reached, and therefore another type of coating material must be applied in addition to an active thermal control to decrease the temperatures and ensure optimal operating conditions for the spacecraft.

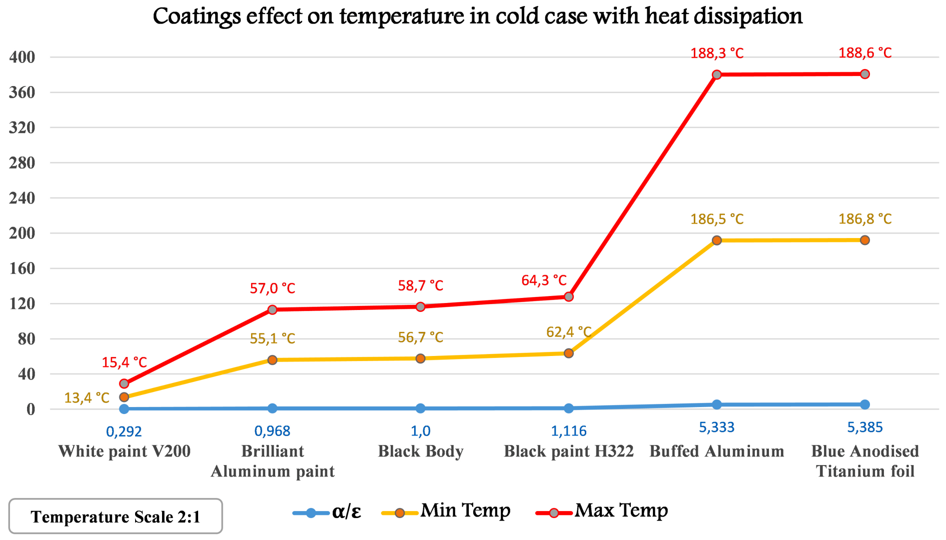

Figure 4. Coating effect on temperature in cold case conditions with heat dissipation.

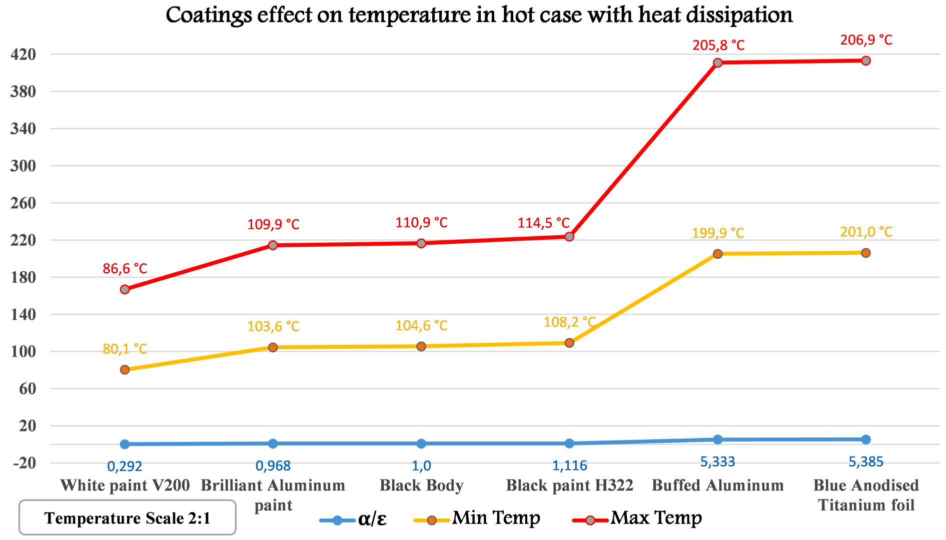

Figure 5. Coating effect on temperature in hot case conditions with heat dissipation.

Coating	$\frac{\alpha}{\epsilon}$	Min Temp [°C]	Max Temp [°C]
White Paint V200	0.292	80.1	86.6
Brilliant Aluminum Paint	0.967	103.6	109.9
Black Body (No coating)	1	104.6	110.9
Black Paint H322	1.116	108.2	114.5
Buffed Aluminum	5.333	199.9	205.8
Blue Anodized Titanium foil	5.384	201.0	206.9

Table 6. Min and Max temperatures for hot case simulation.

3.4. Batteries issues

As it can be seen in Figure 6 and Figure 7 taken from a cold and a hot analysis, the main cause of the high gradient of temperature is the battery “In red”, It is noteworthy that for an operational nanosatellite in the harsh conditions of the outer space, one should think about using all possibilities offered by passive thermal control, or even active thermal one, to overcome the encountered difficulties.

In addition to this, we can undoubtedly notice that the temperature distribution at the level of the different elements of the nanosatellite is almost the same in both extreme cases [24].

It is important to remind that only the dissipation of heat caused by the batteries has been involved, yet if other major parameters are involved in the system with the complexity of their heat dissipation, results will vary greatly.

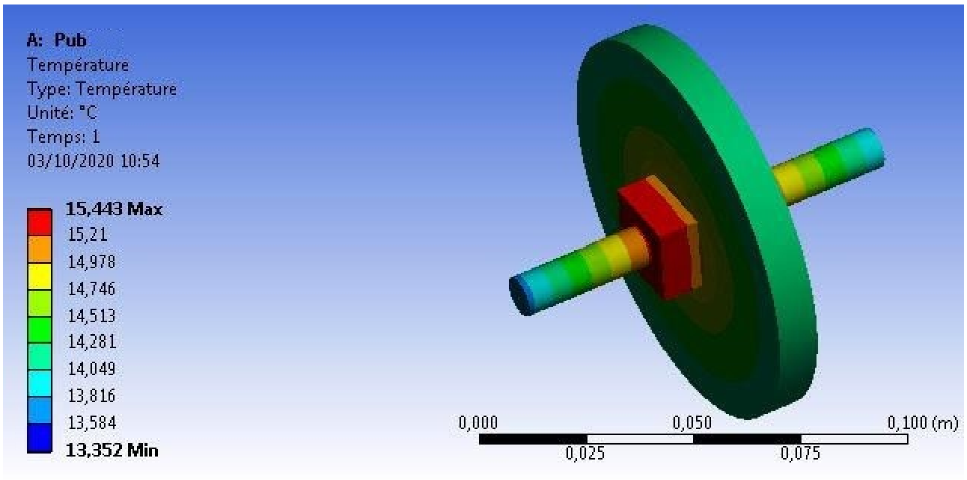

Figure 6. Cold case internal temperature distribution $\frac{\alpha}{\epsilon} = 0.29$.

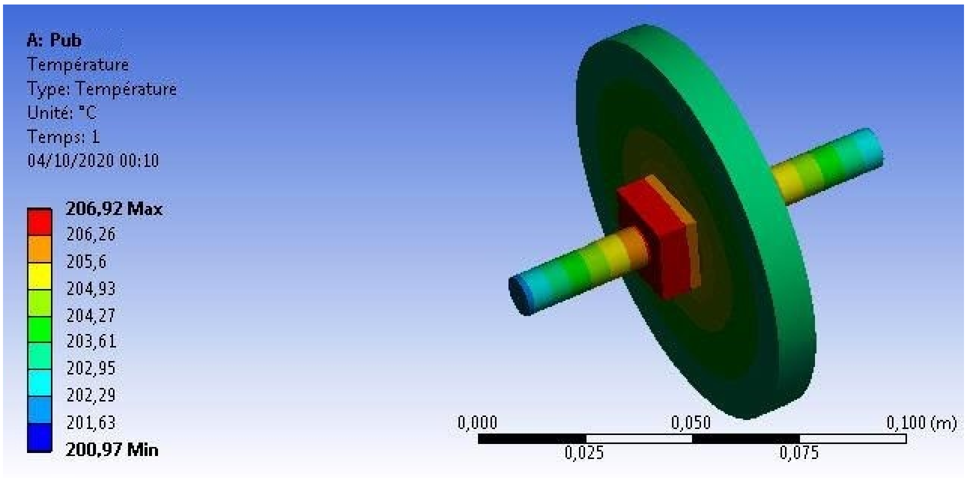

Figure 7. Cold case internal temperature distribution $\frac{\alpha}{\epsilon} = 5.38$.

4. Conclusions

Consistent design criteria for the development and comparison of several material coatings associated with heat dissipation parameters were presented. This paper went through a passive thermal analysis of a simply designed spherical nanosatellite. Indeed, it was assumed that the design provided has shown the effect of batteries' heat dissipation which imposed some changes in temperature plots. Even though, there is an extensive range of material coatings that can offer various $\frac{\alpha}{\epsilon}$ ratios, practical selection of the type of coating is often limited by the ageing characteristics. That's why one should think about using all the offered possibilities by finite element codes even those of active thermal control, which can be the subject of an extensive research study and may serve as an additional resolution tool for the current space revolution. An extended study must be performed to gauge the viability of that kind of thermal control, which may improve the quality and then the stability of that kind of nanosatellite.

List of symbols

α	Absorptivity [–]
β	Beta Angle [°]
ϵ	Emissivity [–]
σ	Stephan-Boltzmann constant $[\mathrm{W\,m^{2}\,K^{-4}}]$
T	Temperature [K]
Q_{sun}	Heat input from the solar radiation [W]
Q_{alb}	Heat input from the Albedo radiation [W]
Q_{ear}	Heat transferred due to Earth Infrared [W]
Q_{int}	Nanosatellite dissipated energy [W]
A_{sat}	Satellite total area emitting radiation $[\mathrm{m^2}]$
A_{sun}	Projected area receiving solar radiation $[\mathrm{m^2}]$
A_{alb}	Projected area receiving albedo radiation $[\mathrm{m^2}]$
A_{ear}	Projected area receiving earth radiation $[\mathrm{m^2}]$
J_s	Solar constant $[\mathrm{W\,m^{-2}}]$
J_{alb}	Intensity of the Albedo radiation $[\mathrm{W\,m^{-2}}]$
J_{ear}	Intensity of the planetary infrared radiation $[\mathrm{W\,m^{-2}}]$

References

[1] K. Woellert, P. Ehrenfreund, A. J. Ricco, H. Hertzfeld. Cubesats: Cost-effective science and technology platforms for emerging and developing nations. *Advances in Space Research* **47**(4):663–684, 2011. `https://doi.org/10.1016/j.asr.2010.10.009`.

[2] B. M. Kading, J. Straub, R. Marsh. Openorbiter mechanical design: A new approach to the design of a 1-U CubeSat. In *53rd AIAA Aerospace Sciences Meeting*. 2015. `https://doi.org/10.2514/6.2015-1835`.

[3] M. H. Heidt, J. Puig-Suari, A. S. Moore, et al. CubeSat: A new generation of picosatellite for education and industry low-cost space experimentation. In *14th Annual AIAA/USU Conference on Small Satellites*, SSC00-V-5. 2000. `https://digitalcommons.usu.edu/smallsat/2000/All2000/32`.

[4] J. Berk, J. Straub, D. Whalen. The open prototype for educational nanosats: Fixing the other side of the small satellite cost equation. In *2013 IEEE Aerospace Conference*, pp. 1–16. 2013. `https://doi.org/10.1109/AERO.2013.6497393`.

[5] D. W. Hengeveld, J. E. Braun, E. A. Groll, A. D. Williams. Hot- and cold-case orbits for robust thermal control. *Journal of Spacecraft and Rockets* **46**(6):1249–1260, 2009. `https://doi.org/10.2514/1.44468`.

[6] B. Anderson, C. Justus, G. Batts. Guidelines for the selection of near-Earth thermal environment parameters for spacecraft design. NASA Technical Memorandum. Accessed 30-09-2020, `https://ntrs.nasa.gov/citations/20020004360`.

[7] K. E. Boushon. *Thermal analysis and control of small satellites in low Earth orbit*. Master's thesis, Missouri University of Science and Technology, 2018.

[8] J. Vojta, S. Zuik, V. Baturkin, et al. Thermocontrol system concept of magion small subsatellites of interball mission. *Acta Astronautica* **39**(9):971–976, 1996. `https://doi.org/10.1016/S0094-5765(97)00083-0`.

[9] A. Akka, F. Benabdelouahab. Passive thermal analysis of a cubesat by a finite element modeling. *JP Journal of Heat and Mass Transfer* **21**(21):133–149, 2020. `https://doi.org/10.17654/HM021010133`.

[10] A. Akka, F. Benabdelouahab, R. Yerrou. Evaluating the temperature toggling of a nanosatellite through a preliminary passive thermal analysis. *JP Journal of Heat and Mass Transfer* **24**(2):383–391, 2021. `https://doi.org/10.17654/0973576321011`.

[11] A. Akka, F. Benabdelouahab. Nanosatellite: A progressive vision of performing passive thermal control. In *AIP Conference Proceedings*. In press.

[12] V. Baturkin. Micro-satellites thermal control–concepts and components. *Acta Astronautica* **56**(1-2):161–170, 2005. `https://doi.org/10.1016/j.actaastro.2004.09.003`.

[13] K. Badari Narayana, V. Venkata Reddy. Thermal design and performance of HAMSAT. *Acta Astronautica* **60**(1):7–16, 2007. `https://doi.org/10.1016/j.actaastro.2006.07.001`.

[14] S. Corpino, M. Caldera, F. Nichele, et al. Thermal design and analysis of a nanosatellite in low earth orbit. *Acta Astronautica* **115**:247–261, 2015. `https://doi.org/10.1016/j.actaastro.2015.05.012`.

[15] V. Knap, L. K. Vestergaard, D.-I. Stroe. A review of battery technology in cubesats and small satellite solutions. *Energies* **13**(16):4097, 2020. `https://doi.org/10.3390/en13164097`.

[16] P. Fortescue, G. Swinerd, J. Stark. *Spacecraft systems engineering*. John Wiley & Sons, Ltd., Chichester, UK, 2011.

[17] J. R. Wertz, D. F. Everett, J. J. Puschell. *Space Mission Engineering: The New SMAD*. Microcosm Press, Hawthorn, CA, 2011.

[18] R. J. Boain. A-B-Cs of sun-synchronous orbit mission design. In *14th AAS/AIAA Space Flight Mechanics Meeting*, AAS 04-108. 2004. Accessed 02-11-2020, `http://hdl.handle.net/2014/37900`.

[19] P. Walimbe, S. Padekar. Evolutionary insights into the state-of-the-art passive thermal control systems for thermodynamic stability of smallsats. *Advanced Engineering Forum* **35**:29–45, 2020. `https://doi.org/10.4028/www.scientific.net/AEF.35.29`.

[20] J. Young, S. Inlow, B. Bender. Solving thermal control challenges for CubeSats: Optimizing passive thermal design. In *2019 IEEE Aerospace Conference*, pp. 1–7. 2019. `https://doi.org/10.1109/AERO.2019.8741754`.

[21] J. Liu, M. Li, Q. Gao. Micro satellite thermal balance testing: Orbit heat flux simulation method and verification. *MATEC Web of Conferences* **54**:09001, 2016. `https://doi.org/10.1051/matecconf/20165409001`.

[22] A. Akka, F. Benabdelouahab, R. Yerrou. Nanosatellite case study: Issue of heat dissipation across passive thermal analysis. *E3S Web of Conferences* **336**:00057, 2022. `https://doi.org/10.1051/e3sconf/202233600057`.

[23] J. H. Henninger. Solar absorptance and thermal emittance of some common spacecraft thermal-control coatings. Tech. rep., National Aeronautics and Space Adminitration, Scientific and Technical Information Branch, 1984.

[24] A. Akka, F. Benabdelouahab, R. Yerrou. Nanosatellite on-low-Earth-orbit temperature simulation and its implication concerning extreme cases. In *AIP Conference Proceedings*. In press.

Acta Polytechnica **62**(5):505–521, 2022
https://doi.org/10.14311/AP.2022.62.0505

THE ENGINEERING PERFORMANCE OF ECO-FRIENDLY CONCRETES CONTAINING DIATOMITE FLY ASH AND GROUND GRANULATED BLAST FURNACE SLAG

Hüseyin Yilmaz Aruntaş[a], Erkan Yildiz[b], Gökhan Kaplan[c,*]

[a] *Gazi University, Faculty of Technology, Department of Civil Engineering, 06500 Ankara ,Turkey*
[b] *Eslem Consulting Engineering and Trade Limited Company, 06824 Ankara, Turkey*
[c] *Atatürk University, Faculty of Engineering, Department of Civil Engineering, 25030 Erzurum, Turkey*
[*] corresponding author: gkaplan@atauni.edu.tr

Abstract. Approximately 10 % of CO_2 is emitted from an ordinary Portland cement production. In cement and concrete production, CO_2 emissions can be greatly reduced by using Supplementary Cementitious Materials (SCMs). In addition, the microstructure and durability properties of concrete are greatly improved when silica-rich SCMs are used. In this study, Eco-Friendly concrete design was carried out using three different SCMs. Diatomite, ground granulated blast furnace (GGBFS) and fly ash (FA) were used as the SCM in the concrete mixtures. SCMs were used instead of cement at ratios of 5, 10, 15, and 20 wt%. When diatomite was used at the rate of 20 %, the standard consistency water increased 1.7 times as compared to the reference mixture. With the increase in the replacement ratio, the final setting times of the pastes increased. The high active SiO_2 content of diatomite shortened the initial setting time and increased the compressive strength. The use of 5 % diatomite reduced the slump value by 57 % as compared to the reference mixture. The slump and Ve-Be tests of GGBFS and FA mixtures showed similar properties to the reference mixture. The 28-day compressive strength of concrete varied between 29.2–34.6 MPa. With the increase in the curing time of the concrete mixtures, up to 50 % improvements were observed in the compressive strength. Especially on the 180th day, a compressive strength of 44.1 MPa was obtained in concrete mixtures with a 10 % replacement ratio. While using the FA in the mixtures improved the abrasion properties, the opposite result was observed in the case of the GGBFS. It was observed that the mixtures with 5 % FA showed the closest properties to the reference mixture. As a result, it was determined that SCMs with different properties could be used in environmentally friendly concrete mixtures by up to a 20 % replacement ratio.

Keywords: Sustainability, diatomite, fly ash, ground granulated blast furnace slag, eco-friendly concrete.

1. INTRODUCTION

The three basic elements of built environment sustainability are resource conservation, life cycle costing (LCC), and human-friendly designs (HFD). In terms of resource conservation, the 3Rs (Reduce, Reuse, and Recycle) idea is currently widely used in the construction and manufacturing sectors [1]. Because of its durability and architectural freedom, concrete is the most important building material on the planet [2]. According to The Concrete Centre, the amount of embedded CO_2 (ECO_2) in concrete is a consequence of the cement content in mixtures [3]. Concrete has an ECO_2 impact of approximately 100 kg CO_2 per tonne. The embodied CO_2 content of concrete is taken into account in building a sustainable concrete structure [2]. Furthermore, it is generally known that the manufacturing of Portland cement is a polluting process, accounting for about 5-9 percent of global anthropogenic carbon dioxide emissions [4]. In 2016, 4200 million metric tons of cement were produced worldwide, according to the reports [5]. Furthermore, the production of Portland cement is an energy-intensive process that accounts for 10–15 percent of total global industrial energy use [6]. The industry adopted alternatives to balance the environmental impacts connected with the production of Portland cement and, consequently, concrete, to reduce the environmental footprint and costs [7]. Using Supplementary Cementitious Materials (SCM) in cement and concrete production is one of the most important methods. Supplementary Cementitious Materials (SCMs), such as Ground Granulated Blast Furnace Slag (GGBFS), Pulverized fly ash (PFA), Rice Husk Ash (RHA), Silica Fumes (SF), can be used to minimise the embodied CO_2 of the concrete. Over the last few decades, SCMs have been widely used in concrete manufacturing. However, sustainability is the main purpose of using SCMs in concrete and cement production. With the use of SCMs, CO_2 emissions will decrease and more sustainable structures can be designed. The advantages of utilizing SCM may include improved mechanical qualities, decreased porosity, permeability, adverse reactions, and other physical properties like pigmentation [8, 9].

The steel industry produces millions of tons of slag as a by-product [10, 11]. By-products account for about 50 % of all steel manufacturing [12]. 294 kg of slag is produced from 1 ton of liquid pig iron [13]. This slag is divided into three categories based on its origin and cooling method (air, water, or water + pressure). The GGBFS is created when the slag formed during the fabrication of pig iron is quickly cooled and powdered to be utilised as a binder by the Portland cement industry [13]. It is known that 530 million tons of GGBFS are released worldwide and only 65 % of it is used [14, 15]. The production of one ton of GGBFS generates just 70 kg of CO_2, which is only 7 % of the pollution created by cement [16]. GGBFS, a by-product of steelmaking, is often stored in landfills. Because of the stiffening of environmental restrictions, the disposing of GGBFS has become a complex and costly operation. GGBFS usually contains significant levels of silicon dioxide (SiO_2), aluminium oxide (Al_2O_3), calcium oxide (CaO), and other materials that allow it to be utilised in the concrete preparation process [17]. Studies are showing that many properties are improved by adding GGBFS to concrete. GGBFS has a slower hydration rate than ordinary Portland cement. As a result, the early hydration heat release of concrete containing GGBFS is typically lower, indicating that GGBFS could significantly improve early thermal cracking resistance [17]. In addition, GGBFS increases the sulphate resistance as it reduces the permeability of the concrete [18]. GGBFS is used to partially replace cement, is often very fine, and has a glassy texture. Because of the small size and glassy surface, less water is required to provide the necessary workability of fresh concrete [19, 20]. However, because GGBFS has a lower density than PC, replacing an equal quantity of cement with GGBFS results in a higher paste volume (about 10 %), significantly improving segregation resistance and flowability [21]. In terms of durability, GGBFS may improve resistance to chloride ion diffusion, maybe because the GGBFS improves pore size distribution and more C-S-H gels are generated, adsorbing more chloride ions and blocking the diffusing path [22].

Fly ash (FA) is a by-product of coal-fired thermal power plants frequently utilized as a supplemental cementitious material (SCM) in the concrete industry as a cement alternative [23]. While 450 million tons of FA is released worldwide, only 25 % of it is disposed of [24]. Thermal power plants in Turkey produce almost 15×10^6 tons of FA per year. One of the major issues with power plants is storing the FA or its removal from the facilities. As a result, the harmful consequences of waste FAs on the ecosystem should be studied [25]. FA is classified as an artificial pozzolan. The research was advanced because suitable volumes of FA were utilised in place of concrete. Numerous studies on FA have been published [26]. FA is beneficial in reducing CO_2 emissions in the cement and concrete industry. Furthermore, the pozzolanic reaction between FA and cement improves the long-term durability and strength of the concrete, making FA a popular mineral addition [27, 28]. Improved FA replacement ratios in concrete result in a higher use efficiency. However, the replacement ratio cannot be too high [29, 30]. For example, EN 197–1:2000 specifies a maximum of 35 percent FA [31]. Many authors have shown that a replacement of 40–60 % FA can result in a high strength development, good resistance to alkali-silica reaction, freezing, thawing, chloride ion penetration, sulphate attack, and water permeability [32–36]. It has also been reported to lower the hydration heat and the risk of thermal cracking [37]. However, due to the perception of enhanced surface scaling, the performance of FA (with high volume) concrete in applications where deicing salts are used is a concern [38]. Bouzoubaa et al. have shown that FA concretes generally have equal or higher mechanical and durability performance to concrete without FA, the exception being inferior salt-scaling resistance of the FA content [39]. Concrete containing FA is shown to carbonate faster than concrete without FA [40]. It has also been stated that FA reduces chloride ion permeability and increases corrosion resistance [41].

Bacillariophyceae are a family of single-celled aquatic algae known as diatoms [42]. Diatomite, made up of their skeletons, is a refined sedimentary deposit almost entirely made up of silica and is utilised in mortars and grouts [43]. Diatomite is a soft, siliceous rock with abrasive properties, low density, and high porosity crushed into white powder. Diatomite is formed from the remains of microscopic single-celled algae (diatoms) found in marine sediments. Dead fossilized diatoms can be found at the bottom of oceans, sea beds, and lakes [44]. Diatomaceous accumulations can be found in many countries around the world, including the United States (particularly in California), the Commonwealth of Independent States (USSR), Canada, South Korea, Romania, Belgium, Japan, Brazil, Denmark, Germany, the Isle of Man, South Africa, Mediterranean countries of Algeria, Italy, France, Turkey, Crete, Cyprus, Spain, and Morocco [45]. The Canadian market (17.900 t/year), Germany (12.000 t/year), Belgium (6.200 t/year), South Africa (4.600 t/year), and Russia (4.300 t/year) are the primary export markets. These five countries accounted for almost half of all stated exports, or 47 percent. Diatomite is used in many ways after being treated and calcined. Water, agro-food sugars, oils, table fats, and other chemical products are filtered with it [45]. One of the different uses of diatomite is in the cement and concrete industry. Diatomite is utilised as an additive, since it has been proved that its reactive silica concentration and high Blaine values can improve the mechanical characteristics [46]. It was proved that diatomite could be used as an enhancement component in cement [47]. This is performed by its capacity to improve paste cohesion and hence reduce segregation. This could be due to

	Cement (OPC)	Diatomite	GGBFS	FA
CaO	62,72	0,73	30,28	12,31
SiO_2	20	87,27	37,65	45,25
Fe_2O_3	3,76	0,5	0,54	6,75
Al_2O_3	4,92	2,64	12,36	11,17
MgO	1,84	0,29	16,55	12,16
Na_2O	0,26	0,00	0,59	4,12
K_2O	0,73	0,25	0,88	1,84
SO_3	2,65	0,07	0,45	3,68
LOI*	2,54	1,27	1,2	1,2
Insoluble residue	0,4	5,34	0,3	0,25
Specific gravity	3,02	2,01	2,97	2,27
Specific surface area**	3220	4470	2400	3378
Initial setting time [min]	150	-	-	-
Final setting time [min]	220	-	-	-

*Loss on ignition

**Blaine method [cm^2/g]

Table 1. Properties of cement and SCMs.

residual negative charges on the diatomite's surface, resulting in enhanced dispersion [42]. Various studies have examined the potential and interest of using it in cement, mortar, and concrete in the form of diatomite powder. Değirmenci and Yılmaz suggested that diatomite can be used instead of cement at a rate of 5 % [48]. Li et al. investigated green concrete's early-age behaviour, mechanical characteristics, and environmental effects with diatomite and limestone as a cement clinker replacement [49]. In their study, Xiao and Liu showed that diatomite reduces the thermal conductivity coefficient [50]. Using calcined diatomite improves the mechanical and microstructural properties of high-strength mortars at ambient and high temperatures, according to Saridemir et al. [51]. In the later stages of cement hydration, diatomite can significantly increase the amount of C-S-H. (28 days). Calcined diatomite solves the problem of strength reduction [52]. As a result, many studies suggest using different SCMs to reduce CO_2 emissions in cement and concrete production [53–58].

In this study, different supplementary cementitious materials (SCM) were used to improve concretes' mechanical and abrasion properties. Alternative materials in concrete are discussed to provide various options that contribute to a more sustainable concrete. In this context, diatomite, GGBFS, and FA were used in the Eco-Friendly concrete mixtures. FA and GGBFS stored in landfills are very dangerous for human and environmental health. The easiest and cheapest disposal method is their use in concrete production. The disposal of these waste products will reduce environmental pollution. If diatomite is used in concrete production, cement consumption will decrease. The decrease in cement consumption causes CO_2 emissions to decrease and more sustainable building material being produced. Within the study's scope, the effectiveness of concretes with relatively lower CO_2 emissions were investigated. Therefore, SCMs were added to the concrete at different replacement ratios, and their fresh, hardened, and abrasion properties were investigated.

2. EXPERIMENTAL MATERIALS AND METHODS

2.1. MATERIALS

Type 1 cement (ordinary Portland cement-OPC) conforming to ASTM C150 [60] standard was used in the experimental study. Diatomite, GGBFS, and FA were used as SCMs in the mixtures. FA was obtained from Çayırhan Thermal Power Plant in Ankara/Nallıhan region. Since the CaO content of FA is more than 10 %, it is in class C according to ASTM C618 [61]. GGBFS conforming to ASTM C989 standard was obtained from KARDEMİR facilities [62]. Diatomite was obtained from the Çankırı-Çerkeş region (Figure 1). Since diatomite (natural pozzolana) is different from other SCMs, SEM studies were performed (Figure 2). It can be seen that the particle size of diatomites vary between 5-50 µm and is generally smaller than 10 μm. A wide variety is observed in the shapes of the diatomite particles. These include pipe, long fish, strainer comb (toothbrush), and round shapes. The chemical and physical properties of cement and SCMs are presented in Table 1. Figure 3 shows the XRD patterns of SCMs.

A limestone aggregate conforming to ASTM C33 [63] standard was used to prepare the mixtures. The particle size of the fine aggregate is 0–4 mm, and

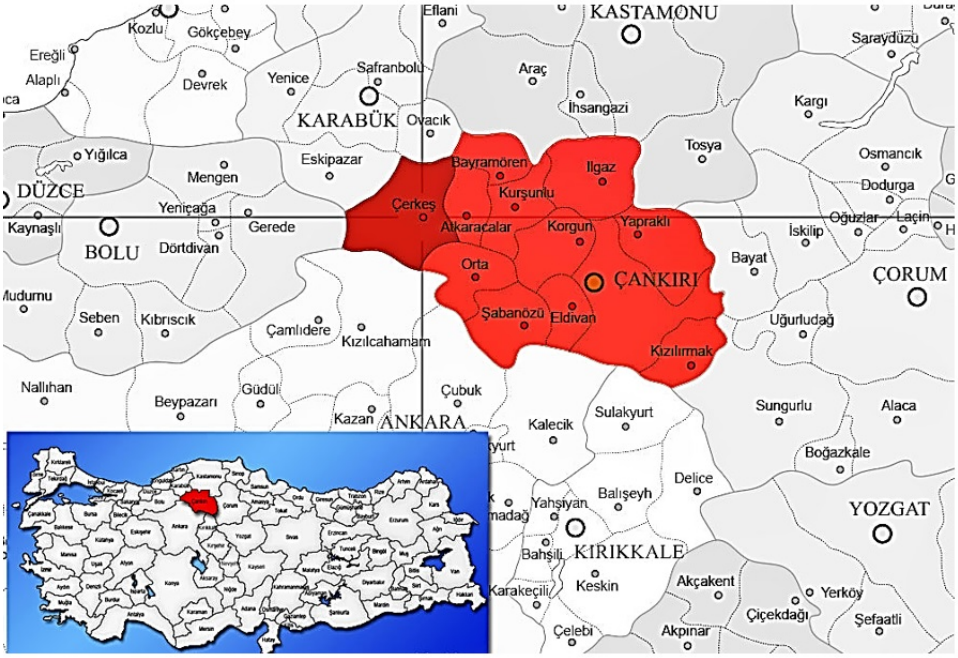

Figure 1. Region of diatomite reserves.

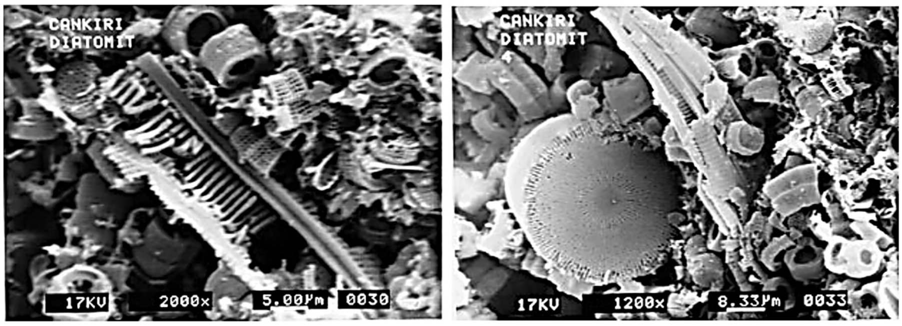

Figure 2. SEM image of the diatomite [59].

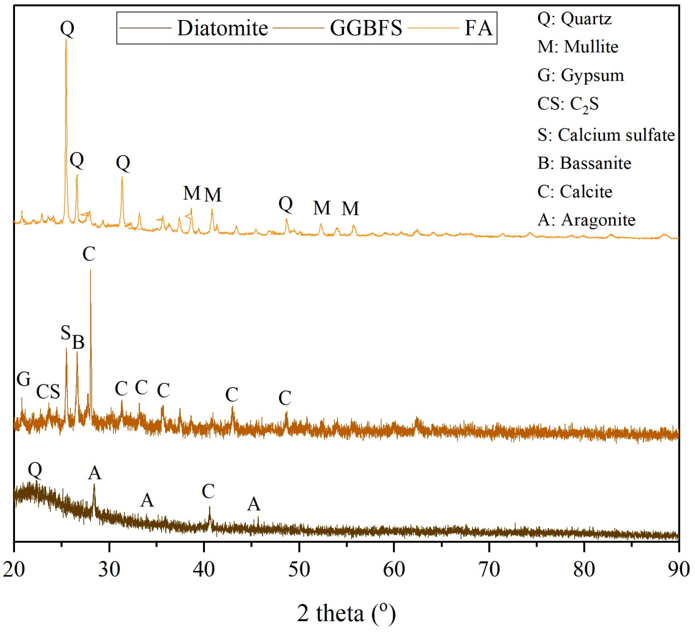

Figure 3. XRD patterns of SCMs.

	Mixture properties		Material quantities [kg/m^3]						
Mix ID	SCM	Replacement ratio [%]	Coarse aggregate	Fine Aggregate	Water	Cement	Diatomite	GGBFS	FA
M1	Reference	0	834.9	1070.5	167.0	315.0	-	-	-
M2	Diatomite	5				299.3	15.7	-	-
M3		10				283.5	31.5	-	-
M4		15				267.8	47.2	-	-
M5		20				252.0	63.0	-	-
M6	GGBFS	5				299.3	-	15.7	-
M7		10				283.5	-	31.5	-
M8		15				267.8	-	47.2	-
M9		20				252.0	-	63.0	-
M10	FA	5				299.3	-	-	15.7
M11		10				283.5	-	-	31.5
M12		15				267.8	-	-	47.2
M13		20				252.0	-	-	63.0

Table 2. Concrete mix proportions.

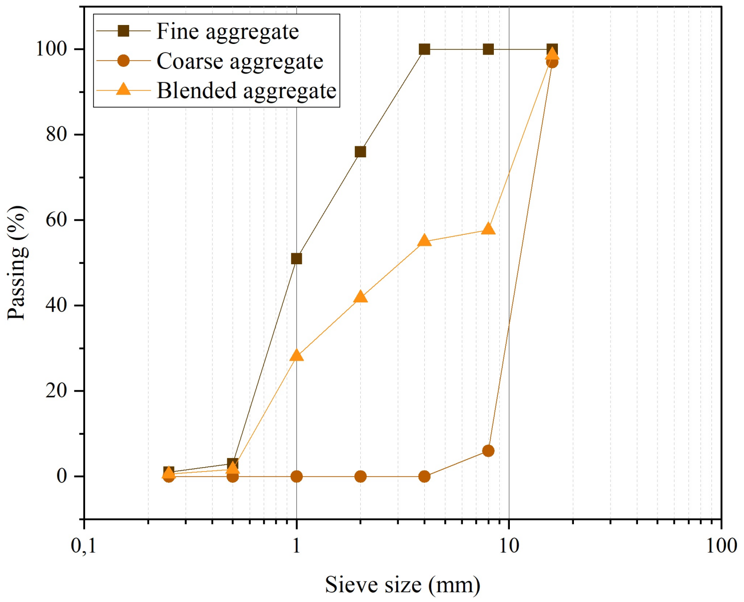

Figure 4. Sieve analysis of aggregates.

the coarse aggregate is 4–16 mm. The fine aggregate's specific gravity and water absorption values are 2.71 and 0.77, respectively. The coarse aggregate's specific gravity and water absorption values are 2.72 and 0.71, respectively. The particle distributions of the aggregates are given in Figure 4. The aggregates do not contain any organic matter. Potable water was used in the mixtures. Diatomite and GGBFS were ground in a ball mill until cement fineness was reached.

2.2. Mixture proportions

The ratios of concrete mixes were determined according to the TS 802 (Concrete Mixing Calculation Principles) standard. In the study, all concretes kept the w/c ratio (0.50) constant. The cement dosage was determined as 315 kg/m^3. The concrete class was chosen as C25/30 according to EN 206 standard [64]. SCMs were used in place of cement with four different replacement ratios. SCMs were used at the rate of 5, 10, 15, and 20 % instead of cement (by weight). Since the C25/30 class was the target in the concrete design, SCMs were not used at very high rates. Mixture properties and material amounts are given in Table 2. Concrete mixes were prepared in a vertical shaft mixer with a volume of 40 dm^3. The mixture was stirred for 1 minute in dry form and another 4 minutes after adding water. After the mixing was completed, fresh concrete experiments were carried out and the concrete was placed in pre-cleaned and oiled moulds. Compaction was done using an im-

Figure 5. Abrasion test and general view of samples.

mersion vibrator. The samples were removed from the mould after 24 hours and cured in a water tank with a temperature of 20 ± 1 °C until the day of the experiment.

2.3. Methods

2.3.1. Setting time, consistency, and soundness test

A Hobart mixer was used to mix all pastes at 140 RPM for 2 minutes and 285 RPM for 2 minutes. The physical properties of the cement were determined according to the EN 196-3 [65] standard. Vicat plunger and needle were used for the standard consistency water and setting time of the pastes. The volume expansion of the pastes was determined by the Le-Chatelier method.

2.3.2. Fresh properties

According to ASTM C 143 [7] standard, the slump test determined the mixtures' fresh properties. The fresh concrete was poured into the slump cone in 3 layers. With a standard 16 mm diameter rounded steel rod, each layer was tamped 25 times. After the slump, the cone was pulled up and the concrete was expected to collapse. The slump value of the concrete was measured with a ruler. The Ve-Be test of the concretes was carried out according to the TS EN 12350-3 standard [66]. The air content of fresh concrete was determined according to ASTM C231 [67], wet bulk density was determined according to ASTM C138 standard [68].

2.3.3. Compressive strength

The uniaxial compressive stress is reached when a material fails the compressive strength test. Compressive strengths of concretes were determined in 100 mm × 100 mm × 100 mm cube samples according to the ASTM C39 standard [69]. Concrete specimens were tested for compressive strength at 28, 90, and 180 days of curing. In each case, a set of three cubes was tested, and the average value of these three was reported.

2.3.4. Abrasion resistance

The abrasion depth of concrete mixes was determined according to the ASTM C944 standard [70]. The abrasion depth was measured in cube samples of 100 mm × 100 mm × 100 mm. In addition, the abrasion depth was tested on 28-, 90-, and 180-day concrete mixes. In this way, the effect of different curing times on the pozzolanic activity was also observed. The depth of abrasion was determined after 6 minutes of testing. The device used in the abrasion test and the samples exposed to the abrasion are given in Figure 5.

3. Results and discussion

3.1. Physical properties of cement

As seen in Figure 6a, the standard consistency water of the reference mixture was determined as 27.1 %. AS Compared to the reference mixture, the standard consistency of water increased to about 4 % using FA and GGBFS. However, the increase in diatomite content led to a larger variation in the standard consistency of water. While the standard consistency water of cement using 5 % diatomite increased by 26.2 %, the standard consistency water of cement using 20 % diatomite increased by 69.7 %. The fact that the diatomite had a porous structure increased the standard consistency of water. Furthermore, the diatomite has a higher specific surface area than other SCMs. Therefore, the addition of diatomite significantly increased the standard consistency of water. The standard consistency of water increased negligibly in the case of FA and GGBFS. Although the specific surface area of FA is higher than that of cement, the standard consistency of water did not increase as much. The reason for this is explained by the fact that FA, generally, has a spherical particle structure. The specific surface area of GGBFS is approximately 25 % lesser than cement's. However, the GGBFS relatively increased the standard consistency of water, because the particle shape of GGBFS has an angular structure like limestone. The angular structure of GGBFS required a

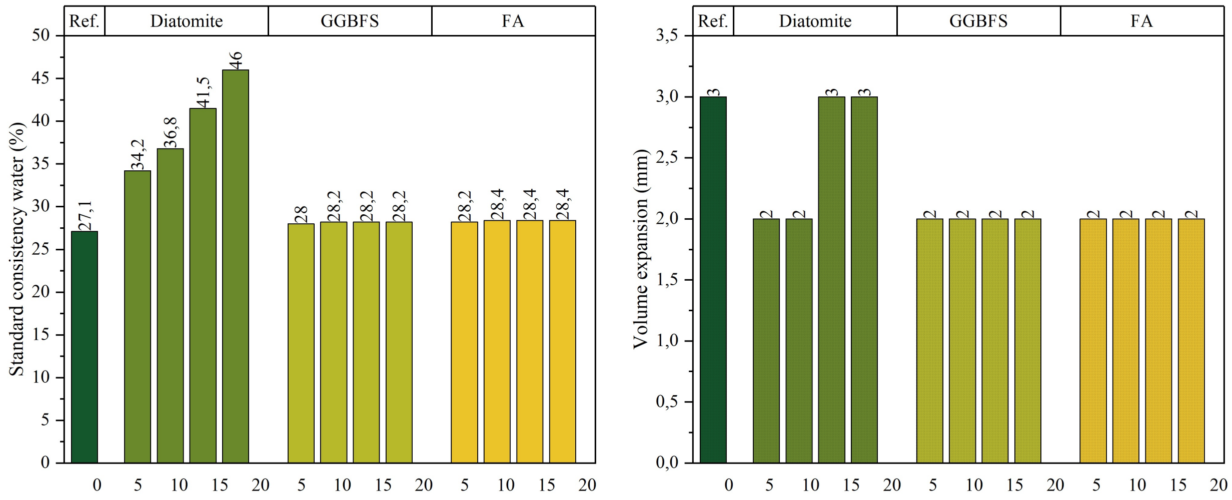

(A) . Standard consistency water.
(B) . Volume expansion.

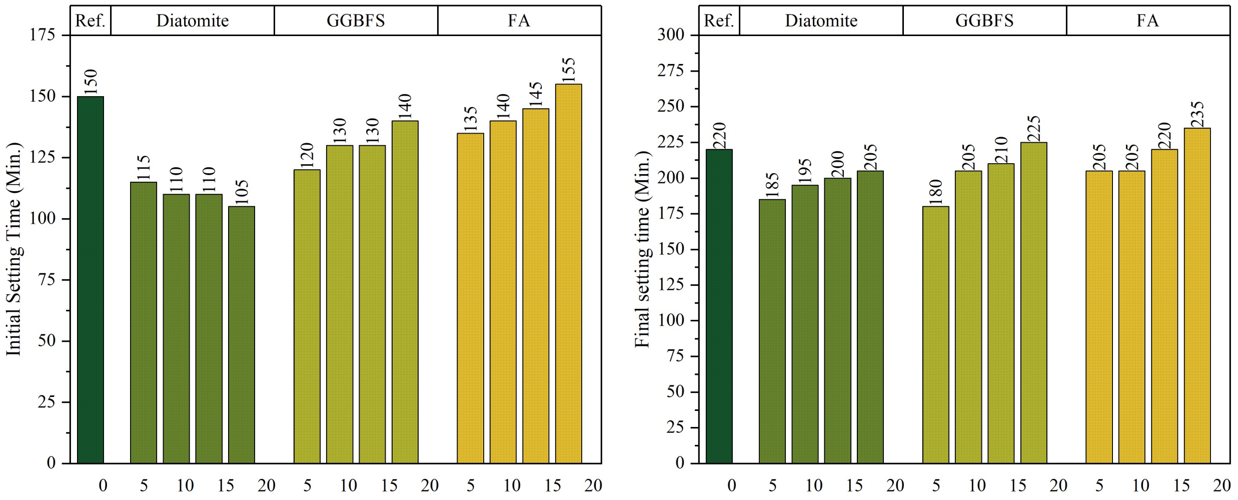

(C) . Initial setting time.
(D) . Final setting time.

Figure 6. Physical properties of cement.

higher consistency water content because of greater internal friction. In the study conducted by Hasan and Saidi, the amount of standard consistency water increased as the diatomite content increased [71]. Water requirement for blended cement is also higher than for standard Portland cement, according to Kastis et al. [72]. Das et al. stated that FA has a spherical structure, whereas GGBFS has an angular structure. They also stated that SCMs with angular structures directly reduce workability. They found that rice husk ash reduced workability due to its high porosity [73]. Diatomite had the same properties as rice husk ash in this study. Volumetric expansion values of cement are given in Figure 6b. The volumetric expansion of cement varies between 2–3 mm. It was observed that the volumetric expansion values were very close to each other. According to EN 196-3 standard [65], the volumetric expansion of cement should be below 10 mm. It was determined that the cement produced from different SCMs complied with this standard.

As seen in Figure 6c, the reference mixture's initial setting time was 150 minutes. Diatomite-containing cement's initial setting time varies between 105–115 minutes. In addition, as the diatomite content increases, the setting time becomes shorter. In particular, the initial setting time of the cement with 20 % diatomite content decreased by approximately 1.4 times as compared to the reference mixture. The diatomite's high SiO_2 content (87.3 %) and specific surface area reduced the setting time. While the setting time of a cement mixture containing GGBFS varies between 120–140 minutes, the initial setting time for mixtures with FA varies between 135–155 minutes. As the FA and GGBFS content increases, the initial setting time increases. Due to the higher hydraulic properties of GGBFS, the initial setting time is relatively shorter than that of the FA cement. In Figure 6d, it was observed that as the replacement ratio increased in the diatomite-containing cement, the final setting time increased. A similar situation was observed for the cement using FA and GGBFS.

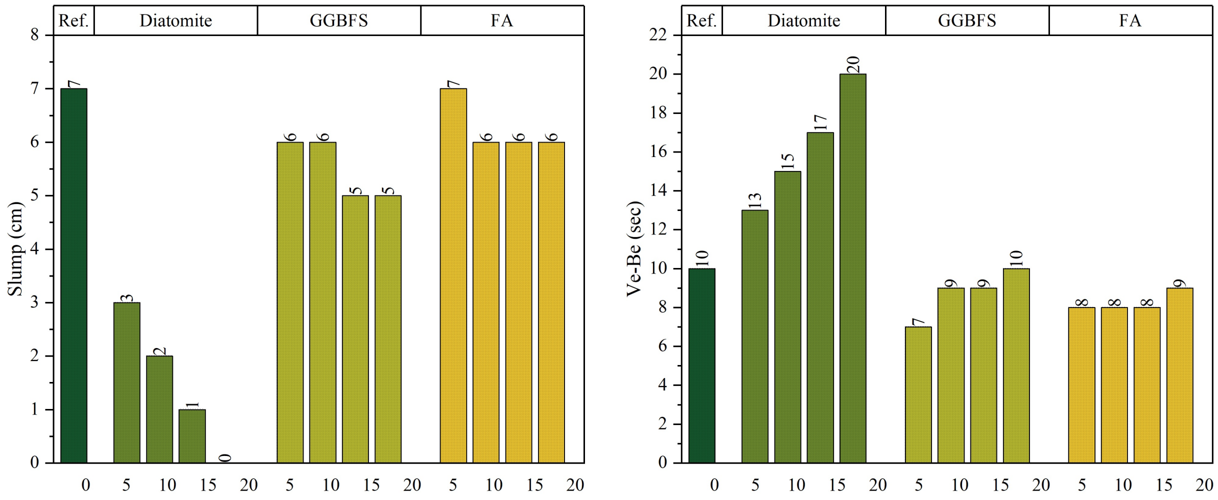

(A) . Slump. (B) . Ve-Be time.

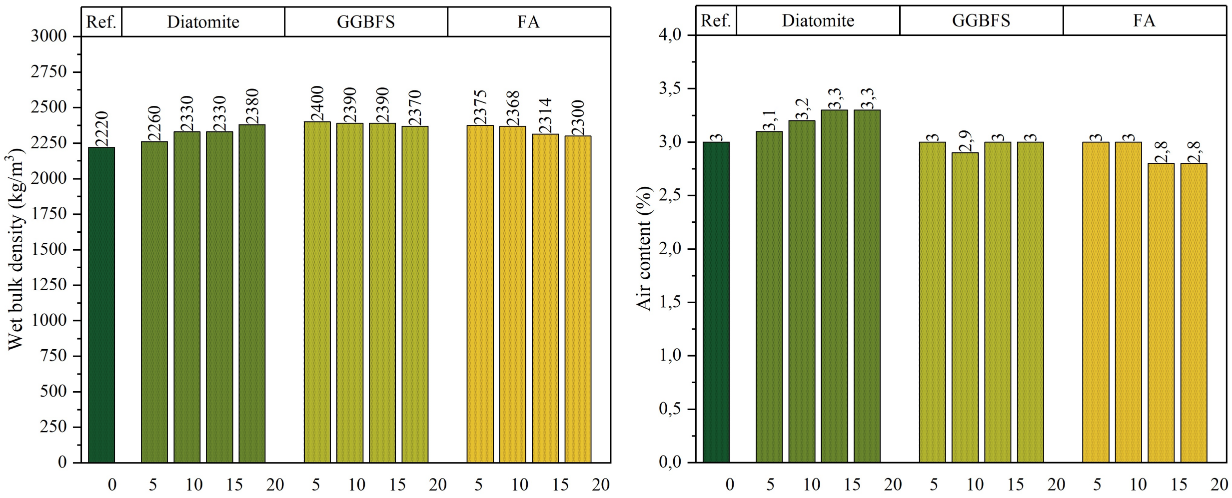

(C) . Wet bulk density. (D) . Final setting time.

Figure 7. Fresh properties of concrete.

However, when different SCMs are used at 5, 10, and 15 % ratios, the final setting time is shorter than that of the reference mixture. As the replacement ratio increases, the setting times are longer because the clinker in the cement decreases.

C_3S is responsible for the early setting of cement paste because it hardens quickly in the presence of water [74]. When C_3A is hydrated, it produces a considerable amount of heat, raising the prevailing setting temperature, causing OPC to set faster than blended cement. As the temperature increases, the setting time of the cement is shortened [75, 76]. The fact that blended cement contains pozzolanic additives, which increase their water demand/standard consistency, could also account for their extended setting time. Cement pastes with high standard consistency water are observed to have a slower setting time. The cohesiveness/rheology of the pastes is reduced by high standard consistency water, which extends the setting time [77, 78].

3.2. Fresh properties of concrete

The slump values of the concrete decrease as the replacement ratio increases, as shown in Figure 7a. The slump value decreased between 14 and 28 % when GGBFS was used. When FA was used, the slump value decreased by approximately 14 %. The spherical particle structure of FA did not reduce the slump value much. However, the angular particle structure of the GGBFS noticeably reduced the slump value. Although the specific surface area of the GGBFS was low, the particle shape had a greater effect on the slump value. The most significant slump value decrease was observed in the diatomite cement concrete. The slump values of concrete made with diatomite cement decreased between 57 and 100 %. The high specific surface area and porosity of diatomite led to a decrease in slump values. It is seen that the Ve-Be times of the concretes produced from these cements vary between 13–20 seconds (Figure 7b). In particular, the Ve-Be time of concretes made with 20 % diatomite cement has increased by two times. The Ve-Be times

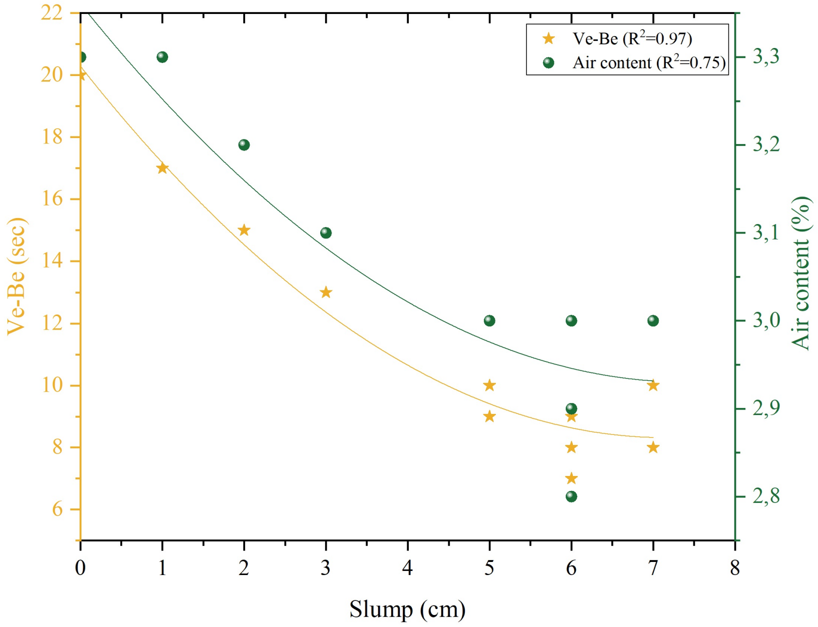

Figure 8. Correlation of fresh concrete properties.

of GGBFS and FA mixtures are close to the reference mixture. The Ve-Be time of the concretes produced with 5 % GGBFS cement was shortened by 30 %. The specific surface area of the GGBFS, 2400 cm^2/g, was very effective. However, as the replacement ratio in the GGBFS increased, the Ve-Be time also increased. The Ve-Be time of the FA mixtures was shortened by 10–20 %. Because of the angularity and irregular forms of the cementitious materials, friction between small particles increased, making the fresh mixture coarse. This effect may increase the water requirement as compared to the reference mix. [79]. In this study, the workability of GGBFS decreased due to its particle structure.

As seen in Figure 7c, the wet bulk densities of the concrete vary between 2220–2400 $\mathrm{kg/m}^3$. However, the wet bulk density of all concretes with SCM is higher than that of the reference concrete. As the replacement ratio increased in GGBFS and FA mixtures, the wet bulk density of the concretes decreased. However, in the case of diatomite concrete, the wet bulk density values increase as the replacement ratio increases. The amount of aggregate in concrete mixtures was kept constant. When diatomite is used instead of cement, the paste volume increases. When 20 % diatomite is used in mixes, the paste volume rises by approximately 10 %. The increase in paste volume increases the wet bulk density of the mixtures. The wet bulk density of the concretes produced with 20 % diatomite cement increased by 7 %. Similar results are also seen for the air content of concretes (Figure 7d). The air contents of the GGBFS and FA mixtures are very close to the reference mixture. Since FA has a higher specific surface area than cement, it fills the voids between cement particles. However, the air content increased by up to 10 % in diatomite mixtures. Because diatomite affects the workability of concrete, pouring it in the mould becomes problematic. As a result, the air content of the mixtures increased.

Nawaz et al. stated that the density increases as the replacement ratio increases in the case FA concrete. The rise in workability of FA explained the reason for this increase. FA micro-spherical particles may act as lubricants to enhance concrete density while maintaining the same compaction energy [80]. In the study conducted by Pokorny et al., the bulk density increased when diatomite was used up to 10 % [81]. Since diatomite has a smaller particle size than cement, it effectively filled the gaps between the cement and the aggregate. As a result of this effect, it increased the wet bulk density of concretes.

Figure 8 shows the relationship between slump values and other fresh concrete properties. It is seen that the R2 value between the Slump and Ve-Be time is 0.97. As the slump value of the mixtures increases, Ve-Be times decrease. The R2 value between the slump value and the air content was 0.75. As the slump value of the mixtures increases, the air content decreases. The decrease in the slump value increases the amount of energy required for vibration. Since the constant vibration energy was used in this study, the air content of the concretes increased as the slump value decreased.

3.3. Mechanical properties

As seen in Figure 9a, the increase in curing time increases the compressive strength of the concrete. The 28-day compressive strength of the concrete varies between 29.2 and 29.8 MPa, while 180-day compressive strengths vary between 32.1 and 39.5 MPa. Using SCM in concrete mixtures did not affect the 28-day compressive strength much. When the compressive

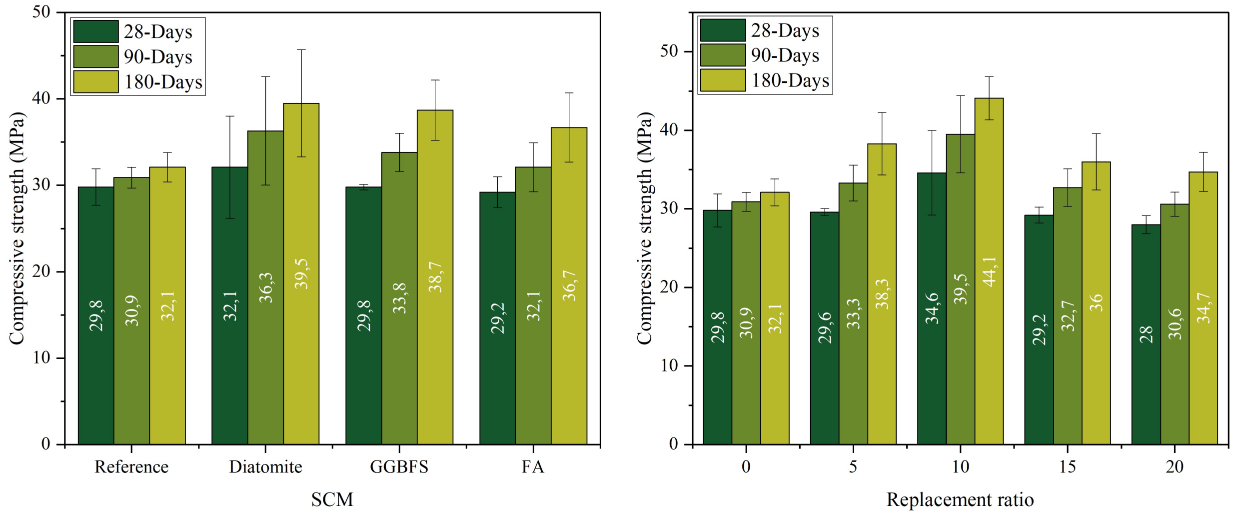

(a) . Effect of SCM.

(b) . Effect of replacement ratio.

Figure 9. Compressive strengths of concrete mixes.

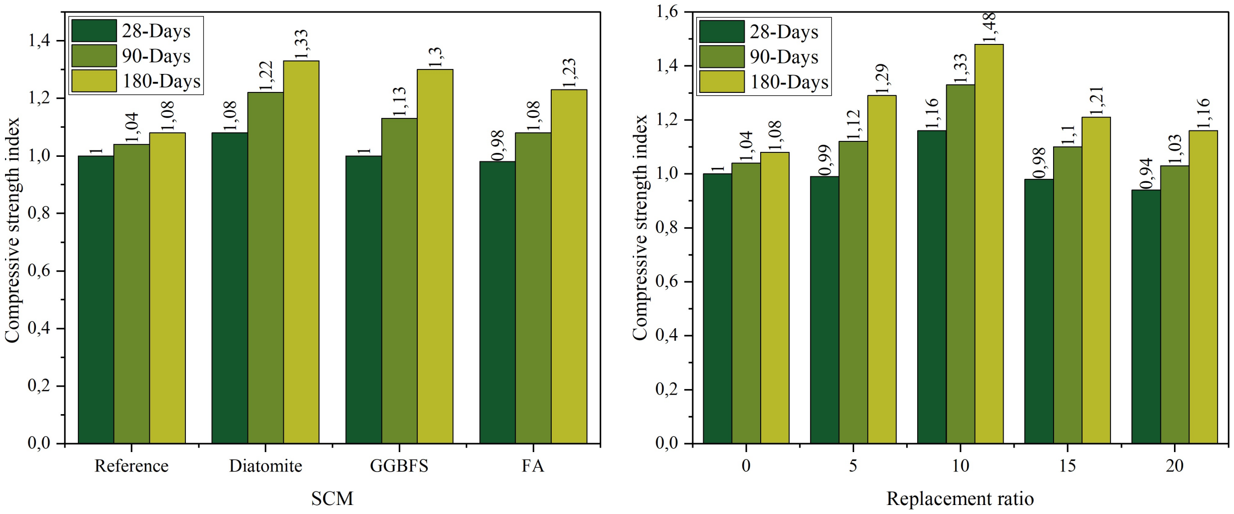

(a) . Effect of SCM.

(b) . Effect of replacement ratio.

Figure 10. Compressive strength index of concrete mixes.

strengths of 90 and 180 days were examined, it was observed that the use of diatomite increased the compressive strength more significantly. The high SiO_2 content and specific surface area of diatomite increased the compressive strength. It was observed that concretes produced with GGBFS had a relatively higher compressive strength than concretes with FA. The hydraulic properties of GGBFS ensured its compressive strength to be higher than that of the reference mixture. Figure 9b shows that the use of SCM up to 10 % increases the compressive strengths. However, when the 180-day compressive strengths are examined, the compressive strengths of the mixtures using 15 and 20 % SCM are higher than that of the reference mixture. When a high proportion of SCM is used, the curing time should also be increased. Especially the use of 10 % SCM improved the compressive strengths considerably. In addition to the pozzolanic activity, the micro filler effect of SCMs also helped to increase the compressive strength. If 20 % SCM is used, the 28-day compressive strength is reduced by 6.7 %.

The compressive strength indexes in Figure 8 were determined according to the 28-day compressive strength of the reference mixture. The 180-day compressive strength of the reference mixture increased by 8 % as compared to the 28th day (Figure 10a). The 28-day compressive strength of the FA mixture decreased by 2 %. Concrete mixes containing diatomite had the greatest values in terms of 90 and 180-day compressive strengths. While the 180-day compressive strength of GGBFS increased by 30 %, this ratio was 23 % for FA mixtures. When the 28-day compressive strengths were examined, the compressive strength increased only at a 10 % replacement ratio (Figure 10b). If 20 % SCM is used, the compressive strength is reduced by approximately 6 %. For the 90- and 180-day curing times, higher compressive strengths were observed for the 10 % replacement ratio. In particular, the com-

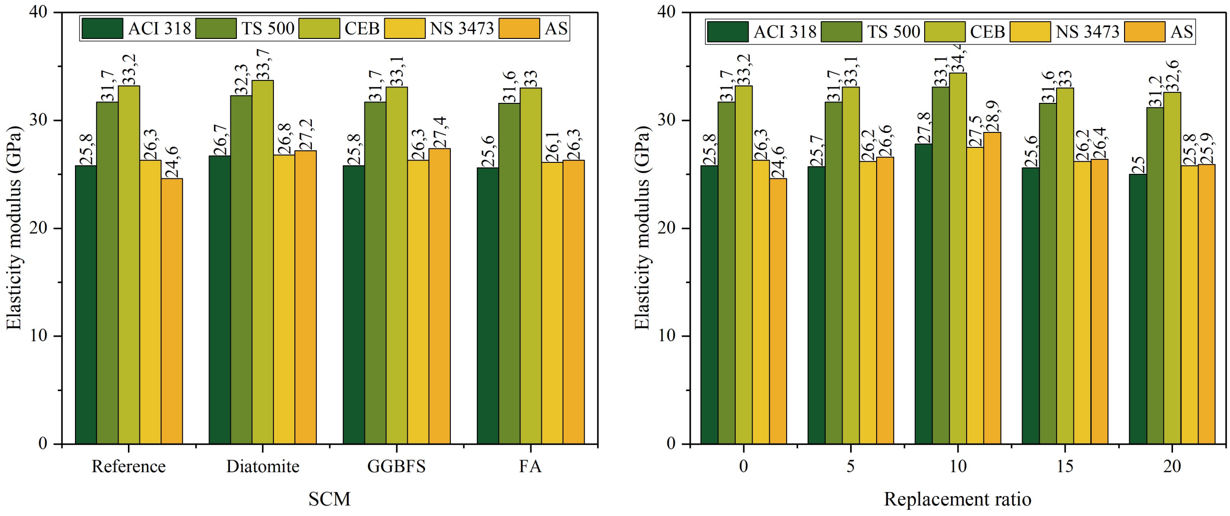

(a) . Effect of SCM.

(b) . Effect of replacement ratio.

Figure 11. The elasticity modulus of concrete mixes.

pressive strength increased approximately 1.5 times for the 10 % replacement on the 180th day.

Shaikh and Hosan increased the compressive strength of the pastes by using 60 % GGBFS [82]. El-Chabib and Syed [14] observed similar results. Due to the hydraulic activity and slag activity index of GGBFS, the addition of GGBFS increases the compressive strength of concrete [83]. The increase in compressive strength of FA and diatomite is related to the pozzolanic activity. The delayed pozzolanic reaction of the SCM causes a reduction in the size of the crystalline compounds in the paste matrix, particularly calcium hydroxide, resulting in an increase in compressive strength development with age in mixtures prepared with high contents of SCM [84]. Ahmadi et al. explained the increase in compressive strength in diatomite-containing mixtures with rich SiO2 content. They stated that diatomite is an active pozzolan and can be replaced by up to 40 % with cement [85].

3.4. Theoretical elasticity modulus

Some empirical formulas estimated the elasticity modules of the mixtures in the literature. In these formulas, the mixtures' 28-day compressive strength and bulk density are used. The equations (1)–(5) used are presented below. ACI 318-95 (ACI Committee 318 1995):

$$E_c = 4.73(f_c)^{1/2}. \tag{1}$$

TS 500 (Turkish Standardization Institute 2000):

$$E_c = 3.25(f_c)^{1/2} + 14. \tag{2}$$

CEB (Comité Euro-International du Béton-Fédération Internationale de la Précontrainte (CEB-FIP) Model Code 1993):

$$E_c = 10(f_c + 8)^{1/3}. \tag{3}$$

NS 3473 (Norwegian Council for Building Standardization 1992):

$$E_c = 9.5(f_c)^{0.3}. \tag{4}$$

AS (Standards Australia Concrete structures 2009):

$$Ec = 0.043w^{1.5}(f_c)^{1/2}, \tag{5}$$

where; f_c [MPa] and E_c [GPa] are 28-day compressive strength and modulus of elasticity of the concrete, respectively, and w [kg/m^3] is the bulk density of concrete.

As shown in Figure 11a and Figure 11b, the elasticity modules of the mixtures using SCM are quite close to the reference mixture. It has been determined that the modules in elasticity determined according to TS 500 and CEB are similar. The modulus of elasticity of the mixes using diatomite is relatively higher. In addition, using SCM up to 10 % noticeably increases the elasticity modulus. While the modulus of elasticity of concrete varies between 32.6–34.4 GPa according to TS 500, it varies between 25–27.8 GPa according to ACI 318. The E-modulus is determined by the components and qualities of the concrete. In particular, the E-modulus, aggregate shape, and cement paste structure significantly impact the findings. However, since no fibre was used in this study, no significant difference was observed between the moduli of elasticity of different mixtures. Letelier et al. produced concrete with compressive strengths ranging from 22.8–31.4 MPa using up to 15 % diatomite. The elasticity modulus of the concrete varies between 16.7–24.2 GPa [86]. Gencel et al.'s study showed that as the FA content increased, the modulus of elasticity decreased [87].

3.5. Abrasion resistance

The abrasion depths of concretes determined according to ASTM C944 are given in Figure 12. As the

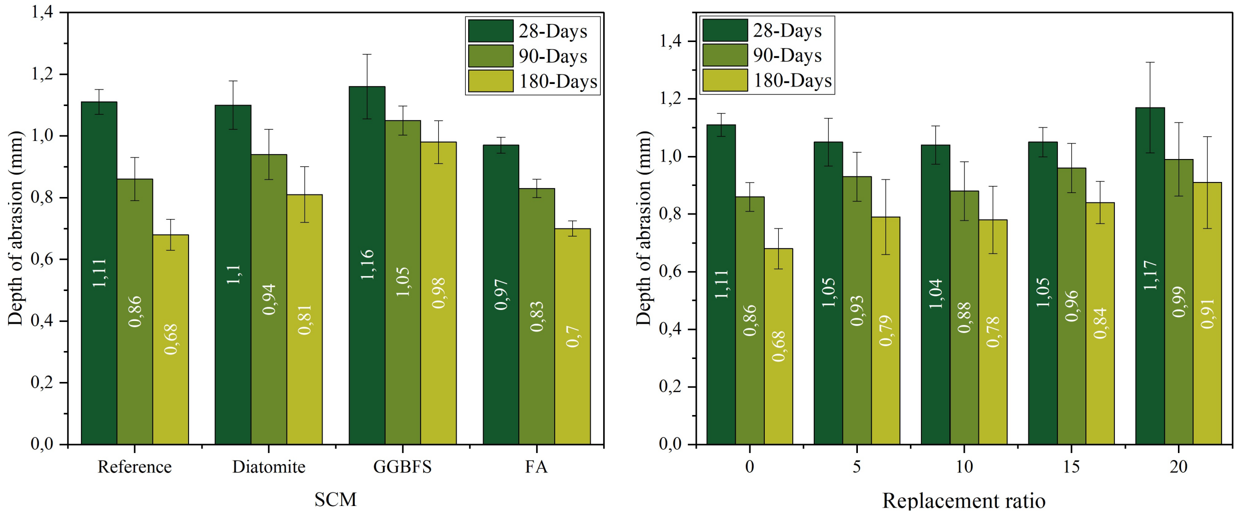

(A) . Effect of SCM.

(B) . Effect of replacement ratio.

FIGURE 12. Abrasion depth of concrete mixes.

curing time applied to the concretes increased, the abrasion depth decreased (Figure 12a). It has been observed that the curing time has a significant impact the abrasion effect. In particular, the pozzolanic activity was effective in concretes with SCM. However, the abrasion depths of concrete with SCM are relatively larger than that of the reference concrete. Using FA in SCM concretes reduced the abrasion depth more than using GGBFS and diatomite. While the abrasion depth of the GGBFS on the 180th day was approximately 1 mm, the abrasion depth of the FA was 0.70 mm. As seen in Figure 12b, the use of SCM by up to 15 % in 28-day mixtures reduced the depth of abrasion. However, this effect was not observed for the abrasion depth of the 90- and 180-day mixtures. Especially on the 180th day, the abrasion depth of the mixtures with 20 % SCM increased by 34 % as compared to the reference mixture. Abrasion depths of concrete mixtures decreased below 1 mm from the 90th day onwards. It is more appropriate to use FA in concretes exposed to abrasion. The replacement ratio should be 10 %, as in the compressive strength. Since diatomite has a porous structure, it did not contribute to the abrasion resistance. In addition, the low specific gravity of GGBFS as compared to cement adversely affected its abrasion resistance.

Sujjavanich et al. determined the abrasion resistance of the concretes they prepared using FA and metakaolin. It was observed that concretes containing 20 % FA lost less weight due to abrasion. This effect was explained by the improvement of the microstructure of pozzolans [88]. The abrasion resistance of concrete is typically affected by the strength of mortar and the mortar-aggregate bond for the same coarse aggregate types and volume. As a result of improving the mortar strength and bonding with aggregate particles, SCMs with strong pozzolanic reactivity, such as silica fume and metakaolin, are expected to improve the surface abrasion resistance of surface abrasion concrete [89]. The chemical characteristics of FA were largely responsible for the abrasion resistance of concrete using FA [90]. Amini et al. improved the abrasion resistance of concretes by using up to 40 % of GGBFS [91]. In the literature, not many studies show diatomite's effect on abrasion. However, due to SCM's high porosity, the abrasion's depth increased.

3.6. STATISTICAL ANALYSIS AND OPTIMIZATION

In Table 3, statistical analyses of the experimental data are given. The relevance of independent factors on dependent variables is displayed by the p-value. If the p-value is less than 0.05, the independent variables will be considered important. When the p values were examined, it was observed that the change in the SCM type generally affected many properties of the concretes. A higher F value shows that the performance characteristics are significantly affected by the variability in the process parameter. As with the p-value, it is seen that the change in the SCM type causes a larger change in the F value. The change of the SCM type affects mostly the fresh state properties of the cement and concrete. In particular, standard consistency water and initial setting time are highly affected by the SCM type. In addition, the SCM type also affects the depth of abrasion. If FA is used instead of diatomite in 28-day mixtures, the depth of abrasion decreases by 12 %. The change in the replacement ratio of SCMs affects concretes' fresh and hardened properties. The SCM type has no significant effect on 28-day compressive strength. This is an indication that SCMs have similar characteristics to each other.

The optimization was performed according to the test parameters given in Table 4. The concrete mix using 5 % FA has the best properties as compared to the reference mix. Although 5 % FA increased the standard consistency water by 4.1 %, it decreased the 28-day abrasion depth by 15.5 %. However, if CO_2 emissions are considered, 10 % FA can be used.

Test Parameters	**SCM**				**Replacement Ratio [%]**			
	p	F-Value	Effect [%]	Significance	p	F-Value	Effect [%]	Significance
S. Cons. Water	0.001	19.03	99.0	Yes	0.899	0.19	1.0	No
Initial Setting Time	0.000	22.12	98.8	Yes	0.921	0.16	1.2	No
Slump	0.042	4.61	83.1	Yes	0.465	0.94	16.9	No
28 Days-Comp Str	0.553	0.63	22.5	No	0.171	2.17	77.5	No
28 Days-Depth of abrasion	0.035	4.98	86.5	Yes	0.536	0.78	13.5	No

Table 3. Statistical analysis results.

Test parameters	**Target function**	**Optimum Mix (FA5)***	**Reference**	**Difference**
S. Consistency Water	Minimum	28.2	27.1	-4.1
Initial setting time	Minimum	135	150	10
Slump	Maximum	7	7	0
28 Days-Comp Str	Maximum	30.2	29.8	1.3
28 Days-Depth of abrasion	Minimum	0.93	1.1	15.5

* Optimum mix design: %5 FA

Table 4. Optimum mixing ratios.

4. Conclusions

- Diatomite increased the standard consistency of water as compared to other SCMs. The standard consistency water amount of GGBFS and FA showed similar properties to the reference mixture.
- Due to diatomite's highly active SiO_2 content being shortened, the replacement ratio's initial setting time increased. However, as the diatomite replacement ratio increased, the final setting times were prolonged. As the GGBFS and FA replacement ratio increases, the setting times become longer. However, pastes' setting times (initial and final) with SCM are generally shorter than that of the reference mixture.
- While the high specific surface area and porosity of diatomite decreased the slump values, it led to the prolongation of Ve-Be times. Despite the low specific surface area of the GGBFS, the rough particle shape reduced the slump values. The FA mixtures showed similar properties to the reference mixture in the slump and Ve-Be tests.
- There was no significant difference between wet bulk densities in fresh concrete. The wet bulk densities of the concrete vary between 2220–2400 kg/m^3. While the wet bulk densities increased as the diatomite replacement ratio increased, the opposite could be observed for the FA mixtures. Such an effect was observed because the diatomite increased the paste volume more than other SCMs. In addition, as the diatomite replacement ratio increased, the air content increased relatively.
- The high specific surface area and active SiO_2 content of diatomite were more effective in increasing the compressive strength. As the curing time increased, the strength development of the mixtures with SCM was greater than that of the reference mixture. In addition, it was determined that the optimum replacement ratio was 10 % in the mixtures with SCM. All concrete mixes' theoretical modulus of elasticity is more than 20 GPa.
- As the curing time increased, the abrasion depths decreased due to the development of both the hydration and the pozzolanic activity. The abrasion depth of FA mixtures was smaller. It was observed that the abrasion depth was larger for the GGBFS. In addition, the abrasion depths increased at a 20 % substitution rate for the mixtures with SCM.
- Statistically, the change in the SCM type affects the engineering performance of concrete more significantly than the change in the substitution ratio, which did not have as pronounced effect on the engineering properties. It was determined that the 5 % FA mixtures had the closest properties to the reference mixture. However, considering environmental factors and CO2 emissions, it is thought that the optimal replacement ratio might be 10 %.

- As a result, it has been determined that Eco-Friendly concrete can be produced by using SCMs with different properties of up to 20 %.

Acknowledgements

This study was supported by Gazi University Scientific Investigation Projects (BAP) unit with the code 07/2005-28.

References

[1] G. Bramley, S. Power. Urban form and social sustainability: The role of density and housing type. *Environment and Planning B: Planning and Design* **36**(1):30–48, 2009. `https://doi.org/10.1068/b33129`.

[2] S. Samad, A. Shah. Role of binary cement including Supplementary Cementitious Material (SCM), in production of environmentally sustainable concrete: A critical review. *International Journal of Sustainable Built Environment* **6**(2):663–674, 2017. `https://doi.org/10.1016/j.ijsbe.2017.07.003`.

[3] The Concrete Centre. Specifying Sustainable Concrete'. Accessed 2021-08-16, `https://www.concretecentre.com/publications`.

[4] A. A. Aliabdo, A. E. M. Abd Elmoaty, A. Y. Aboshama. Utilization of waste glass powder in the production of cement and concrete. *Construction and Building Materials* **124**:866–877, 2016. `https://doi.org/10.1016/j.conbuildmat.2016.08.016`.

[5] Statista. Major countries in worldwide cement production 2015-2019, 2020. Accessed 2020-12-30, `https://www.statista.com/statistics/267364/world-cement-production-by-country/`.

[6] J. Vargas, A. Halog. Effective carbon emission reductions from using upgraded fly ash in the cement industry. *Journal of Cleaner Production* **103**:948–959, 2015. `https://doi.org/10.1016/j.jclepro.2015.04.136`.

[7] E. T. Bueno, J. M. Paris, K. A. Clavier, et al. A review of ground waste glass as a supplementary cementitious material: A focus on alkali-silica reaction. *Journal of Cleaner Production* **257**:120180, 2020. `https://doi.org/10.1016/j.jclepro.2020.120180`.

[8] J. M. Paris, J. G. Roessler, C. C. Ferraro, et al. A review of waste products utilized as supplements to Portland cement in concrete. *Journal of Cleaner Production* **121**:1–18, 2016. `https://doi.org/10.1016/j.jclepro.2016.02.013`.

[9] J. L. B. Galvão, H. D. Andrade, G. J. Brigolini, et al. Reuse of iron ore tailings from tailings dams as pigment for sustainable paints. *Journal of Cleaner Production* **200**:412–422, 2018. `https://doi.org/10.1016/j.jclepro.2018.07.313`.

[10] Deepti, A. Sinha, P. Biswas, et al. Utilization of LD slag from steel industry for the preparation of MF membrane. *Journal of Environmental Management* **259**:110060, 2020. `https://doi.org/10.1016/j.jenvman.2019.110060`.

[11] Y. Jiang, T. C. Ling, C. Shi, S. Y. Pan. Characteristics of steel slags and their use in cement and concrete–A review. *Resources, Conservation and Recycling* **136**:187–197, 2018. `https://doi.org/10.1016/j.resconrec.2018.04.023`.

[12] J. Y. Lee, J. S. Choi, T. F. Yuan, et al. Comparing properties of concrete containing electric arc furnace slag and granulated blast furnace slag. *Materials* **12**(9):1371, 2019. `https://doi.org/10.3390/ma12091371`.

[13] P. R. de Matos, J. C. Oliveira, T. M. Medina, et al. Use of air-cooled blast furnace slag as supplementary cementitious material for self-compacting concrete production. *Construction and Building Materials* **262**:120102, 2020. `https://doi.org/10.1016/j.conbuildmat.2020.120102`.

[14] H. Zhao, W. Sun, X. Wu, B. Gao. The properties of the self-compacting concrete with fly ash and ground granulated blast furnace slag mineral admixtures. *Journal of Cleaner Production* **95**:66–74, 2015. `https://doi.org/10.1016/j.jclepro.2015.02.050`.

[15] A. Gholampour, T. Ozbakkaloglu. Performance of sustainable concretes containing very high volume Class-F fly ash and ground granulated blast furnace slag. *Journal of Cleaner Production* **162**:1407–1417, 2017. `https://doi.org/10.1016/j.jclepro.2017.06.087`.

[16] Y. J. Patel, N. Shah. Enhancement of the properties of Ground Granulated Blast Furnace Slag based Self Compacting Geopolymer Concrete by incorporating Rice Husk Ash. *Construction and Building Materials* **171**:654–662, 2018. `https://doi.org/10.1016/j.conbuildmat.2018.03.166`.

[17] P. Monteiro, P. Mehta. *Concrete: Microstructure, properties, and materials.* Mc Graw Hill, 3rd edn., 2006. ISBN 0071462899.

[18] G. Li, A. Zhang, Z. Song, et al. Ground granulated blast furnace slag effect on the durability of ternary cementitious system exposed to combined attack of chloride and sulfate. *Construction and Building Materials* **158**:640–648, 2018. `https://doi.org/10.1016/j.conbuildmat.2017.10.062`.

[19] W. Song, J. Yin. Hybrid effect evaluation of steel fiber and carbon fiber on the performance of the fiber reinforced concrete. *Materials* **9**(8):704, 2016. `https://doi.org/10.3390/ma9080704`.

[20] P. S. Deb, P. Nath, P. K. Sarker. The effects of ground granulated blast-furnace slag blending with fly ash and activator content on the workability and strength properties of geopolymer concrete cured at ambient temperature. *Materials and Design* **62**:32–39, 2014. `https://doi.org/10.1016/j.matdes.2014.05.001`.

[21] S. Dadsetan, J. Bai. Mechanical and microstructural properties of self-compacting concrete blended with metakaolin, ground granulated blast-furnace slag and fly ash. *Construction and Building Materials* **146**:658–667, 2017. `https://doi.org/10.1016/j.conbuildmat.2017.04.158`.

[22] L. Faguang, F. Naiqian, L. Xinying. An experimental study on the properties of resistance to diffusion of chloride ions of fly ash and blast furnace slag concrete. *Cement and Concrete Research* **30**:989–992, 2000. `https://doi.org/10.1016/S0008-8846(00)00250-7`.

[23] Y. K. Cho, S. H. Jung, Y. C. Choi. Effects of chemical composition of fly ash on compressive strength of fly ash cement mortar. *Construction and Building Materials* **204**:255–264, 2019. `https://doi.org/10.1016/j.conbuildmat.2019.01.208`.

[24] M. Ahmaruzzaman. A review on the utilization of fly ash. *Progress in Energy and Combustion Science* **36**(3):327–363, 2010. `https://doi.org/10.1016/j.pecs.2009.11.003`.

[25] A. Bicer. Effect of fly ash particle size on thermal and mechanical properties of fly ash-cement composites. *Thermal Science and Engineering Progress* **8**:78–82, 2018. `https://doi.org/10.1016/j.tsep.2018.07.014`.

[26] H. Xiao, W. Wang, S. H. Goh. Effectiveness study for fly ash cement improved marine clay. *Construction and Building Materials* **157**:1053–1064, 2017. `https://doi.org/10.1016/j.conbuildmat.2017.09.070`.

[27] Z. Liu, D. Xu, Y. Zhang. Experimental investigation and quantitative calculation of the degree of hydration and products in fly ash-cement mixtures. *Advances in Materials Science and Engineering* **2017**:2437270, 2017. `https://doi.org/10.1155/2017/2437270`.

[28] W. She, Y. Du, G. Zhao, et al. Influence of coarse fly ash on the performance of foam concrete and its application in high-speed railway roadbeds. *Construction and Building Materials* **170**:153–166, 2018. `https://doi.org/10.1016/j.conbuildmat.2018.02.207`.

[29] A. Wang, C. Zhang, W. Sun. Fly ash effects: I. The morphological effect of fly ash. *Cement and Concrete Research* **33**(12):2023–2029, 2003. `https://doi.org/10.1016/S0008-8846(03)00217-5`.

[30] M. Liu, H. Tan, X. He. Effects of nano-SiO_2 on early strength and microstructure of steam-cured high volume fly ash cement system. *Construction and Building Materials* **194**:350–359, 2019. `https://doi.org/10.1016/j.conbuildmat.2018.10.214`.

[31] The British Standards Institution. Cement Part 1: Composition, specifications and conformity criteria for common cements (BS Standard No. BS EN 197-1), 2011.

[32] M. R. Dunstan, M. D. A. Thomas, J. B. Cripwell, D. J. Harrison. Investigation into the long-term in-situ performance of high fly ash content concrete used for structural applications. In *American Concrete Institute, ACI Special Publication*, vol. 132, pp. 1–20. 1992. `https://doi.org/10.14359/1905`.

[33] F. Aguayo, A. Torres, Y.-J. Kim, O. Thombare. Accelerated carbonation assessment of high-volume fly ash concrete. *Journal of Materials Science and Chemical Engineering* **08**(03):23–38, 2020. `https://doi.org/10.4236/msce.2020.83002`.

[34] D. S. Hopkins, M. D. A. Thomas, D. B. Oates, et al. York university uses high-volume fly ash concrete for green building. *Proceedings–Canadian Society for Civil Engineering* pp. 1–7, 2001.

[35] F. U. Shaikh, S. W. Supit. Compressive strength and durability properties of high volume fly ash (HVFA) concretes containing ultrafine fly ash (UFFA). *Construction and Building Materials* **82**:192–205, 2015. `https://doi.org/10.1016/j.conbuildmat.2015.02.068`.

[36] F. U. Shaikh, S. W. Supit. Mechanical and durability properties of high volume fly ash (HVFA) concrete containing calcium carbonate ($CaCO_3$) nanoparticles. *Construction and Building Materials* **70**:309–321, 2014. `https://doi.org/10.1016/j.conbuildmat.2014.07.099`.

[37] R. N. Swamy, H. H. Hung. Engineering properties of high volume fly ash concrete. In *American Concrete Institute, ACI Special Publication*, vol. 178, pp. 331–359. 1998. `https://doi.org/10.14359/5987`.

[38] M. Tyler Ley, N. J. Harris, K. J. Folliard, K. C. Hover. Investigation of air-entraining admixture dosage in fly ash concrete. *ACI Materials Journal* **105**(5):494–498, 2008. `https://doi.org/10.14359/19979`.

[39] N. Bouzoubaa, M. H. Zhang, V. M. Malhotra, D. M. Golden. Mechanical properties and durability of laboratory produced high-volume fly ash blended cements. In *American Concrete Institute, ACI Special Publication*, vol. 199, pp. 55–82. 2001. `https://doi.org/10.14359/10484`.

[40] D. Burden. The durability of concrete containing high levels of fly ash, 2006. PCA R&D Serial No. 2989. Accessed 2021-01-05, `https://www.cement.org/bookstore/profile.asp?itemid=SN2989&itemid=SN2989`.

[41] S. Uthaman, R. P. George, V. Vishwakarma, et al. Enhanced seawater corrosion resistance of reinforcement in nanophase modified fly ash concrete. *Construction and Building Materials* **221**:232–243, 2019. `https://doi.org/10.1016/j.conbuildmat.2019.06.070`.

[42] M. Kurtay, H. Gerengi, Y. Kocak, et al. The potency of zeolite and diatomite on the corrosive destruction of reinforcing steel in 1M HNO_3 environment. *Construction and Building Materials* **236**:117572, 2020. `https://doi.org/10.1016/j.conbuildmat.2019.117572`.

[43] S. Xu, J. Wang, Q. Jiang, S. Zhang. Study of natural hydraulic lime-based mortars prepared with masonry waste powder as aggregate and diatomite/fly ash as mineral admixtures. *Journal of Cleaner Production* **119**:118–127, 2016. `https://doi.org/10.1016/j.jclepro.2016.01.069`.

[44] N. Sharma, P. Sharma, S. kr Verma. Influence of Diatomite on the properties of mortar and concrete: A Review. *IOP Conference Series: Materials Science and Engineering* **1116**(1):012174, 2021. `https://doi.org/10.1088/1757-899x/1116/1/012174`.

[45] D. Taoukil, Y. El meski, M. lhassane Lahlaouti, et al. Effect of the use of diatomite as partial replacement of sand on thermal and mechanical properties of mortars. *Journal of Building Engineering* **42**:103038, 2021. `https://doi.org/10.1016/j.jobe.2021.103038`.

[46] B. Yilmaz, N. Ediz. The use of raw and calcined diatomite in cement production. *Cement and Concrete Composites* **30**(3):202–211, 2008. `https://doi.org/10.1016/j.cemconcomp.2007.08.003`.

[47] V. J. Inglezakis, A. A. Zorpas. Natural zeolites structure and porosity. In *Handbook of Natural Zeolites*, pp. 133–146. Bentham Science Publisher, 2012. `https://doi.org/10.2174/978160805261511201010133`.

[48] N. Degirmenci, A. Yilmaz. Use of diatomite as partial replacement for Portland cement in cement mortars. *Construction and Building Materials* **23**(1):284–288, 2009. `https://doi.org/10.1016/j.conbuildmat.2007.12.008`.

[49] J. Li, W. Zhang, C. Li, P. J. Monteiro. Green concrete containing diatomaceous earth and limestone: Workability, mechanical properties, and life-cycle assessment. *Journal of Cleaner Production* **223**:662–679, 2019. `https://doi.org/10.1016/j.jclepro.2019.03.077`.

[50] L. G. Xiao, X. X. Liu. Effect of diatomite on thermal insulation properties of straw fiber cement-based composites. *IOP Conference Series: Earth and Environmental Science* **295**(3):032047, 2019. `https://doi.org/10.1088/1755-1315/295/3/032047`.

[51] M. Sarıdemir, S. Çelikten, A. Yıldırım. Mechanical and microstructural properties of calcined diatomite powder modified high strength mortars at ambient and high temperatures. *Advanced Powder Technology* **31**(7):3004–3017, 2020. `https://doi.org/10.1016/j.apt.2020.05.024`.

[52] W. Du. Study on preparation of ultra-high strength and high performance concrete from diatomite and its mechanical properties. *IOP Conference Series: Earth and Environmental Science* **376**(1):012054, 2019. `https://doi.org/10.1088/1755-1315/376/1/012054`.

[53] Y. H. Aruntaş, M. Tokyay. Central Anatolian diatomites for producing pozzolanic cements. In *1st International Symposium on Mineral Admixtures in Cement*, pp. 193–197. 1997.

[54] K. Toklu, O. Şimşek, H. Y. Aruntaş. Investigation of the usability of high-performance fiber-reinforced cement composites containing high-volume fly ash and nanomaterials as repair mortar. *Journal of the Australian Ceramic Society* **55**(3):789–797, 2019. `https://doi.org/10.1007/s41779-018-00291-6`.

[55] O. Gencel, O. Yavuz Bayraktar, G. Kaplan, et al. Characteristics of hemp fibre reinforced foam concretes with fly ash and Taguchi optimization. *Construction and Building Materials* **294**:123607, 2021. `https://doi.org/10.1016/j.conbuildmat.2021.123607`.

[56] G. Kaplan, S. A. Yildizel, S. Memiş, A. U. Öztürk. The optimization of calcareous fly ash-added cement containing grinding aids and strength-improving additives. *Advances in Civil Engineering* **2018**:8917059, 2018. `https://doi.org/10.1155/2018/8917059`.

[57] Y. H. Aruntaş, M. Tokyay. Katkılı Çimento Üretiminde Diyatomitin Puzolanik Malzeme Olarak Kullanılabilirliği. *Çimento ve Beton Dünyası* **1**(4):33–41, 1996.

[58] O. Y. Bayraktar. The possibility of fly ash and blast furnace slag disposal by using these environmental wastes as substitutes in portland cement. *Environmental Monitoring and Assessment* **191**(9):560, 2019. `https://doi.org/10.1007/s10661-019-7741-4`.

[59] Y. H. Aruntaş, M. Albayrak, A. H. Saka, M. Tokyay. Ankara-Kızılcahamam ve Çankırı-Çerkeş Yöresi Diyatomitlerinin Özelliklerinin Araştırılması. *The Turkish Journal of Engineering and Environmental Sciences* **22**:337–343, 1998.

[60] American Society for Testing and Materials. Standard specification for portland cement (ASTM Standard No. C150/C150M-22), 2019.

[61] American Society for Testing and Materials. Standard specification for coal fly ash and raw or calcined natural pozzolan for use in concrete (ASTM Standard No. C618-17a), 2014.

[62] American Society for Testing and Materials. Standard specification for slag cement for use in concrete and mortars (ASTM Standard No. C989), 2014.

[63] American Society for Testing and Materials. Standard specification for concrete aggregates (ASTM Standard No. C33-16), 2018.

[64] European Committee for Standardization. Concrete - part 1: Specification, performance, production and conformity (EN Standard No. 206-1), 2006.

[65] The British Standards Institution. Methods of testing cement – Part 3: Determination of setting times and soundness (BS Standard No. BS EN 196-3), 2016.

[66] The British Standards Institution. Testing fresh concrete (Part 2) – Slump test and Vebe test (BS Standard No. BS EN 12350-22009), 2009.

[67] American Society for Testing and Materials. Standard test method for air content of freshly mixed concrete by pressure method (ASTM Standard No. C231/C231M-17a), 2017.

[68] American Society for Testing and Materials. Standard test method for density (unit weight), yield, and air content (gravimetric) of concrete (ASTM Standard No. C138/C138M), 2012.

[69] American Society for Testing and Materials. Standard test method for compressive strength of cylindrical concrete specimens (ASTM Standard No. C39/C39M-18), 2018.

[70] American Society for Testing and Materials. Standard test method for abrasion resistance of concrete or mortar surfaces by the rotating-cutter method (ASTM Standard No. C944/C944M-19), 2020.

[71] M. Hasan, T. Saidi. Properties of blended cement paste with diatomite from Aceh Province Indonesia. *IOP Conference Series: Materials Science and Engineering* **796**(1):012034, 2020. `https://doi.org/10.1088/1757-899X/796/1/012034`.

[72] D. Kastis, G. Kakali, S. Tsivilis, M. G. Stamatakis. Properties and hydration of blended cements with calcareous diatomite. *Cement and Concrete Research* **36**(10):1821–1826, 2006. `https://doi.org/10.1016/j.cemconres.2006.05.005`.

[73] S. K. Das, J. Mishra, S. K. Singh, et al. Characterization and utilization of rice husk ash (RHA) in fly ash - Blast furnace slag based geopolymer concrete for sustainable future. *Materials Today: Proceedings* **33**(Part 8):5162–5167, 2020. `https://doi.org/10.1016/j.matpr.2020.02.870`.

[74] J. Liu, J. Li, J. Ye, F. He. Setting behavior, mechanical property and biocompatibility of anti-washout wollastonite/calcium phosphate composite cement. *Ceramics International* **42**(12):13670–13681, 2016. `https://doi.org/10.1016/j.ceramint.2016.05.165`.

[75] J. J. Zheng, J. Zhang, G. W. Scherer. Prediction of the degree of hydration at initial setting time of cement paste with particle agglomeration. *Cement and Concrete Research* **42**(9):1280–1285, 2012. `https://doi.org/10.1016/j.cemconres.2012.05.020`.

[76] S. U. Khan, M. F. Nuruddin, T. Ayub, N. Shafiq. Effects of different mineral admixtures on the properties of fresh concrete. *The Scientific World Journal* **2014**:986567, 2014. `https://doi.org/10.1155/2014/986567`.

[77] N. Dave, A. K. Misra, A. Srivastava, S. K. Kaushik. Setting time and standard consistency of quaternary binders: The influence of cementitious material addition and mixing. *International Journal of Sustainable Built Environment* **6**(1):30–36, 2017. `https://doi.org/10.1016/j.ijsbe.2016.10.004`.

[78] J. Aparicio, J. Barbero, M. Kapelko, et al. Testing the consistency and feasibility of the standard Malmquist-Luenberger index: Environmental productivity in world air emissions. *Journal of Environmental Management* **196**:148–160, 2017. `https://doi.org/10.1016/j.jenvman.2017.03.007`.

[79] D. H. Le, Y. N. Sheen, M. N. T. Lam. Fresh and hardened properties of self-compacting concrete with sugarcane bagasse ash–slag blended cement. *Construction and Building Materials* **185**:138–147, 2018. `https://doi.org/10.1016/j.conbuildmat.2018.07.029`.

[80] M. A. Nawaz, L. A. Qureshi, B. Ali, A. Raza. Mechanical, durability and economic performance of concrete incorporating fly ash and recycled aggregates. *SN Applied Sciences* **2**(2):162, 2020. `https://doi.org/10.1007/s42452-020-1960-8`.

[81] J. Pokorny, M. Zaleska, M. Pavlikova, Z. Pavlik. Properties of fine-grained concrete with admixture of diatomite powder. *IOP Conference Series: Materials Science and Engineering* **603**(2):022045, 2019. `https://doi.org/10.1088/1757-899X/603/2/022045`.

[82] F. U. A. Shaikh, A. Hosan. Effect of nano silica on compressive strength and microstructures of high volume blast furnace slag and high volume blast furnace slag-fly ash blended pastes. *Sustainable Materials and Technologies* **20**:e00111, 2019. `https://doi.org/10.1016/j.susmat.2019.e00111`.

[83] E. Özbay, M. Erdemir, H. I. Durmuş. Utilization and efficiency of ground granulated blast furnace slag on concrete properties - A review. *Construction and Building Materials* **105**:423–434, 2016. `https://doi.org/10.1016/j.conbuildmat.2015.12.153`.

[84] N. Bouzoubaâ, M. Lachemi. Self-compacting concrete incorporating high volumes of class F fly ash: Preliminary results. *Cement and Concrete Research* **31**(3):413–420, 2001. `https://doi.org/10.1016/S0008-8846(00)00504-4`.

[85] Z. Ahmadi, J. Esmaeili, J. Kasaei, R. Hajialioghli. Properties of sustainable cement mortars containing high volume of raw diatomite. *Sustainable Materials and Technologies* **16**:47–53, 2018. `https://doi.org/10.1016/j.susmat.2018.05.001`.

[86] V. Letelier, E. Tarela, P. Muñoz, G. Moriconi. Assessment of the mechanical properties of a concrete made by reusing both: Brewery spent diatomite and recycled aggregates. *Construction and Building Materials* **114**:492–498, 2016. `https://doi.org/10.1016/j.conbuildmat.2016.03.177`.

[87] O. Gencel, F. Koksal, C. Ozel, W. Brostow. Combined effects of fly ash and waste ferrochromium on properties of concrete. *Construction and Building Materials* **29**:633–640, 2012. `https://doi.org/10.1016/j.conbuildmat.2011.11.026`.

[88] S. Sujjavanich, P. Suwanvitaya, D. Chaysuwan, G. Heness. Synergistic effect of metakaolin and fly ash on properties of concrete. *Construction and Building Materials* **155**:830–837, 2017. `https://doi.org/10.1016/j.conbuildmat.2017.08.072`.

[89] M. K. Ismail, A. A. Hassan. Abrasion and impact resistance of concrete before and after exposure to freezing and thawing cycles. *Construction and Building Materials* **215**:849–861, 2019. `https://doi.org/10.1016/j.conbuildmat.2019.04.206`.

[90] C. D. Atiş. High volume fly ash abrasion resistant concrete. *Journal of Materials in Civil Engineering* **14**(3):274–277, 2002. `https://doi.org/10.1061/(asce)0899-1561(2002)14:3(274)`.

[91] K. Amini, H. Ceylan, P. C. Taylor. Effect of curing regimes on hardened performance of concrete containing slag cement. *Construction and Building Materials* **211**:771–778, 2019. `https://doi.org/10.1016/j.conbuildmat.2019.03.273`.

Acta Polytechnica **62**(5):522–530, 2022
`https://doi.org/10.14311/AP.2022.62.0522`

EXTRA CONTROL COEFFICIENT ADDITIVE ECCA-PID FOR CONTROL OPTIMIZATION OF ELECTRICAL AND MECHANIC SYSTEM

Erol Can

Erzincan Binali Yıldırım University, School of Civil Aviation, Department of Aviation Electric-Electronics, Erzincan, Turkey

correspondence: `cn_e@hotmail.com`

Abstract.

Proportional Integral Derivative (PID) controllers are frequently used control methods for mechanical and electrical systems. Controller values are chosen either by calculation or by experimentation to obtain a satisfactory response in the system and to optimise the response. Sometimes the controller values do not quite capture the desired system response due to incorrect calculations or approximate entered values. In this case, it is necessary to add features that can make a comparison with the existing traditional system and add decision-making features to optimise the response of the system. In this article, the decision-making unit created for these control systems to provide a better control response and the PID system that contributes an extra control coefficient called ECCA-PID is presented. First, the structure and design of the traditional PID control system and the ECCA-PID control system are presented. After that, ECCA-PID and traditional PID methods' step response of a quadratic system are examined. The results obtained show the effectiveness of the proposed control method.

Keywords: ECCA-PID, decision-making unit, satisfactory response.

1. Introduction

PID (proportional-integral-derivative) controller control loop method is a control mechanism that has a wide range of uses, such as electronic devices, mechanical devices and pneumatic systems [1–4]. The PID compares the signal sent to the input via the feedback path with the input signal and calculates the error obtained. The PID control system compares the reference signal of input with sensing the output signal of controlled plant via the feedback path. Then, the controller system calculates the error of the obtained signal. This error is sent to P, I, D and after the controller units multiplies this error with a coefficient, it sends new created signals to the input of the target plant system [5, 6]. This process is repeated until the error reaches a minimum value. While PID control studies generally focus on linear systems, studies on a good-performing PID controller are also presented for some system groups with uncertainty [7, 8]. The balancing of the first order time-delayed system using a PID controller with the previously given PID values has been investigated [9, 10] While high order time delay systems are controlled by PID [11–13]. In some studies, it relies on testing the negative feedback control system in continuous oscillation with a step input to calculate the PID gain values. Initially, the integral and derivative terms are disabled by making the gains of zero in the PID controller, and the controller is operated with only a proportional effect. A step input is applied to the input of the system and the K_p gain is increased from zero until a continuous and same amplitude oscillation is obtained at the output of the system [12, 13]. The gain K_p giving sustained oscillation is determined as the sustained oscillation period in seconds. Forcing this method to reach the constant oscillation region may have undesirable results in some applications. Against external factors, the process can easily pass into the unstable region. Therefore, some physical damage to the equipment may occur. It takes a lot of experimentation to calculate its value. However, in some systems, predetermined insufficient controller values may be insufficient to provide the desired stabilisation times. In order to eliminate such situations, an extra control coefficient additive (ECCA)-PID control is recommended, which is based on all these principles, but which can activate the system faster and stabilise the system by providing a shorter settling time. The ideal reference signal is divided into reflection reference values of different magnitudes to form a decision unit to be compared with the error and error change rates. Therefore, extra controller coefficients are produced by observing the error and error rate of change and comparing it with the reflection reference part values of different sizes. It is aimed to provide a faster optimisation with a semi-linear control independently of the controller coefficients entered into the system before. First, the ECCA-PID design working logic is given. Then, in the implementation phase, Conventional PID and Proposed PID are applied to the transfer function of a second-order system and the step response is examined. The ideal response parts expected with the proposed system are tested at the reflection reference values 0–0.5 and 0–1 and the step responses are measured. Considering the results obtained, the proposed method can reach the ideal control point in a very short time, while the traditional system is far from the desired response.

2. Design with PID controller

Although the PD control from three controllers brings attenuation to the system, it does not affect the steady state behaviour of the system. The PI controller, however, increases the relative stability as well as the rise time, although it corrects the steady-state errors. These results lead to the use of PID control, with the use of a combination of PI and PD controllers. K_p, K_i, K_d define the proportional, integral and derivative gain coefficients, respectively. A PID controller consists of PI and PD parts connected in series. The closed loop control scheme for a PID control is given in Figure 1, with e being the error of the output signal, r is the references value.

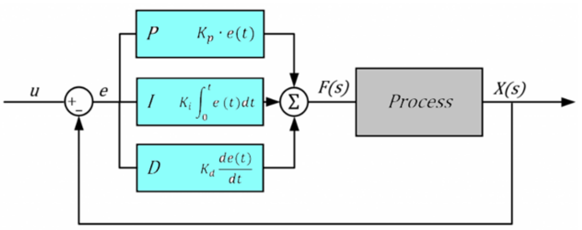

Figure 1. The closed loop control scheme for PID.

While the transfer function of PID controller is as below:

$$u(t) = e(t) * K_p + K_i \frac{\mathrm{de}(t)}{\mathrm{dt}} + K_i \int_0^t e(t)\, dt \quad (1)$$

$$e(t) = r(t) - y(t) \quad (2)$$

Open-loop techniques rely on the results of a bump or step test in which the output of the controller is abruptly manually forced by cancelling the feedback. The graphical slice of the trailing trajectory of the process variable is given in Figure 2 in [10], the curve known as the reaction curve. The sloping line drawn tangent to the steepest point of the reaction curve demonstrates how fast the process reacts to the step change of the controller output. The inverse of the slope of this line, T, which is the measure of the severity of the delay, is the time constant of the process. The reaction curve is also: the dead time (d), which shows how long it takes for the process to give the initial reaction of the process, and the process gain (K), how much the process variable increases according to the size of the step. Ziegler and Nichols determined, by trial and error, that the best values of the tuning parameters P, $\mathrm{T_i}$, and $\mathrm{T_d}$ can be calculated from the T, d, and K values as follows [12, 13]. P is 1.2 T/K_d, $\mathrm{T_i}$ is 2d, $\mathrm{T_d}$ is 0.5d.

A closed-loop technique executes the controller in an automatic mode but with integral and derivative

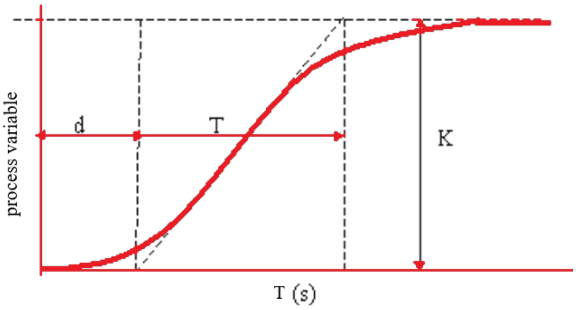

Figure 2. Open loop curve.

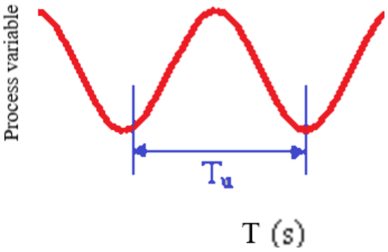

Figure 3. Curve for a closed-loop.

turned off. As seen in Figure 3, the gain for the controller is boosted until the smallest error produces a continuous oscillation in the process variable. The gain of the smallest controller that causes an oscillation is named the final gain, $\mathrm{P_u}$. The period of these oscillations is also named the final period, $\mathrm{T_u}$. Appropriate tuning parameters are calculated from the following rules based on these two values [10].

As a results, P is 0.6 $\mathrm{P_u}$, $\mathrm{T_i}$ is 0.5 $\mathrm{T_u}$, $\mathrm{T_d}$ is 0.125 $\mathrm{T_u}$. Despite all these separations and arrangements, the gain K_p giving a sustained oscillation is determined as the sustained oscillation period in seconds. Forcing this method to reach the constant oscillation region may have undesirable results in some applications. The process can move to the unstable region very easily against external factors. Thus, some physical damage to the equipment may occur. So, the ECCA-PID method offers a good alternative to avoid these complex and inconvenient situations of traditional methods. In order to provide a more optimum control, the response expected from the system is divided into partial sizes and compared again with the error obtained, the error and error change rates produced for the control are evaluated, and new coefficients are created to be added to the controller coefficients of the controllers, thus enabling the system to give a better one. $K \in \mathbb{Z}^+ \rightarrow K = \{K_1, K_2, K_3, \ldots, K_n\}$, In order to find the value that will provide the desired control in Rr, the value is to be compared with the error produced by the system; virtual part reference value is $Rr \in \mathbb{R}^+ \rightarrow Rr = \{Rr_1, Rr_2, \ldots, Rr_n\}$, The K values to be produced can be found as follows.

If $e_1 > Rr_1$ *then* K_1

If $K_1 > 0$ *then* $K_p + K_1$ *and* $K_i + K_1$ *and* $K_d + K_1$

If $e_2 > Rr_2$ *then* K_2

If $K_2 > 0$ *then* $K_p + K_2$ *and* $K_i + K_2$ *and* $K_d + K_2$

If $e_n > Rr_n$ *then* K_n

If $K_n > 0$ *then* $K_p + K_n$ *and* $K_i + K_n$ *and* $K_d + K_n$

Unlike other swarm optimization and traditional PID control methods, the proposed method produces linear movements to approach the desired value whenever it is far from the desired value, and in this case, the desired control can be achieved more quickly. Extra control coefficient (ECCA)-PID control is given in Figure 4a while Figure 4b shows the mesh depicting the interaction of the reference and reflection reference values that will contribute to the extra coefficient. The control gains predicted by the decision-making unit can be expressed as the following equations.

$$\begin{aligned} u(t_1) = e(t_1) * (K_p + K_1) + (K_d + K_1)\frac{\mathrm{d}e(t_1)}{\mathrm{d}t} \\ + (K_i + K_1)\int_0^{t_1} e(t_1)\,dt \end{aligned} \tag{3}$$

$$\begin{aligned} u(t_2) = e(t_2) * (K_p + K_2) + (K_d + K_2)\frac{\mathrm{d}e(t_2)}{\mathrm{d}t} \\ + (K_i + K_2)\int_0^{t_2} e(t_2)\,dt \end{aligned} \tag{4}$$

$$\begin{aligned} u(t_n) = e(t_n) * (K_p + K_n) + (K_d + K_n)\frac{\mathrm{d}e(t_n)}{\mathrm{d}t} \\ + (K_i + K_n)\int_0^{t_n} e(t_n)\,dt \end{aligned} \tag{5}$$

If there is too much overshoot and oscillation in the system, the decision-making order of the proposed method can be arranged as follows.

If $e_1 > Rr_1$ *then* K_1

If $K_1 > 0$ *then* $K_p + K_1$ *and* $K_i + K_1$ *and* $K_d + K_1$

Else if $e_1 < Rr_1$ *then* K_{11}

If $K_{11} > 0$ *then* $K_p - K_{11}$ *and* $K_i - K_{11}$ *and* $K_d - K_1$

If $e_2 > Rr_2$ *then* K_2

If $K_2 > 0$ *then* $K_p + K_2$ *and* $K_i + K_2$ *and* $K_d + K_2$

Else if $e_2 < Rr_2$ *then* K_{22}

If $K_{22} > 0$ *then* $K_p - K_2$ *and* $K_i - K_2$ *and* $K_d - K_2$

If $e_n > Rr_n$ *then* K_n

If $K_n > 0$ *then* $K_p + K_n$ *and* $K_i + K_n$ *and* $K_d + K_n$

Else if en $< Rr_{nn}$ *then* K_{nn}

If $K_n > 0$ *then* $K_p - K_{nn}$ *and* $K_i - K_{nn}$ *and* $K_d - K_{nn}$

e is error, de is error change, $e \in \mathbb{R} \rightarrow e = \{e_1, e_2, \ldots, e_n\}$, $de \in \mathbb{R} \rightarrow de = \{de_1, de_2, \ldots, de_n\}$, e and de are expressed as below.

$$e(t_1) = r(t) - y(t_1) \tag{6}$$

$$K_1 = e(t_1) - Rr_1 \tag{7}$$

$$e(t_2) = r(t) - y(t_2) \tag{8}$$

$$K_2 = e(t_2) - Rr_2 \tag{9}$$

$$de_1 = e(t_2) - e(t_1) \tag{10}$$

$$e(t_{n-1}) = r(t) - y(t_{n-1}) \tag{11}$$

$$K_{n-1} = e(t_{n-1}) - Rr_{n-1} \tag{12}$$

$$de_{n-1} = e(t_{n-1}) - e(t_{n-2}) \tag{13}$$

$$e(t_{n-1}) = r(t) - y(t_{n-1}) \tag{14}$$

$$K_{n-1} = e(t_n) - Rr_{n-1} \tag{15}$$

$$e(t_n) = r(t) - y(t_n) \tag{16}$$

$$K_n = e(t_n) - Rr_n \tag{17}$$

Considering the error e_c for a conventional PID control and the effect of the proposed method on the error of the conventional method e_k, $e(t)$ can be arranged as follows.

$$e(t) = e_c + e_k \tag{18}$$

The general equation for the PID can be arranged as follows.

$$\begin{aligned} u(t_1) &= (e_{c1} + e_{k1})(t_1) * (K_p + K_1) \\ &+ (K_i + K_1)\frac{(\mathrm{d}e_{c1} + \mathrm{d}e_{k1})(t1)}{\mathrm{d}t} \\ &+ (K_i + K_1)\int_0^{t_1} (e_{c1} + e_{k1})(t_1)\,dt \end{aligned} \tag{19}$$

$$\begin{aligned} u(t_2) &= (e_{c2} + e_{k2})(t_2) * (K_p + K_2) \\ &+ (K_i + K_2)\frac{(\mathrm{d}e_{c2} + \mathrm{d}e_{k2})(t2)}{\mathrm{d}t} \\ &+ (K_i + K_2)\int_0^{t_2} (e_{c2} + e_{k2})(t_2)\,dt \end{aligned} \tag{20}$$

$$\begin{aligned} u(t_n) &= (e_{cn} + e_{kn})(t_n) * (K_p + K_n) \\ &+ (K_i + K_n)\frac{(\mathrm{d}e_{cn} + \mathrm{d}e_{kn})(t_n)}{\mathrm{d}t} \\ &+ (K_i + K_n)\int_0^{tn} (e_{cn} + e_{kn})(t_n)\,dt \end{aligned} \tag{21}$$

Depending on whether the error is positive or negative, the control diagram of the system is as in Figure 5, in line with the above explanation of the decision-making unit. The equation of the second order and PID system is given in Equation (22).

$$\frac{X(s)}{F(s)} = \frac{1}{0.5s^2 + s + 1} \tag{22}$$

The PID control is applied to the system to be tested as in Equation (23).

$$\frac{X(s)}{F(s)} = \frac{K_d \cdot s^2 + K_p \cdot s + K_i}{(0.5 + K_d)s^2 + K_p \cdot s + K_i} \tag{23}$$

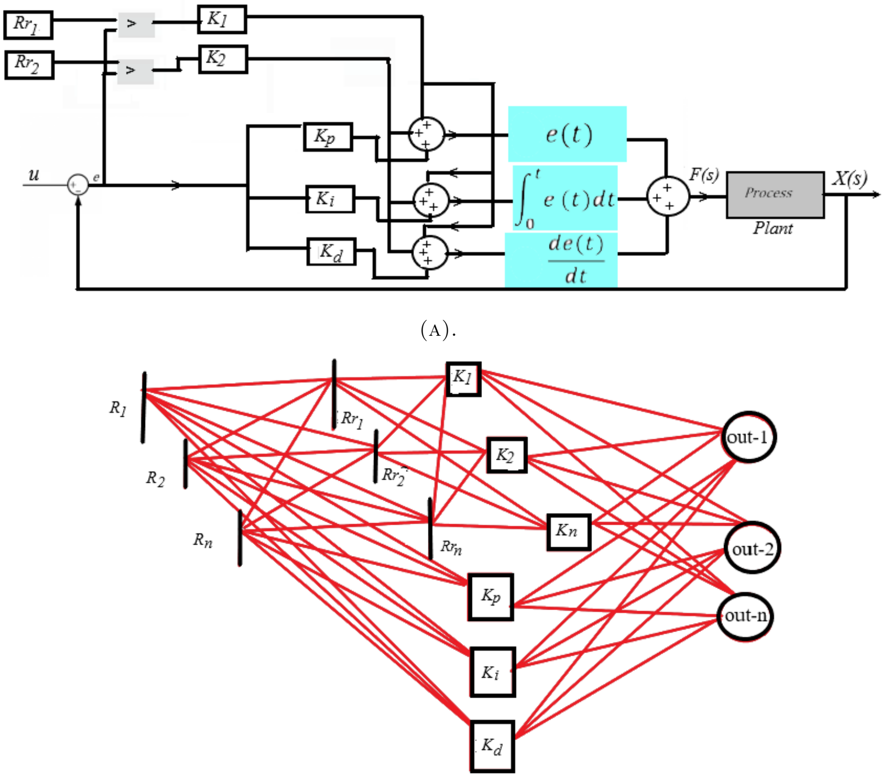

(a).

(b).

Figure 4. a) extra control coefficient (ECCA)-PID control, b) relation network between R and Rr.

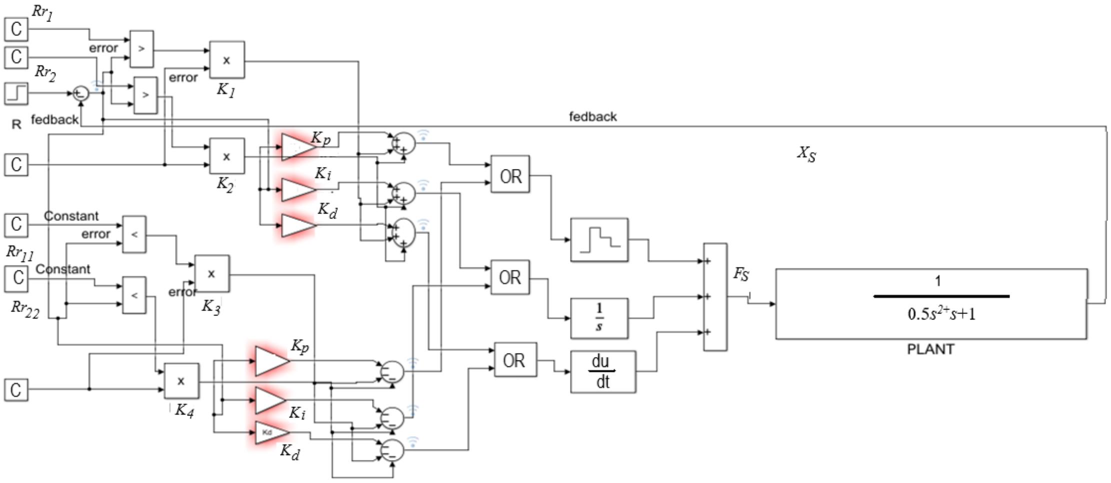

Figure 5. The control diagram of the system, depending on whether the error is positive or negative.

Equation (24) and Equation (25) give the fixed value contributions to the controller systems as a result of the comparison of the reflection reference values in the decision-making unit of the proposed system with the actual controller coefficient values.

$$\frac{X(s)}{F(s)} = \frac{(K_d + K_1)\cdot s^2(K_p + K_1)\cdot s + (K_i + K_1)}{(0.5 + (K_d + K_1))\cdot s^2 + (K_p + K_1)\cdot s + (K_i + K_1)} \tag{24}$$

$$\frac{X(s)}{F(s)} = \frac{(K_d - K_1)\cdot s^2(K_p - K_1)\cdot s + (K_i - K_1)}{(0.5 + (K_d - K_1))\cdot s^2 + (K_p - K_1)\cdot s + (K_i - K_1)} \tag{25}$$

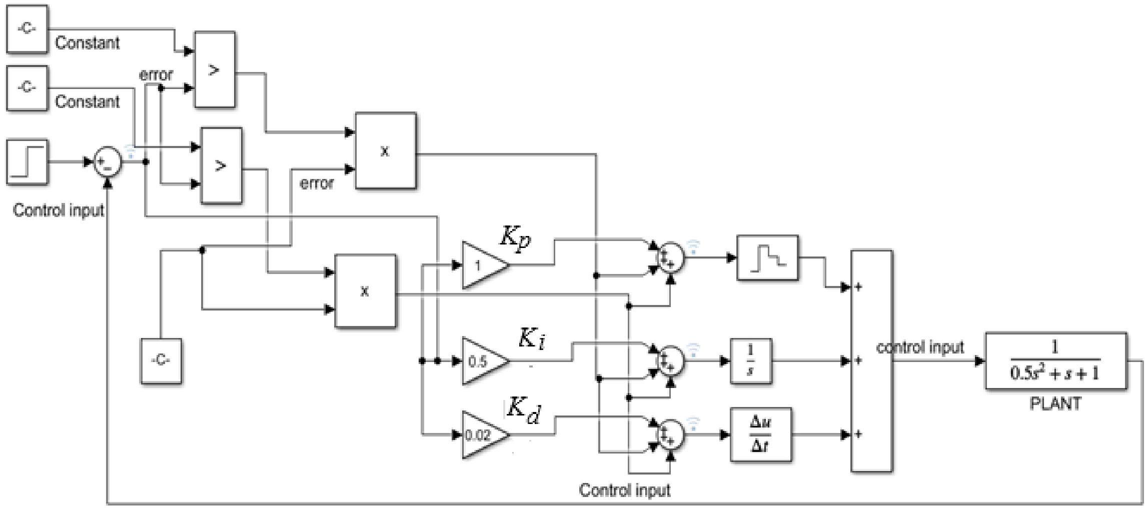

Figure 6. The MATLAB Simulink model of the designed system.

3. (ECCA)-PID control application

The proposed system is examined over the step response of a second-order system such as $[(1/(0.5s^2 + s + 1)]$. The MATLAB Simulink model of the designed system is given in Figure 6. In the second order system, both traditional PID control method and (ECCA)-PID Control are applied. Figure 7a shows the step response values when two *Rr* values such as 0–0.5 are given to the proposed system for the step response of the system. While the extra gain values produced by the controller decision unit are given in Figure 7b, the controller output signal and controller errors can be seen in Figure 8. K_p is 1, K_i is 0.5, K_d is 0.02, e is error.

While the rise moment response of the system is as short as 0.1 s for ECCA-PID and ECCA-P, the rise moment response of the system for a traditional PID control is 1.1 s. This means that the rise moment response of the proposed system corresponds to 9 % of the take-off response of a traditional PID controlled system. The settling time for ECCA-P cannot occur in 10 s, but when I-D controllers are added to the total control system, the settling time takes place in 5 s for ECCA-PID. When the system is controlled with a traditional PID, the system is not capable of settling in 10 s. This shows that the desired control can be achieved with the decision-making unit of the proposed system, even if insufficient controller coefficients are selected for the system. *Rr* values in the range of 0–0.5 taken into consideration by the decision-making unit are trying to reach the desired control point. While the gain factor is increased between 0–1 s and 5.4–8.4 s for *Rr* 0, the gain factor is increased between 0–1 s and 2–10.4 s for *Rr* 0.5. The controller output signal becomes stable in 4 s. For the proposed control system, the controller error ends in 5 s, while for the ECCA-P and traditional PID method, the error does not end for 10 s.

Figure 9a shows the step response values when two *Rr* values such as 0–1 are given to the proposed system for the step response of the system. While the extra gain values produced by the controller decision unit are given in Figure 9b, the controller output signal and controller errors can be seen in Figure 10. K_p is 1, K_i is 0.5, K_d is 0.02.

While the rise moment response of the system for *Rr* of 0–1 is as short as 0.1 s for ECCA-PID and ECCA-P, the rise moment response of the system for a traditional PID control is 1.1 s. This means that the rise moment response of the proposed system corresponds to 9 % of the take-off response of a traditional PID controlled system. The settling time for ECCA-P cannot occur in 10 s, but when I-D controllers are added to the total control system, the settling time takes place in 4 s for ECCA-PID. When the system is controlled with a traditional PID, the system is not capable of settling in 10 s. This shows that the desired control can be achieved with the decision-making unit of the proposed system, even if insufficient controller coefficients are selected for the system. *Rr* values in the range of 0–1 taken into consideration by the decision-making unit are trying to reach the desired control point. While the gain factor is increased between 0–1 s and 3.9–7 s for *Rr* of 0, the gain factor is increased between 0–10 s for *Rr* of 1. While the controller output signal becomes stable in 4 s, It deviates from the ideal control reference value between 2 and 4 s. For the proposed control system, the controller error ends in 4 s, while for the ECCA-P and traditional PID method, the error does not end for 10 s.

Figure 11 shows the step responses and the extra gain values produced by the controller decision unit for *Rr* 0–0.3. There are controller output signal and controller errors for 0–0.3. The rise moment response of the system for *Rr* of 0–0.3 is as short as 0.1 s for ECCA-PID and ECCA-P, the rise moment response of the system for a traditional PID control is 1.1 s.

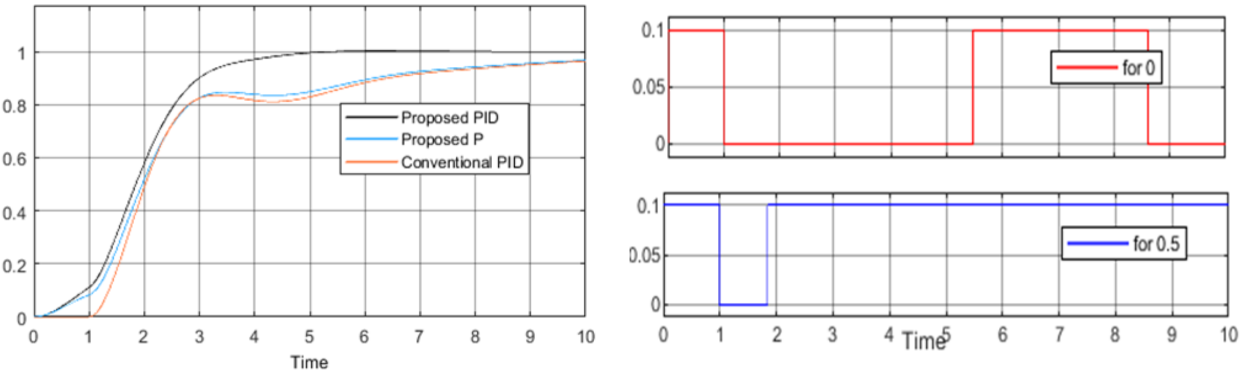

(a). (b).

Figure 7. For Rr of 0–0.5 $> e$: a) the step responses, b) the extra gain values produced by the controller decision unit.

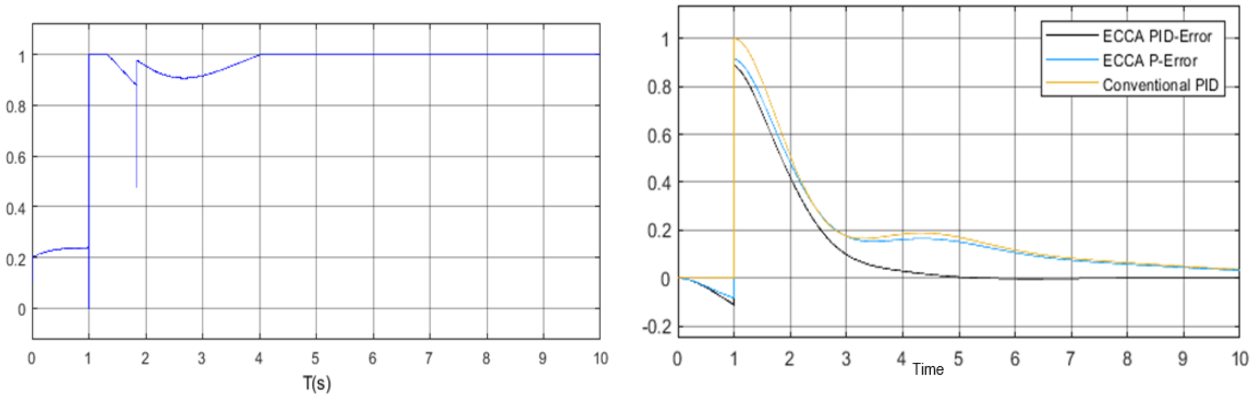

(a). (b).

Figure 8. a) The controller output signal, b) errors for controllers.

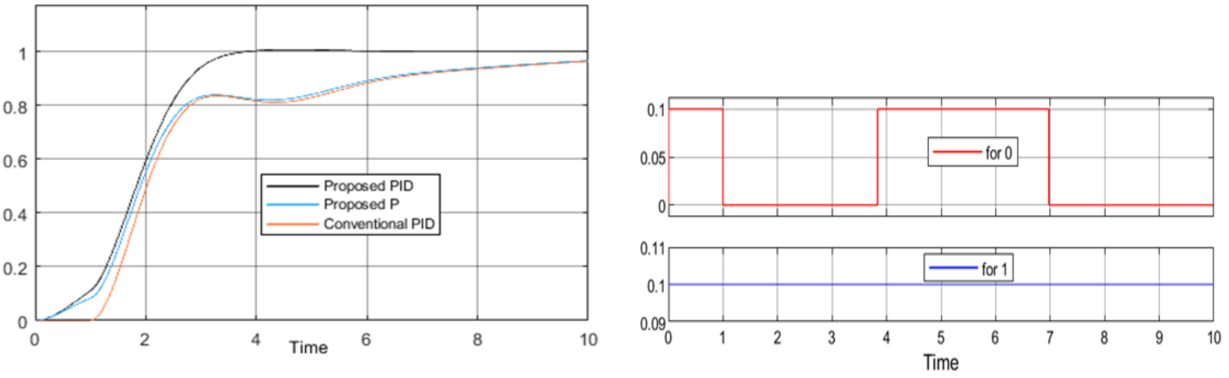

(a). (b).

Figure 9. For Rr of 0–1 $> e$: a) the step responses, b) the extra gain values produced by the controller decision unit.

The 0–0.3 Rr range in ECCA-P provides an earlier rise as compared to the 0–1 range. The settling tim for ECCA-P cannot occur in 10 s, but when I-D controllers are added to the total control system, the settling time takes place in 4 s for ECCA-PID. When the system is controlled with a traditional PID, the system is not capable of settling in 10 s. This shows that the desired control can be achieved with the decision-making unit of the proposed system, even if insufficient controller coefficients are selected for the system. Rr values in the range of 0–0.3 taken into consideration by the decision-making unit are trying to reach the desired control point. While the gain factor is increased between 0–1 s and 5.5–8.7 s for Rr of 0, the gain factor is increased between 0–1 s and 1.2–10 s for Rr of 0. After the maximum collapse occurs in 2.2 s, the controller output signal becomes stable in 4 s. For the proposed control system, the

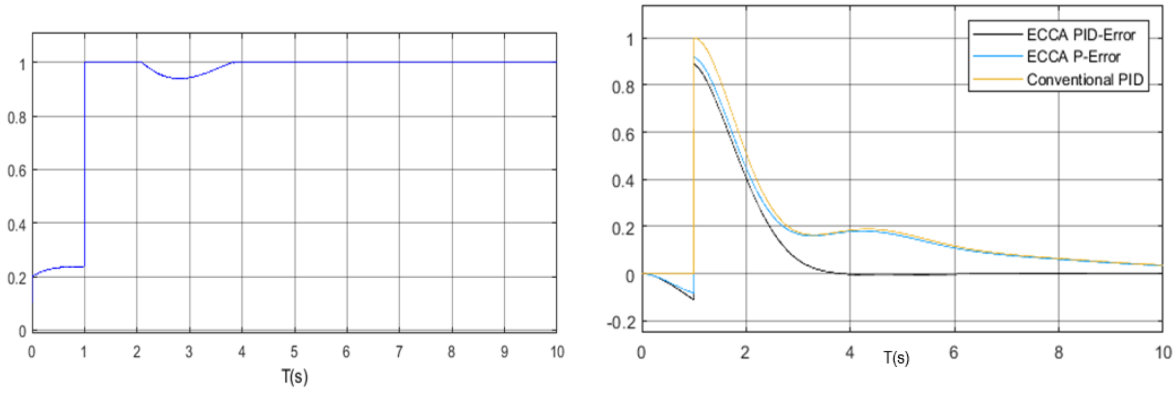

(a).

(b).

Figure 10. a) the controller output signal, b) controller errors.

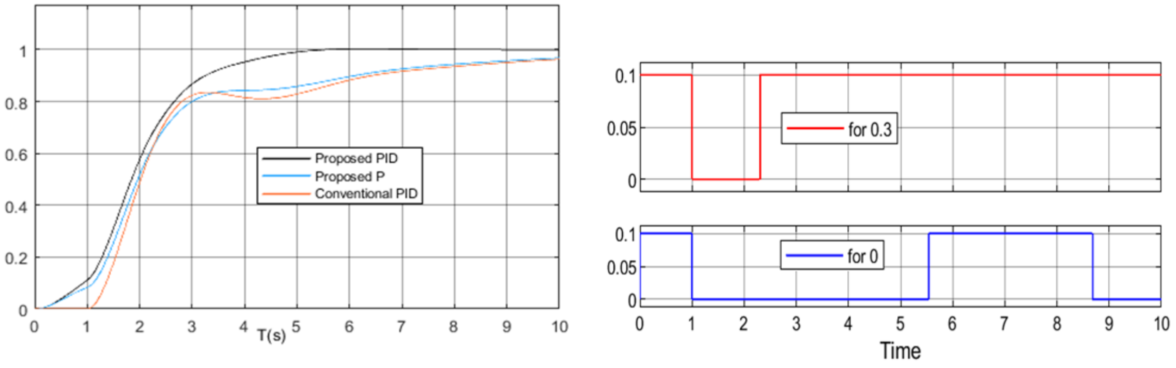

(a).

(b).

Figure 11. For Rr of 0–0.3 $> e$: a) the step responses, b) the extra gain values produced by the controller decision unit.

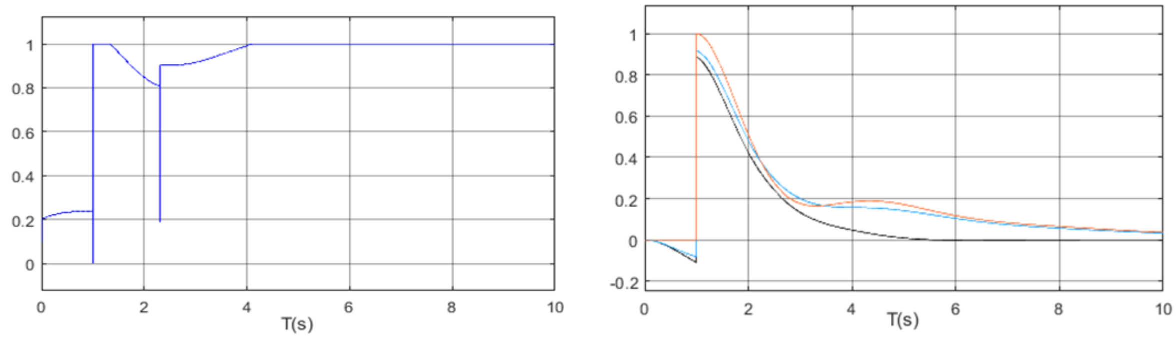

(a).

(b).

Figure 12. a) the controller output signal for 0–0.3, b) controller errors.

controller error ends in 6 s, while for the ECCA-P and traditional PID method, the error does not end for 10 s.

Figure 13 shows the step response of the system controlled with ECCA-PID and the controller errors for different Rr values. Figure 14 shows the step response of the system control with ECCA-P and the controller errors for different Rr values.

ECCA-PID and ECCA-P are tested for control of a quadratic system. Even if the previously determined controller coefficient constants are insufficient or not entered at all, the system controlled by ECCA-PID produces values that will contribute to the controller system by making comparisons with the actual error of the system for different reflection Rr values in the decision-making unit. Thus, unlike traditional PID controllers with linear response, the error variation affects the error variation in a semi-linear manner, independent of the controller coefficients entered into the system before, and brings the control of the system to a satisfactory level.

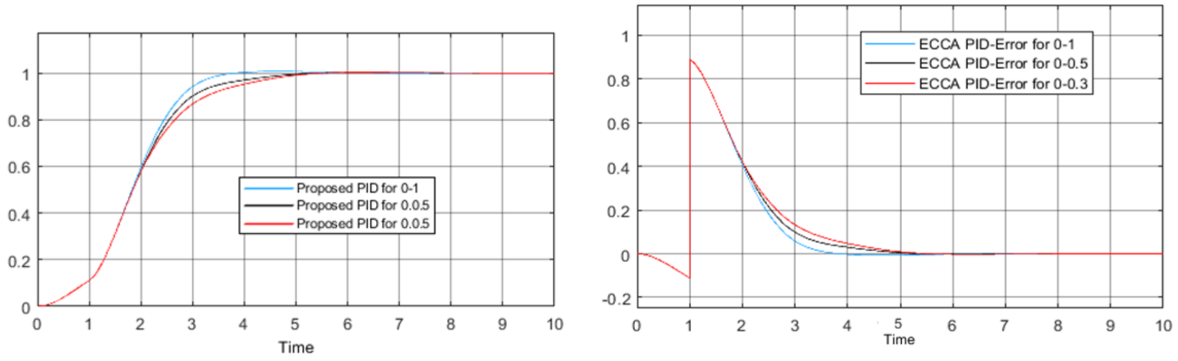

(a). (b).

Figure 13. With ECCA-PID: a) the step response of the system controlled, b) the controller errors for different Rr values.

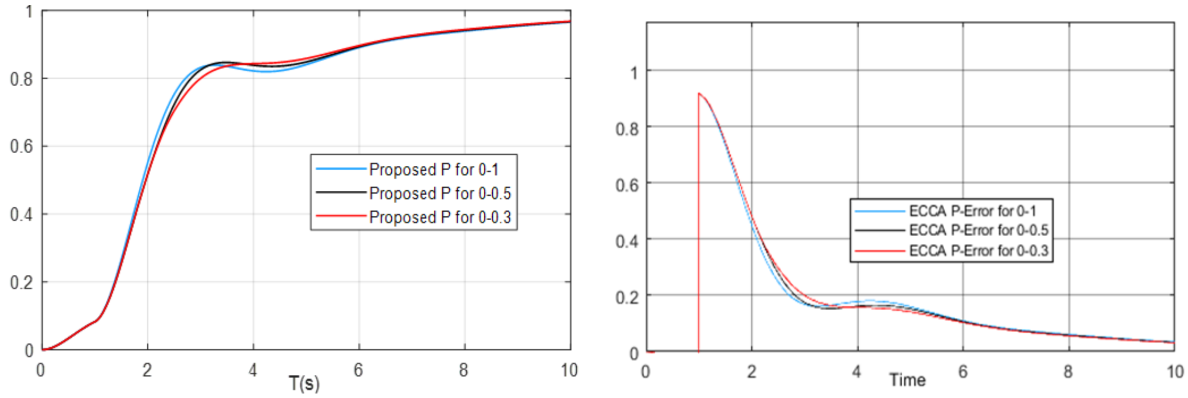

(a). (b).

Figure 14. With ECCA-P: a) the step response of the system controlled, b) the controller errors for different Rr values.

4. Conclusions

In this article, a PID control with extra gain is developed. The structure and design of the traditional PID control system and the ECCA-PID control system are presented. Then, the step response of a second-order system with the conventional method is examined. In the control processes for Rr of 0–5 and Rr of 0–1 values, the proposed system responds in 0.1 s for the moment of rise, while the traditional PID method responds in 1.1 s. Again, while ECCA-PID provides settling time at 4 s and 5 s, traditional PID cannot provide settling at 10 s. This shows the effectiveness of the proposed system and its contribution to the control systems. Therefore, it seems to be an ideal method for energy conversion systems and motor control units.

References

[1] H. Wang, L. Jinbo. Research on fractional order fuzzy PID control of the pneumatic-hydraulic upper limb rehabilitation training system based on PSO. *International Journal of Control, Automation and Systems* **20**(3):210–320, 2022. `https://doi.org/10.1007/s12555-020-0847-1`.

[2] M. N. Muftah, A. A. M. Faudzi, S. Sahlan, M. Shouran. Modeling and fuzzy FOPID controller tuned by PSO for pneumatic positioning system. *Energies* **15**(10):3757, 2022. `https://doi.org/10.3390/en15103757`.

[3] E. Can, H. H. Sayan. The performance of the DC motor by the PID controlling PWM DC-DC boost converter. *Tehnički glasnik* **11**(4):182–187, 2017.

[4] E. Can, M. S. Toksoy. A flexible closed-loop (fcl) pid and dynamic fuzzy logic + pid controllers for optimization of dc motor. *Journal of Engineering Research* 2021. Online first, `https://doi.org/10.36909/jer.13813`.

[5] J. Crowe, K. K. Tan, T. H. Lee, et al. *PID control: New identification and design methods*. Springer-Verlag London Limited, 2005.

[6] C. Knospe. PID control. *IEEE Control Systems Magazine* **26**(1):30–31, 2006. `https://doi.org/10.1109/MCS.2006.1580151`.

[7] M.-T. Ho, C.-Y. Lin. PID controller design for robust performance. *IEEE Transactions on Automatic Control* **48**(8):1404–1409, 2003. `https://doi.org/10.1109/TAC.2003.815028`.

[8] C. Zhao, L. Guo. Towards a theoretical foundation of PID control for uncertain nonlinear systems. *Automatica* **142**:110360, 2022. `https://doi.org/10.1016/j.automatica.2022.110360`.

[9] P. Patil, S. S. Anchan, C. S. Rao. Improved PID controller design for an unstable second order plus time delay non-minimum phase systems. *Results in Control and Optimization* **7**:100117, 2022. `https://doi.org/10.1016/j.rico.2022.100117`.

[10] E. S. Tognetti, G. A. de Oliveira. Robust state feedback-based design of PID controllers for high-order systems with time-delay and parametric uncertainties. *Journal of Control, Automation and Electrical Systems* **33**(2):382–392, 2022. `https://doi.org/10.1007/s40313-021-00846-2`.

[11] C. Cruz-Díaz, B. del Muro-Cuéllar, G. Duchén-Sánchez, et al. Observer-based PID control strategy for the stabilization of delayed high order systems with up to three unstable poles. *Mathematics* **10**(9):1399, 2022. `https://doi.org/10.3390/math10091399`.

[12] J. G. Ziegler, N. B. Nichols. Optimum settings for automatic controllers. *Journal of Dynamic Systems, Measurement, and Control* **115**(2B):220–222, 1993. `https://doi.org/10.1115/1.2899060`.

[13] S. Skogestad. Simple analytic rules for model reduction and PID controller tuning. *Journal of Process Control* **13**(4):291–309, 2003. `https://doi.org/10.1016/S0959-1524(02)00062-8`.

Acta Polytechnica **62**(5):531–537, 2022
`https://doi.org/10.14311/AP.2022.62.0531`

Published by the `Czech Technical University in Prague`

CONCRETE LINTELS REINFORCED WITH STEEL FIBRES ORIENTED BY A MAGNETIC FIELD

Kristýna Carrera[a], Karel Künzel[b], Petr Konrád[a,*], Radoslav Sovják[a], Václav Papež[b], Michal Mára[a], Jindřich Fornůsek[a], Přemysl Kheml[a]

[a] *Czech Technical University in Prague, Faculty of Civil Engineering, Experimental Centre, Thákurova 7, 166 29 Prague 6, Czech Republic*

[b] *Czech Technical University in Prague, Faculty of Electrical Engineering, Department of Electrotechnology, Technická 2, 166 27 Prague 6, Czech Republic*

[*] corresponding author: `petr.konrad@fsv.cvut.cz`

Abstract. This paper explores the possibility of applying the technique of magnetic orientation of steel fibres for manufacturing a concrete structural element of realistic dimensions, compared to small laboratory specimens. This technique could be a part of an answer to the current need for faster and automated production in the prefabrication industry. The examined specimens have dimensions of commonly used lintels in construction, 80 mm × 100 mm × 980 mm. The properties of specimens with magnetically oriented fibres are compared with same size specimens prefabricated conventionally. The orientation of fibres has been confirmed by Q-factor non-destructive testing method using a measuring coil. All specimens were tested with a four-point bending test. The specimens with oriented fibres show a significantly higher flexural strength, by 150 %, than specimens produced conventionally with the same volume of fibres.

Keywords: Magnetic, orientation, fibre, align, concrete, lintels, beams.

1. Introduction

During the production of cement, a large amount of CO_2 is produced, indirectly due to the energy consumption and directly because of the chemical reactions in the conversion of limestone to clinker [1]. With increasing demands to reduce the carbon footprint and speed up the production processes, new materials and technologies are being developed. However, another key aspect of the more sustainable use of cement is through manufacturing processes that result in significantly more efficient products. High-performance concrete (HPC) allows us to use less volume of the material to achieve the same required strengths while increasing the overall durability and longevity thanks to its resistance to the environment [2]. Fibre reinforcement also benefits from the use of HPC as a stronger fibre-matrix bond can be achieved for better efficiency [3].

This paper investigates the emerging technology for fibre orientation in fresh concrete using a magnetic field to manufacture a high-performance fibre-reinforced concrete (HPFRC). This increases the efficiency of the material even further, but the technology also has the potential to be fully automated in the future. One recent industry requirement is the speed and automation of production. Furthermore, the use of fibres specifically aligned as needed can present an alternative or replacement to conventional, labour-intensive steel-bar reinforcement. Although several authors have addressed the topic of magnetic orientation [4–9], none of them tested an element with realistic dimensions for a practical use in construction. In this paper, lintels of common dimensions were fabricated and experimentally tested.

Since the successful magnetic orientation is not immediately apparent, it must go hand in hand with a certain non-destructive evaluation that can confirm it. This is also a necessary step for a future automated industrial production, as quality control must be present. As part of the experimental campaign, a non-destructive method from previous studies [10] is also employed to test it with these larger specimens.

2. Materials and methods

2.1. Manufacturing of specimens

The mixture design of the HPFRC is in Table 1. It is used in combination with 1.5 % of volume of Weidacon FM high-strength steel fibres with a length of 13 mm and a diameter of 0.15 mm, which corresponds to an aspect ratio of 87. The mixture was prepared in a 50 l pan mixer. At first, all dry constituents were mixed for 3 minutes, then water with a high-range water-reducer (HRWR) was added and mixed for additional 10 minutes for the full activation of the used HRWR. Finally, steel fibres were sprinkled into the running mixer, to eliminate fibre clustering, which took 5 more minutes. The fresh HPFRC was poured by hand into the centres of plastic moulds to let the material flow into the whole volume (Figure 1). This ensured that all specimens were manufactured the same way.

Constituent	Rel. weight	kg/m^3
Cement 42.5 R	1.000	692.7
Water	0.281	194.5
Silica fume	0.110	76.2
Silica flour	0.280	194.0
High-range water-reducer	0.057	39.5
Silica sand 0/1.2 mm	0.820	568.0
Silica sand 0/4.0 mm	0.940	651.1

Table 1. The mixture design.

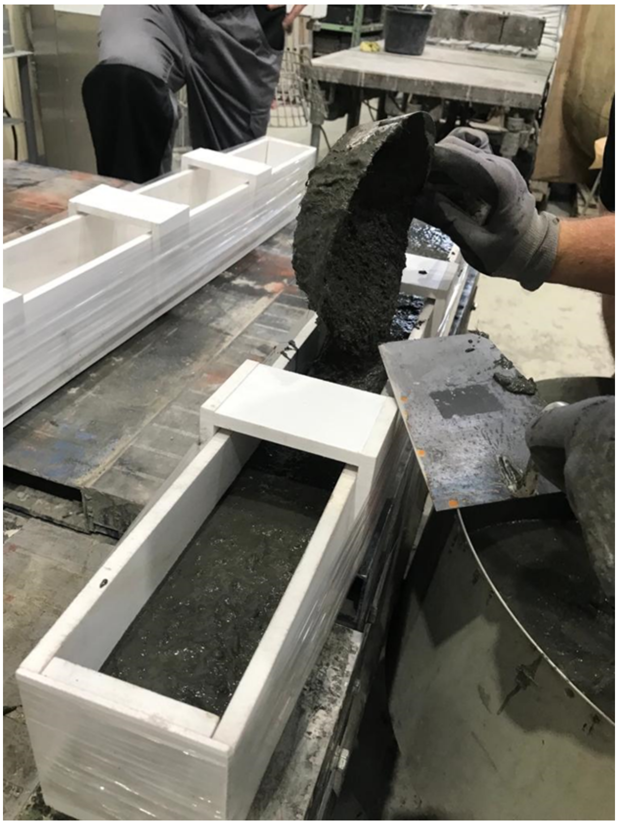

Figure 1. The filling of moulds.

Figure 2. Device.

The moulds had dimensions of 80 mm × 100 mm × 980 mm. These dimensions were chosen because of the typical dimensions of concrete lintels above doors. Plastic moulds were used instead of steel ones because the magnetic orientation process would otherwise be prevented by the steel enclosure. To ensure consistent results, one non-oriented and one oriented specimens were always made in sequence. The filled moulds were vibrated for 10 seconds.

The filled moulds intended for magnetic orientation were closed from the top and immediately subjected to the magnetic orientation process. It is important that relatively low manufacturing times are maintained as the fresh mixture needs to have suitable rheology so the magnetic field can overcome the matrix's resistance against the fibre rotation [11]. The fibres have been oriented with a special coil device using a magnetic field (Figure 2). It consists of a coil generating the required magnetic field and a plastic conveyor. The same device has been used in a previous study [12], which is describing it in more detail. The device is capable of treating specimens with cross-sections up to 100 mm × 100 mm and the parameters are as follows. The coil has 215 turns of copper tube with a diameter of 6 mm/4 mm (outer/inner diameter) with cooling water circulating inside the coil winding. In total, 5 compensating capacitors are connected in parallel to the coil, each of them has a capacity of 300 µF. The voltage is 300 V and is provided by a step-down autotransformer connected to a 400 V mains line. The current passing through the inductor is 150 A and generates a magnetic induction of 100 mT.

Steel fibres interact with magnetic field and align themselves in direction of magnetic field lines, in our case along the longitudinal axis of the specimen. The orientation of the fibres is ensured by passing the specimens through the device. Specimens were pulled through manually at a slow speed, approximately 2 cm/s (Figure 3). A total of 11 specimens were produced, 6 of which with oriented fibres and 5 specimens produced in the standard way with fibres randomly oriented. The specimens were produced in three batches. First to test the manufacturing setup and the technology (moulds, their transport and passing through the device) for one reference and one oriented specimen and the next two batches included 2 oriented, 2 non-oriented and 3 oriented, 2 non-oriented, respectively.

Figure 3. Pulling a filled mould through the device.

Figure 4. An example of Q measuring process.

2.2. Testing

Specimens were demoulded after 24 hours from mixing and measured non-destructively. The non-destructive method using a measuring coil with an inserted specimen is used for evaluating the fibre orientation. The parameter most sensitive to the quantity and orientation of the inserted fibres is the quality factor Q of the measuring coil, which is a dimensionless value calculated using the coil's resistance, inductance, and frequency of the passing electrical current. The quality factor Q and its use for this purpose is described more extensively in previous works [10, 13, 14]. The measurement setup consists of an impedance meter HIOKI IM3536 and a coil with 15 turns of a copper wire with a cross-section of 16 mm^2. The measuring coil has a diameter of 155 mm and a length of 105 mm (Figure 4). The measurement is time-independent and can be performed even with fresh concrete still inside the mould. The only material that affects the measurement is a magnetic material, which, in our case, are the steel fibres. If the fibres are aligned in the desired direction along the longitudinal axis of the specimen, i.e., parallel with the axis of the measuring coil, the fibres are interacting strongly with the measuring coil, leading to a low value of Q. Vice versa, specimens with randomly oriented fibres or perpendicularly to the axis of the measuring coil have a high value of Q. The measuring is performed on the frequency range from 1 MHz to 6 MHz, where Q shows the highest sensitivity for this particular setup. The peak Q value is used for a comparison between the specimens. The measurement is comparative and the absolute value is dependent not just on the orientation of the fibres but also on the size of the specimen (the volume of the fibres) and the measuring coil's parameters. Only specimens with the same percentage of fibre volume can be compared with each other [10]. All specimens were measured at 200 mm, 400 mm, 500 mm, 600 mm and 800 mm from one end.

Figure 5. Four-point bending test setup.

After the non-destructive measurement, the specimens were kept for 27 days in a dry room environment at 20 °C. After this time period, they were tested using a four-point bending experiment. The test was done using a hydraulic loading machine with a deformation control of 0.1 mm/min. The total span was 900 mm and the loading points were 300 mm apart in the centre of the span. Two displacement sensors on the sides of the beam measured the displacement which was then averaged. All specimens were tested until a complete specimen failure. The complete setup is shown in Figure 5. The broken halves were then subjected to compressive strength tests with a loading area of 80 mm × 100 mm.

3. Results

Figure 6 shows the measured quality factor Q of the first two manufactured specimens of the first batch (oriented – S, non-oriented – N, same designation for next graphs). The measuring was performed at different points along the specimen, which is indicated on the x-axis. A lower value of Q means more aligned fibres in the direction of the measuring coil's axis or lower fibre volume. This data shows that the oriented specimen have similar values of Q at all points. The difference between the largest and smallest values relative to the mean value for the individual measurements ranges from 3 % to 12 %, unlike the non-oriented specimen, where the Q values are highly

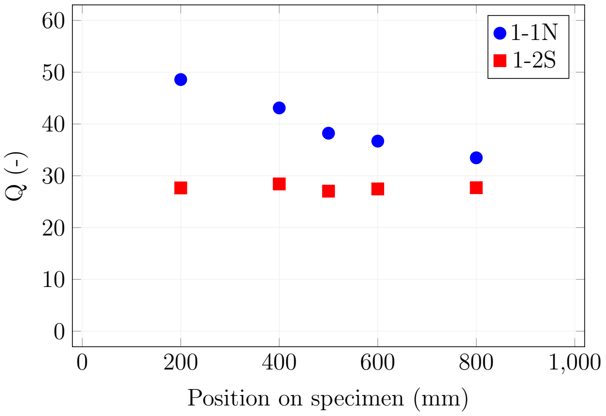

Figure 6. Q for the first batch of specimens.

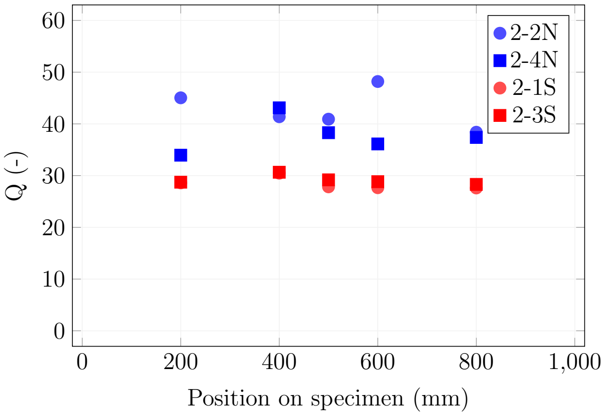

Figure 7. Q for the second batch of specimens.

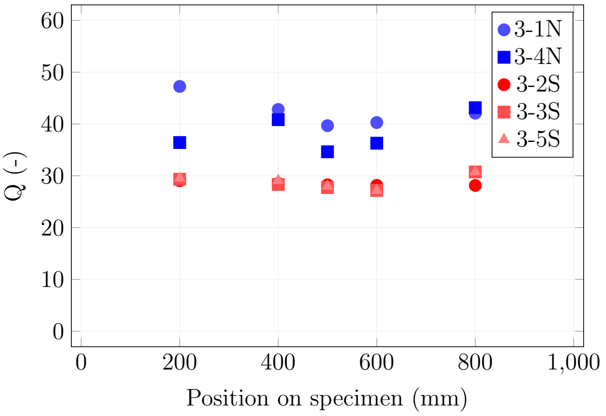

Figure 8. Q for the third batch of specimens.

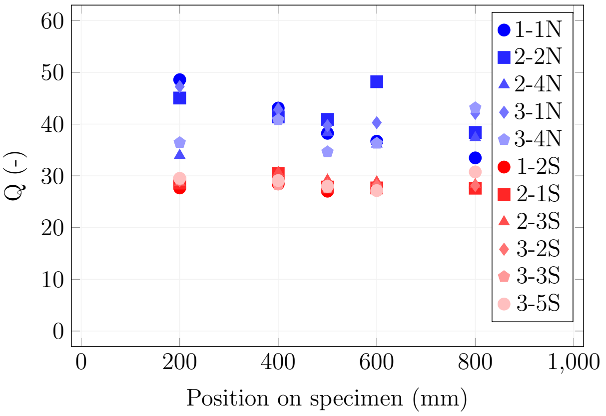

Figure 9. Summary of all Q measurements.

variable, from 18 % to 38 %. Since both specimens have the same fibre volume, the difference of Q is caused by the different orientation of fibres in the measured cross-sections. In each measured point of the oriented specimen, Q values are lower than at any point of the non-oriented specimen. This means that in each measured point, the oriented specimen has more aligned fibres in the preferred direction than the non-oriented specimen. The measurements of the first batch were carried out twice. The first measuring is identical to the second measuring which confirms the functionality and reliability of the measuring method.

Figures 7 and 8 show the second and third batches, respectively. All results of the non-destructive measurement are summarised in Figure 9. The overall average value of Q for specimens exposed to a magnetic field is 29.15. Meanwhile, reference specimens have an average Q of 38.35, which is 23 % higher than the oriented specimens. All of the oriented specimens also have lower spreads of Q.

All of the measured results are summarised in Table 2. The load-displacement diagrams obtained from the bending experiments are shown in Figure 10. From the graph and from the flexural strength values, it is clear, that the specimens treated with the magnetic field performed significantly better. For the subsequent comparison of the mechanical parameters, the outlying values were excluded (specimens 2-4N and 3-2S). The average flexural strength of oriented specimens is 15.93 MPa and 7.20 MPa for non-oriented specimens, which is an increase of 121 %. We can also compare the dissipated mechanical energy, which is calculated as the area under the load-displacement curve. In this case, the average values rose by 178 % for oriented specimens. However, we can observe, from Figure 10 that the peak loads were achieved for larger displacements for the oriented specimens, i.e., the orientation improved the deflection hardening behaviour. The energy-absorbing capacity until the maximum peak is then much higher, although the force after it decays faster to similar values as for the non-oriented specimens, which is the result of the fibre length. Generally, the higher capacity to dissipate mechanical energy would be beneficial in the case of impact loading. The compressive strength has been affected minimally. The average compressive strength of oriented specimens is 128 MPa and 118 MPa for non-oriented specimens, which is a relative difference of 9 %.

In line with a previous study [10], the non-destructive measuring of Q correlates well with flexural strengths (Figure 11). The specimens with a higher flexural strength and higher dissipated energy have

Specimen	Flexural strength [MPa]	Quality factor [−]	Dissipated energy [J]	Compressive strength [MPa]
1-1N	7.55	38.22	79.05	120.19
1-2S	18.34	27.03	194.65	134.06
2-1S	13.91	27.83	100.09	126.19
2-2N	6.69	40.91	44.13	113.88
2-3S	13.95	29.18	103.96	116.56
2-4N	3.88	38.30	18.44	110.63
3-1N	6.87	39.68	39.20	125.25
3-2S	22.12	28.26	173.85	126.19
3-3S	17.17	34.64	115.05	131.50
3-4N	7.68	34.64	54.12	118.31
3-5S	16.29	27.98	97.63	132.63

Table 2. Summary of the results.

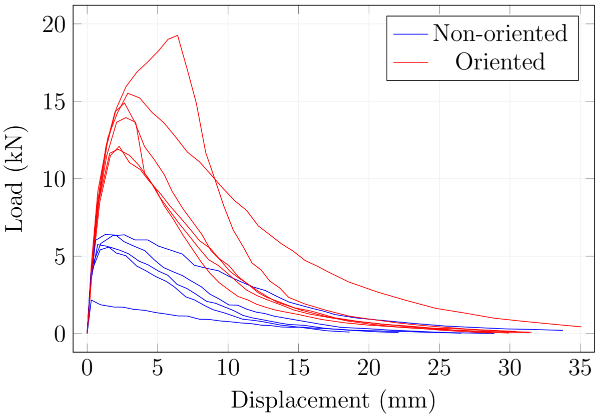

Figure 10. Load-displacement diagrams.

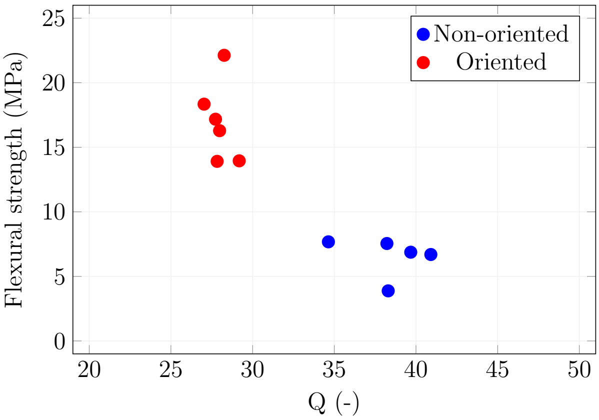

Figure 11. The quality factors Q compared to the measured flexural strengths for all specimens

a lower value of Q and vice versa. This is described in more detail in a previous study [10].

Figure 12 shows an example of three damaged specimens during the bending experiment together with the values of Q. As mentioned earlier, a higher Q means lower fibre volume of fewer preferentially-oriented fibres. At this stage, the non-destructive technique cannot differentiate between the two cases and it is a topic for future research. Nevertheless, both cases present a weak point for the element. It was expected that at these points, the failure would occur, but this assumption was generally not met. In these examples, only in the case of the specimen 2S, the failure initiated in the constant moment region, although at the point of lower Q. Other specimens developed the main crack at various locations with various Q values. It is worth noting, that the non-destructive measurement cannot predict the homogeneity of the matrix or, for example, the fibre anchoring strength or fibre interactions, which would be the key parameters determining the behaviour of the examined volume. Also, for the oriented specimens, as was seen in the previous graphs, the differences in Q are rather low.

Compared to a study with small-scale specimens [12], the mechanical parameters of the lintels showed a higher spread. It was assumed that, as the non-destructive measurement suggests, the magnetic orientation manufacturing also creates more homogeneous material and, therefore, lowers the spread of flexural strengths, dissipated energies, and other characteristics. From the graph in Figure 10, we can clearly see that this is not the case. This only highlights the necessity for experimental campaigns with larger-scale production, to provide a better picture regarding the scalability of all steps of new manufacturing techniques.

4. CONCLUSIONS

In this paper, the technology of magnetically oriented fibres has been tested on lintels with more realistic dimensions. Thanks to the exposure of the fresh concrete with steel fibres to a magnetic field inside

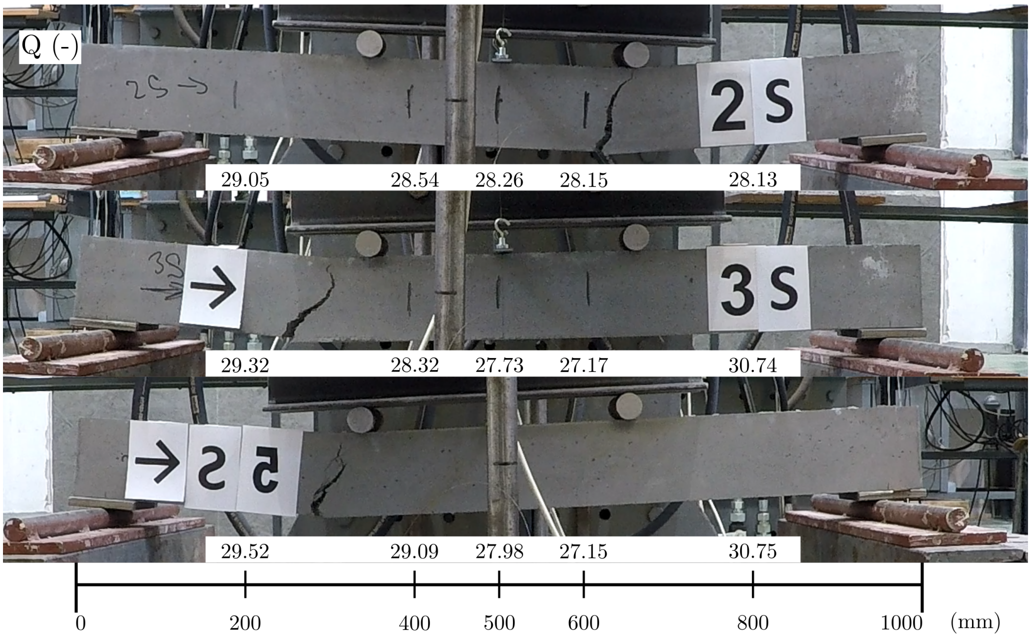

Figure 12. Cracking patterns compared with the non-destructive measurement results.

the orienting device, we can significantly improve the mechanical parameters in comparison to the reference specimens produced in a conventional way.

- Flexural strength is increased by 121 %.
- Dissipated energy is increased by 179 %.
- Compressive strength is increased by 9 %.
- The non-destructive measurements confirmed stable results along the specimen.
- The quality factor Q of oriented specimens is, on average, 24 % lower than for non-oriented specimens.

The results confirm the stability and repeatability of the technology to eventually replace the conventional steel bar reinforcement.

Acknowledgements

This research was funded by the Czech Science Foundation grant number GA20-00624S and by the Czech Technical University student's grant project number SGS22/050/OHK1/1T/11.

References

[1] H. Mikulčić, E. Von Berg, M. Vujanović, et al. Numerical modelling of calcination reaction mechanism for cement production. *Chemical Engineering Science* **69**(1):607–615, 2012. `https://doi.org/10.1016/j.ces.2011.11.024`.

[2] P. K. Mehta, D. Manmohan. Sustainable high-performance concrete structures. *Concrete international* **28**(7):37–42, 2006.

[3] I. L. Larsen, R. T. Thorstensen. The influence of steel fibres on compressive and tensile strength of ultra high performance concrete: A review. *Construction and Building Materials* **256**:119459, 2020. `https://doi.org/10.1016/j.conbuildmat.2020.119459`.

[4] V. P. Villar, N. F. Medina. Alignment of hooked-end fibres in matrices with similar rheological behaviour to cementitious composites through homogeneous magnetic fields. *Construction and Building Materials* **163**:256–266, 2018. `https://doi.org/10.1016/j.conbuildmat.2017.12.084`.

[5] M. Hajforoush, A. Kheyroddin, O. Rezaifar. Investigation of engineering properties of steel fiber reinforced concrete exposed to homogeneous magnetic field. *Construction and Building Materials* **252**:119064, 2020. `https://doi.org/10.1016/j.conbuildmat.2020.119064`.

[6] R. Mu, H. Li, L. Qing, et al. Aligning steel fibers in cement mortar using electro-magnetic field. *Construction and Building Materials* **131**:309–316, 2017. `https://doi.org/10.1016/j.conbuildmat.2016.11.081`.

[7] A. I. Miller, F. R. Bjorklund. Method of reinforcing concrete with fibres, 1977. US Patent 4,062,913.

[8] W. Xue, J. Chen, F. Xie, B. Feng. Orientation of steel fibers in magnetically driven concrete and mortar. *Materials* **11**(1):170, 2018. `https://doi.org/10.3390/ma11010170`.

[9] M. Wijffels, R. Wolfs, A. Suiker, T. Salet. Magnetic orientation of steel fibres in self-compacting concrete beams: Effect on failure behaviour. *Cement and Concrete Composites* **80**:342–355, 2017. `https://doi.org/10.1016/j.cemconcomp.2017.04.005`.

[10] K. Künzel, V. Papež, K. Carrera, et al. Electromagnetic properties of steel fibres for use in cementitious composites, fibre detection and non-destructive testing. *Materials* **14**(9):2131, 2021. `https://doi.org/10.3390/ma14092131`.

[11] K. Carrera, P. Kheml, R. Sovják, K. Künzel. Rheological properties of sonogel and comparison with rheological properties of high-performance concrete. *Materials Today: Proceedings* **58**:1308–1311, 2022. `https://doi.org/10.1016/j.matpr.2022.02.160`.

[12] K. Carrera, K. Künzel, P. Konrád, et al. Mechanical properties of high-performance concrete with steel fibres oriented by an electromagnetic field. *Journal of Materials in Civil Engineering* **34**(9):04022199, 2022. `https://doi.org/10.1061/(ASCE)MT.1943-5533.0004342`.

[13] K. Künzel, V. Papež, K. Carrera, R. Sovják. Magnetic properties of steel fibres commonly used in concrete. *Materials Today: Proceedings* **62**:2599–2603, 2022. `https://doi.org/10.1016/j.matpr.2022.04.134`.

[14] K. Carrera, R. Sovják, V. Papež, K. Künzel. Quality factor as a tool to measure concentration and orientation of ferromagnetic fibres in sample. *Materials Today: Proceedings* **62**:2624–2627, 2022. `https://doi.org/10.1016/j.matpr.2022.04.605`.

Acta Polytechnica **62**(5):538–548, 2022
`https://doi.org/10.14311/AP.2022.62.0538`

Published by the `Czech Technical University in Prague`

EXPERIMENTAL STUDY OF THE TORSIONAL EFFECT FOR YARN BREAK LOAD TEST OF POLYMERIC MULTIFILAMENTS

Daniel Magalhães da Cruz*, Fernanda Mazuco Clain,
Carlos Eduardo Marcos Guilherme

Federal University of Rio Grande, Engineering School, Stress Analysis Laboratory POLICAB, 96203-000, Rio Grande – RS, Brazil

* corresponding author: `dacruz.daniel@furg.br`

Abstract.

Polymeric multifilaments have gained a significant interest in recent decades. In the studies of mechanical characteristics, although there are different types of tests, such as rupture, abrasion, creep, impact and fatigue, it can be said that the main mechanical characterisation is the tensile rupture strength (Yarn Break Load, YBL), which also serves as a parameter for other tests. The objective of this work is to evaluate the results of breaking strength under different torsional conditions in polymeric multifilaments and to determine optimal twists for failures. The test were carried out with the following materials: polyamide, polyester, and high modulus polyethylene (HMPE), and for torsional conditions: 0, 20, 40, 60, 120, 240, and 480 turns per metre. As a result, for these torsion groups, curves were obtained for the three materials that present an optimal point of maximum rupture value, which was also experimentally proven. The twist that optimises the breaking strength of HMPE is 38 turns per metre, 56 turns per metre for polyester, and 95 turns per metre for polyamide. The twist groups that exceed the optimal torsion have a deleterious effect on the material, where the multifilament ceases to be homogeneous and starts to create an excessive "spring effect". The results found differ from the recommendation of the standard that regulates the YBL test, and thus, a relationship is built between groups of optimal torsion and linear density that provides evidence that the increase in linear density causes the optimal torsion for rupture to also increase, while the standard places a condition of 30 turns per metre for linear densities greater than 2200 dtex, and 60 turns per metre for linear densities less than 2200 dtex. In addition to optimal torsion values, this conclusion is paramount, the test procedure makes a general recommendation that does not optimise the breaking strength.

Keywords: Yarn Break Load, twist effect, maximum breaking strength, polymeric multifilaments.

1. Introduction

The last few decades have provided significant advances in the field of material engineering and its applications. There has been a significant increase in academic production and commercial focus on polymers [1]. It is noteworthy that over time, some of the polymers could be produced at low cost with very similar properties, and even superior to those of natural ones [2]. Thus, polymers have become, in certain applications, a viable and promising alternative to classic engineering materials.

In technical terms, polymers have several advantages as compared to other materials. Highlights are: low specific weight, high toughness (sometimes similar to metallic materials), good vibration dampening, low friction coefficient, thermal insulation, and high corrosion resistance. Their limitations are related to low stiffness, lower levels of hardness and resistance to abrasion, and heat sensitivity [3].

Synthetic polymers, when extruded, have a stretch orientation to provide textile yarns [4]. Due to this elongation in fabrication, the ultimate tensile strength becomes greater, also having an effect of reducing the maximum elongation. The mechanism responsible for this improved performance is the orientation of the polymeric chains, with a possible formation of oriented crystals and a reduction of the amorphous phase [5].

One of the prominent uses of such polymeric materials is in offshore mooring systems, these synthetic fibre ropes have replaced traditional steel ropes due to their better properties in the marine environment and low weight [6]. There is a constant development of mooring ropes; since it is desired that they are more rigid to guarantee limits on the movement of floating units, their mechanical performance is fundamentally studied [7, 8].

On offshore moorings, the synthetic polymeric multifilaments for ropes can be made from different materials, but polyamide, polyester and high modulus polyethylene (HMPE) stand out. Polyamide can be highlighted by recent studies in mooring for Offshore Energy Conversion Systems, such as for FOWT floating wind turbines [9]. Polyester is a material already established in offshore mooring systems, it can be said that it is the most used in these applications, and studies that address it have excellent references in the literature [10]. High modulus polyethylene (HMPE), however, is a newer material, also more expensive, but it has excellent mechanical performance and there are studies for Mobile Offshore Drilling Unit [11, 12].

For mechanical characterisation of polymeric materials, the work carried out with multifilaments stands out, where the conditions of use involve multiple variables, such as temperature, humidity, and types of loads (static, sudden, cyclic). Predicting the behaviour of these materials is a challenge due to their non-linear characteristics [13]; this complexity means that much of the research is carried out experimentally [14].

From this mechanical characterisation carried out in several researches with polymeric multifilaments, the tensile rupture (Yarn Break Load, YBL) stands out as the main one. This is because YBL serves as a parameter for several other mechanical characterisation tests, such as impact, creep, abrasion, fatigue, quasi-static stiffness, and dynamic stiffness. As load, they usually use a specific percentage of the standard YBL breaking load, as seen in several works that attest YBL as a parameter for performing other mechanical characterisation tests on multifilaments [15–19].

ISO 2062 standard regulates the execution of the Yarn Break Load test. In this standard, several parameters are determined, but no requirement is stated about the twist that must be applied to the multifilament. Only a torsional recommendation exists in the standard norm based on the dTex (linear density). Due to this standard, most of the papers that show the YBL in the experimental data use either 60 twists per metre or no twists at all. To provide break values (YBL) that serve as a reference for each material, the results from the cited literature can be used, [15] for HMPE, [16] for polyamide, and [17] for polyester.

Furthemore, a study on torsional effect in aramid and LCP yarns can be mentioned [20]. The results show that yarn strength can be improved with a slight twist, but a high degree of twist damages the fibres and reduces the yarn's tensile strength. The approach defined in the study by Rao & Farris [20] is based on torsional angles and shows a general tendency that there is an ideal torsional angle group for each material to achieve a maximum strength.

Thus, the aim of this study is, through an experimental approach, to study the torsion effect on Yarn Break Load (YBL) tests, which are the main test used for mechanical characterisation of multifilaments: in particular analysing the effects on the values of breaking force. The hypothesis is that, as found in [20] for aramid multifilaments, there is a torsion group that optimises the breaking strength for polyamide, polyester, and HMPE.

2. Materials and methods

2.1. Multifilament materials and torsion conditions

In this study, the following materials are analysed: polyamide, polyester, and high modulus polyethylene. The materials tested were characterised by measuring their linear density and breaking load according to current standards, as shown in Sections 2.2 and 2.3.

Each material is initially tested with the following twist group: 00 (no torsion), 20, 40, 60, 120, 240 and 480 turns per metre.

Also, all tests followed standard atmosphere determinations of ISO 139:2005. The specimens are conditioned during the test with a temperature of $20 \pm 2\,°\mathrm{C}$ and a relative humidity of $65 \pm 4\,\%$ [21].

2.2. Linear density test, Tex

In the characterisation methodology of each of the multifilament materials, the weight by length is very important, even as a parameter to determine the linear tenacity of the multifilament. The density linear test (mass/length ratio) was performed for each material with a series of 10 specimens to obtain the mean and standard deviations according to ASTM D1577 [22].

The same procedure was performed for all materials: polyamide, polyester, and HMPE. For a sample with a length of $1000 \pm 1\,\mathrm{mm}$, the mass was measured on a highly accurate balance with a resolution of 0.0001 grams. For each sample, a 3-minute stabilisation period was set before recording the mass data indicated by the balance. Using the mass and length data, the linear density in grams per metre was determined. It should be highlighted that the unity usually appears in the literature in tex [g/km], and can also be presented in submultiple notation as decitex [dtex].

2.3. Yarn Breaking Load test

The multifilament break test follows the methodology of the ISO 2062:2009 standard and is called Yarn Break Load (YBL) [23]. The main parameters of the test being: tested useful length – 500 millimetres, speed – 250 millimetres per minute, and environmental standard ISO 139:2005. The Yarn Break Load test gives the breaking value as well as the maximum elongation of the tested specimen. This result is also important to determine the linear tenacity of the multifilament. Breakage tests were performed on 12 specimens for each of the 7 torsion groups and for each of the 3 materials, resulting in 252 specimens. Data were statistically filtered using Box-plots, leaving 8 values for each group that characterise the mean of the required condition and make up the standard deviation. In the box-plot tool, values that differ greatly from the set are outside an accepted range. These atypical and extreme values are known as outliers and are excluded from the treatment [23].

2.4. Curve parameterization for optimal point

In the work of Rao & Farris [20], an optimal point of twist angle is presented. The expectation that something similar will occur in relation to the torsion groups in turns per metre is what motivates the parameterisation of the curve to an optimal point. Theoretically, increasing the twister condition increases the breaking strength to an optimal point, and increasing the twist any further decreases the breaking strength.

With the rupture results for each of the torsional groups, graphs of the torsional groups versus YBL were plotted, where the axis x corresponds to the twist value and the axis y corresponds to the rupture strength. Then, the optimal point is determined by three sets of discrete data, for each of the groups tested: the highest breaking strength data are used, also taking into account the groups immediately before and immediately after. It should be noted that the non-linear characteristics of polymeric materials are what hinder a general approach to the results. Furthermore, it would be very difficult to predict a curve with a satisfactory coefficient of determination that passes through all 7 or 8 discrete points for each material.

With these 3 sets of data, it is possible to perform a quadratic regression and determine a second degree polynomial that passes through the 3 points. In fact, this determination is a precise mathematical methodology that makes a perfect fit. Since R^2 represents a quantitative measure to predict whether a given mathematical model is satisfactory for the described behaviour, in this case, it forces a perfect fit, an R^2 equal to 1 [24]. By definition, the maximum and minimum points of a given function are equivalent to a first derivative of the function equal to zero, and this will be able to provide the ideal torsional groups for maximum breaking strength for each of the materials [25]. After finding the ideal twist point, all materials were tested again for this ideal twist condition to verify the experimental YBL value with the one obtained mathematically.

2.5. Relationship between optimum twist and linear density

The recommendation of the standard that regulates the Yarn Break Load test, ISO 2062:2009 is: “A twist of 60 ± 1 turns/m for yarns below 2200 dtex and a twist of 30 ± 1 turns/m for yarns above 2200 dtex are recommended. Other twist amounts may be allowed on agreement of the interested parties” [26].

It is not a requirement of the standard, but based on that recommendation, it is possible to infer that the optimal torsion group is a function of the linear density (Tex) of the material. Based on this and taking into account the optimal experimental results, perhaps it is possible to make a mathematical model for torsion per metre as a function of the linear density value in Tex [g/km]. The methodology used is the least-square method associated with the concept of the best coefficient of determination, that is, $R^2 = 1$ [24, 27]. It should be emphasized that this step depends on the experimental results and on the aforementioned methodology itself.

3. Results and discussions

3.1. Linear density for multifilaments

The results of linear density measurements are shown in Table 1 for each material measurement series. It is observed that polyamide is the material with the highest linear density, while the high modulus polyethylene is the material with the lowest linear density; it should be noted that the difference linear density between these two materials is significant.

The standard deviation (SD) is very satisfactory. The results show the linear density values in tex [g/km] for each of the respective materials: 284.4 tex for polyamide, 225.5 tex for polyester, and 185.4 tex for high modulus polyethylene.

For a comparison, and even validation, results from the literature can be cited for each of the materials. In [16], the linear density for the polyamide was 284.6 tex. For polyester, in [17], the value of 233.8 tex can be found. And for the HMPE, in [15], a linear density of 176.4 tex was found.

	Polyamide	**Polyester**	**HMPE**
Average	0.2844	0.2255	0.1854
SD	0.0011	0.0006	0.0009

Table 1. Linear density results in grams per metre [g/m].

3.2. Yarn Breaking Load for torsion groups

For the Yarn Break Load criterion, the breaking force is used for each of the twist groups. Table 2 shows the mean and SD for YBL of the 8 sets of filtered data, as described in Section 2.3, for each group of torsion.

Although there is no data in the literature for all torsional conditions, the results presented in Table 2 can be compared to specific literature cited in the introduction [15–17]. In the reference works, a breaking force for HMPE of 500.84 Newtons with a standard deviation of 16.37 Newtons was measured [15], but the torsion used was not specified, although the need for adherence to the standard suggests that it was 60 turns per metre. For polyamide, the average breaking strength found for an untwisted condition was 210.47 N with a standard deviation of 3.78 N [16]. A value reference for YBL polyester can be an average breaking force of 174.04 N with a standard deviation of 3.20 N for a twist condition of 60 turns per metre [17]. As can be seen, they are numerically different but similar values in a very consistent way. These

Torsion [rev/m]	Polyamide		Polyester		HMPE	
	Maximum Load [N]	**Strain [%]**	**Maximum Load [N]**	**Strain [%]**	**Maximum Load [N]**	**Strain [%]**
0	210.08 ± 3.90	17.68 ± 1.00	172.36 ± 2.48	12.52 ± 0.17	467.17 ± 10.74	2.53 ± 0.12
20	214.31 ± 2.50	17.19 ± 0.61	176.58 ± 4.23	13.15 ± 0.48	532.00 ± 8.15	2.81 ± 0.09
40	218.45 ± 0.72	19.81 ± 0.33	179.14 ± 1.17	13.50 ± 0.30	546.45 ± 5.47	2.96 ± 0.04
60	220.32 ± 1.82	19.68 ± 0.32	181.34 ± 2.18	13.29 ± 0.28	522.60 ± 7.85	2.85 ± 0.05
80	-	-	176.56 ± 1.12	12.91 ± 0.30	-	-
120	221.15 ± 1.61	21.17 ± 0.69	175.62 ± 2.29	13.24 ± 0.44	474.16 ± 21.67	2.96 ± 0.17
180	210.40 ± 2.49	21.49 ± 0.57	-	-	-	-
240	190.87 ± 4.72	20.39 ± 1.11	151.66 ± 4.53	13.76 ± 0.38	193.93 ± 21.13	3.24 ± 0.25
480	95.39 ± 2.85	28.03 ± 2.70	67.03 ± 3.08	16.15 ± 1.71	94.25 ± 13.44	7.78 ± 1.05

Table 2. Yarn Break Load results for polyamide, polyester and HMPE

sensitive differences can even be justified by the coil manufacturer or polymerisation method. Thus, the values presented in Table 2 are values verified in the literature in coherent ranges for each material (mainly for untwisted groups and with 60 turns per metre).

Of the initial 7 torsion groups, the 80-turns-per-metre group for polyester and the 180-turns-per-metre group for polyamide were added, as can be seen in Table 2. The reason for these additions is due to the higher tensile strength in the group immediately preceding the aggregate, the intention was to verify the behaviour of the breaking force for some marginally intermediate group that would allow interpretations, since in relation to the initial values the torsion gaps were large. There is also the intention of verifying an increasing and then decreasing behaviour, because the absence of a hold level confirms a result similar to that of [20], that is, there is a maximum point that optimises resistance, quoted for torsional angle in the literature and for a torsional ratio in turns per metre in the present work.

The results can be graphically represented for each material, Figure 1 for polyamide, Figure 2 for polyester and Figure 3 for HMPE.

There is a torsional group that provides the highest break value in the yarn break load test, which differs for each material. For polyamide, the maximum break value is 221.15 Newtons for a twist of 120 turns per metre, polyester breaks at 181.34 Newtons for a twist of 60 turns per metre, and for HMPE, the maximum break is 546.45 Newtons for a twist of 40 turns per metre.

In the table and graphs, there is important information about stretching. An increasing trend towards elongation is observed. At certain points, the mean even decreases, but if the standard deviation is considered, it can be said that there is an increase in elongation as more twist is added to the specimen.

The addition of torsion promotes a densification of the multifilament, the effect of this torsion is manifested in the elongation in what can be called the "spring effect". As the "spring effect" increases, the elongation increases in a contained manner, until reaching the point in which the multifilament starts to fold in on itself. In approximately 200 or 240 turns per metre, when this "self-folding" of the multifilament occurs (indications in red circles in Figure 4b), the elongation data grows exponentially for the YBL test. Understanding that this more expressive increase in elongation is not a characteristic of the material, but is the removal of excessive "self-folding" torsion through traction.

In the rupture graph, this removal of "self-folding" is evident by the abrupt decays that occur during the test, taking away the visual homogeneity of the graph, Figure 5.

These groups of excessive elongations also appear to be the groups with the lowest breaking strength. What happens is that the excessive twist promotes shear forces, so a much larger amount of twist promotes more shear forces in the multiflament when it is pulled, and therefore the break value is lower.

It is noteworthy that the effect of any torsion group has an important characteristic from the point of view of homogenising the moment of rupture, even due to the effect of densifying the multifilament. For all materials in this study, this homogeneity in rupture can be observed for a group that has the torsion. Taking polyamide as an example, in Figure 6 and Figure 7, the untwisted and 20-turns-per-metre graphs are displayed respectively.

In Figure 6, this rupture is seen unevenly, and in Figure 7, where there is a torsion in the specimen, the rupture is much more homogeneous.

3.3. Determination of the optimal torsion group

From the results already shown, it is found that there is an optimal group for each material. As described in Section 2.4, for each material and its discrete data

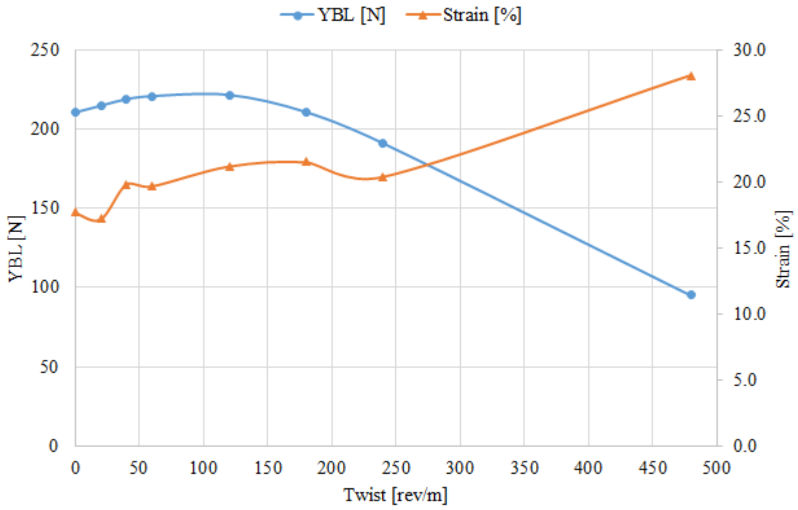

Figure 1. Twist x YBL for polyamide.

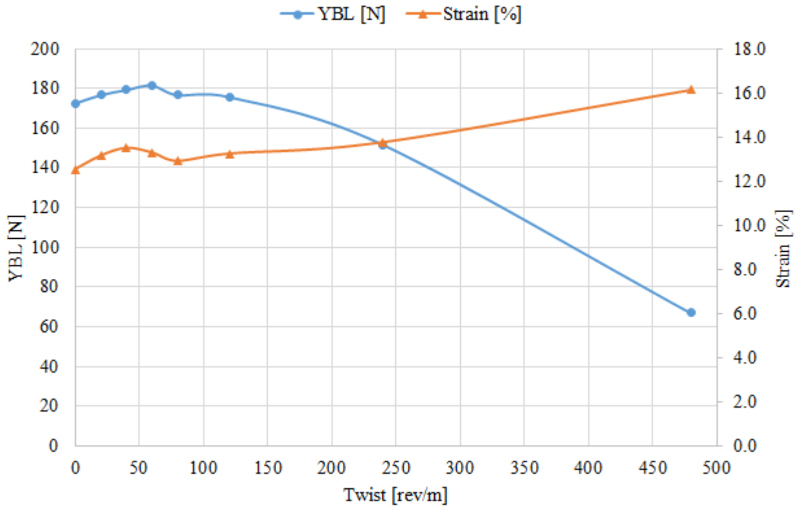

Figure 2. Twist x YBL for polyester.

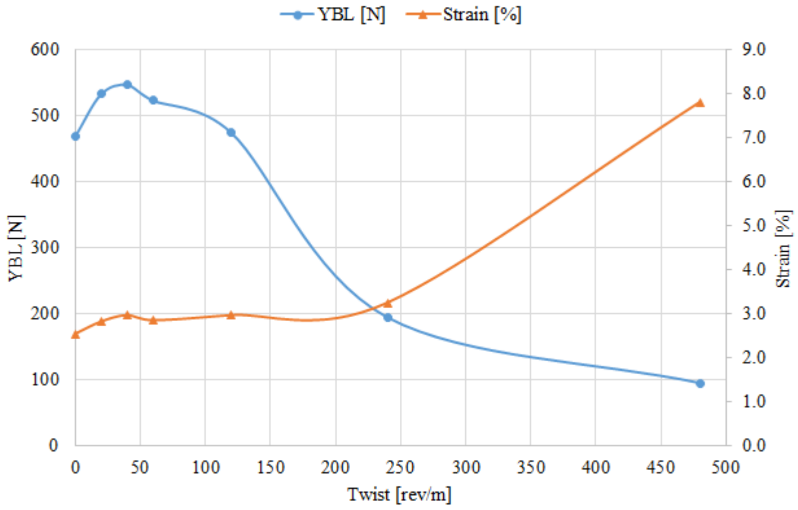

Figure 3. Twist x YBL for HMPE.

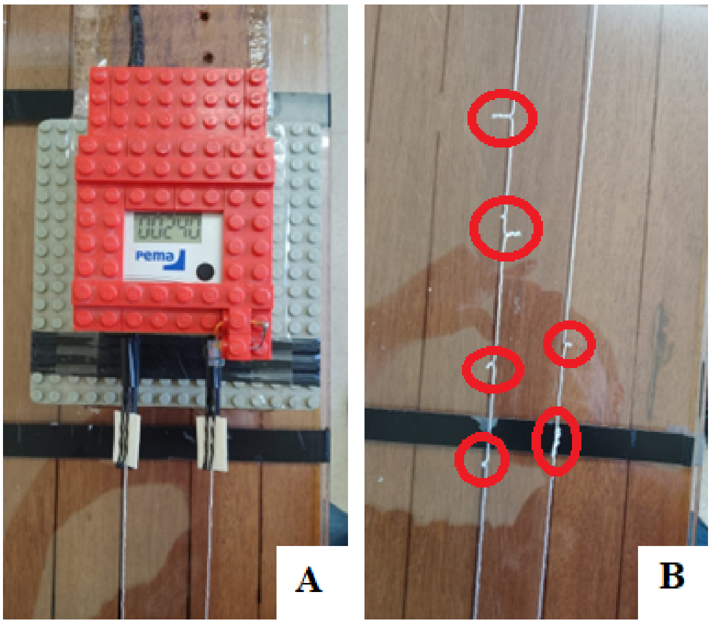

Figure 4. (A) Counter-turn display in 240 turns per metre, (B) Appearance of “self-folding”.

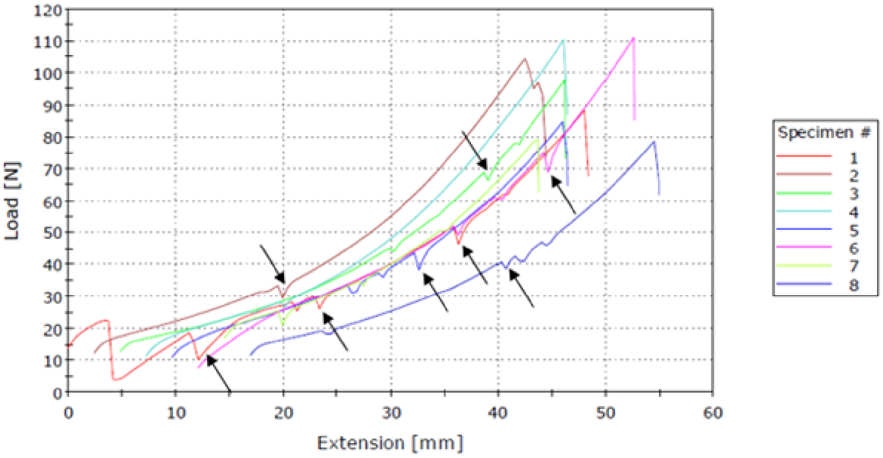

Figure 5. Graphic effect of self-folding removal on the HMPE specimen.

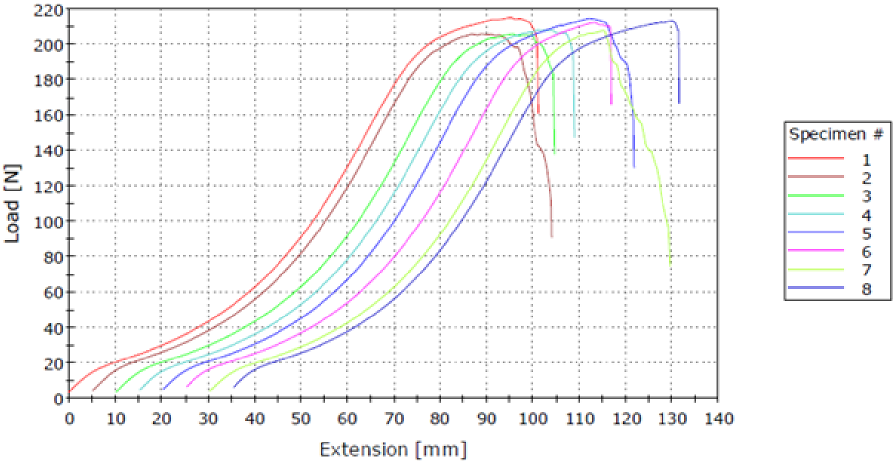

Figure 6. Graph of the YBL test results for polyamide, 00 turns per metre.

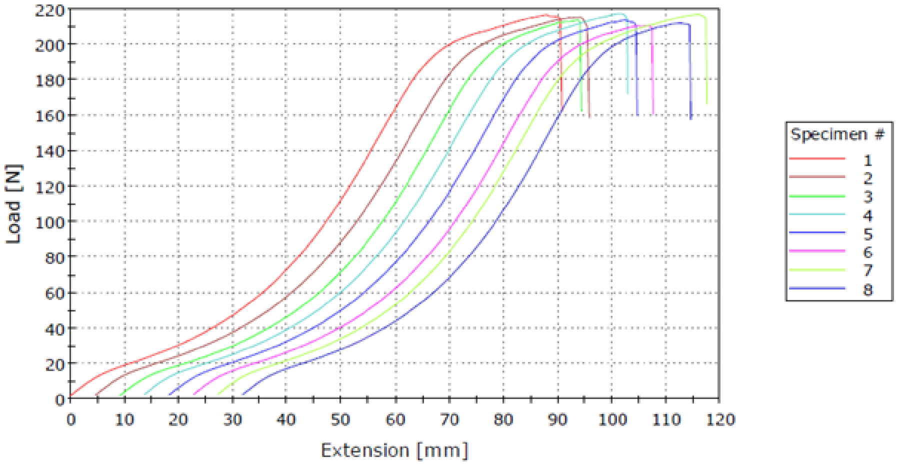

Figure 7. Graph of the YBL test results for polyamide, 20 turns per metre.

set, a system of equations was created. The matrix condition was solved by Gauss, thus providing the coefficients of the quadratic model of Equations (1), (2) and (3).

For polyamide, Equation (1):

$$y = -0.0016 \cdot x^2 + 0.3031 \cdot x + 207.92. \tag{1}$$

For polyester, Equation (2):

$$y = -0.0087 \cdot x^2 + 0.9819 \cdot x + 153.82. \tag{2}$$

For HMPE, Equation (3):

$$y = -0.0479 \cdot x^2 + 3.5945 \cdot x + 479.26. \tag{3}$$

The approximated curves, developed by the quadratic model, are shown in Figure 8 (polyamide), Figure 9 (polyester) and Figure 10 (HMPE).

The first derivative of a function equal to zero represents the maximum and/or minimum points of the function [25], as in all models, there is a downwards concavity of the parabola, it is the maximum of the function which, when equal to zero, will result in the optimal torsion group for the maximum breaking value.

For polyamide, Equation (4):

$$\frac{\mathrm{d}}{\mathrm{d}x}\Big[-0.0016 \cdot x^2 + 0.3031 \cdot x + 207.92\Big] = 0. \tag{4}$$

For polyester, Equation (5):

$$\frac{\mathrm{d}}{\mathrm{d}x}\Big[-0.0087 \cdot x^2 + 0.9819 \cdot x + 153.82\Big] = 0. \tag{5}$$

For HMPE, Equation (6):

$$\frac{\mathrm{d}}{\mathrm{d}x}\Big[-0.0479 \cdot x^2 + 3.5945 \cdot x + 479.26\Big] = 0. \tag{6}$$

Thus, the optimal torsional groups, rounded to whole numbers, are: 95 turns per metre for polyamide, 56 turns per metre for polyester, and 38 turns per metre for HMPE. With these torque values, it is possible to return to the respective models, Equations (1), (2) and (3) respectively, and determine the expected force value for the optimal point.

For polyamide, Equation (7) is developed:

$$y(95) = -0.0016 \cdot (95)^2 + 0.3031 \cdot (95) \\ + 207.92 = 222.2745\ [\mathrm{N}]. \tag{7}$$

For polyester, Equation (8) is developed:

$$y(56) = -0.0087 \cdot (56)^2 + 0.9819 \cdot (56) \\ + 153.82 = 181.5232\ [\mathrm{N}]. \tag{8}$$

For HMPE, Equation (9) is developed:

$$y(38) = -0.0479 \cdot (38)^2 + 3.5945 \cdot (38) \\ + 479.26 = 546.6834\ [\mathrm{N}]. \tag{9}$$

Observing the rupture forces obtained for optimal mathematical groups, the values are higher than those of the works taken as reference [15–17], and it is possible to infer the improvement in strength with a given twist per metre. It is important now to verify if the experimental breakage values are coincident for the same optimal groups obtained by the mathematical models above.

3.4. YBL results for optimal torsion

Having determined the appropriate ideal torsional groups, as well as the expected breaking force, it is possible to verify experimentally whether these torsions correspond to the maximum breaking response in the yarn breaking load test. The results of these tests are presented in Table 3, which contains the experimental results and the results of the predicted force in the quadratic mathematical model.

Very low relative differences in maximum breaking load occurred between the square model and the experimental data, which confirms that these are the ideal torsional groups for each material.

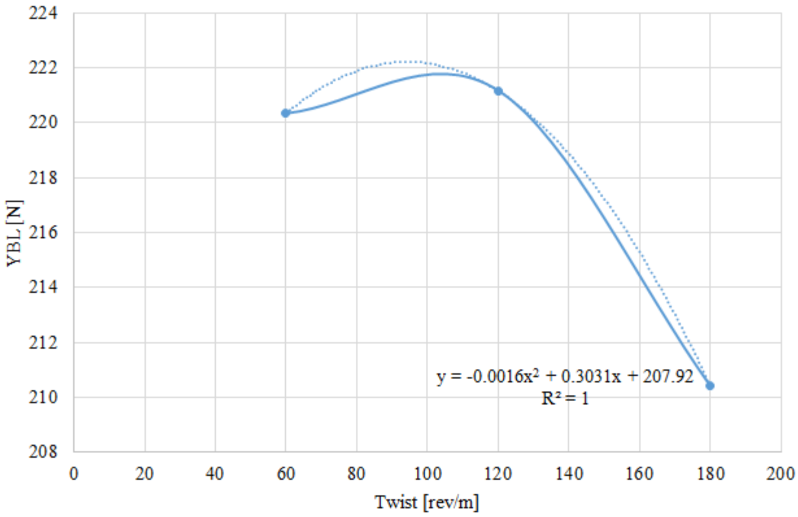

Figure 8. Square model for optimal stitch, polyamide.

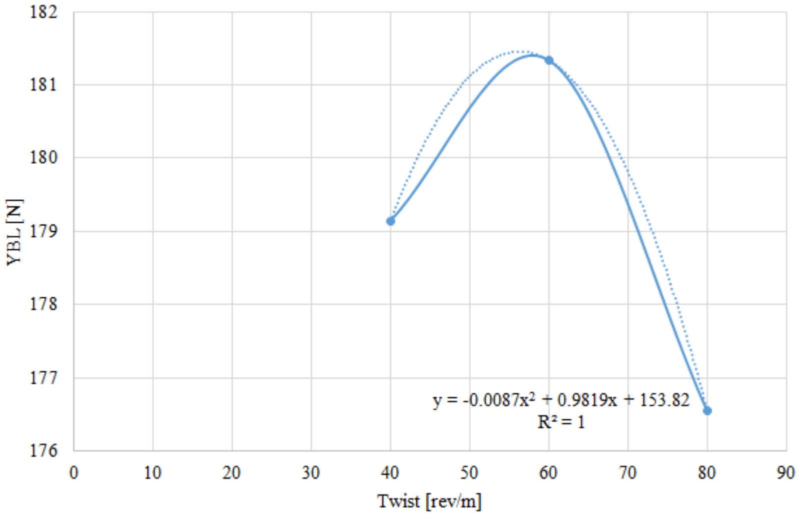

Figure 9. Square model for optimal stitch, polyester.

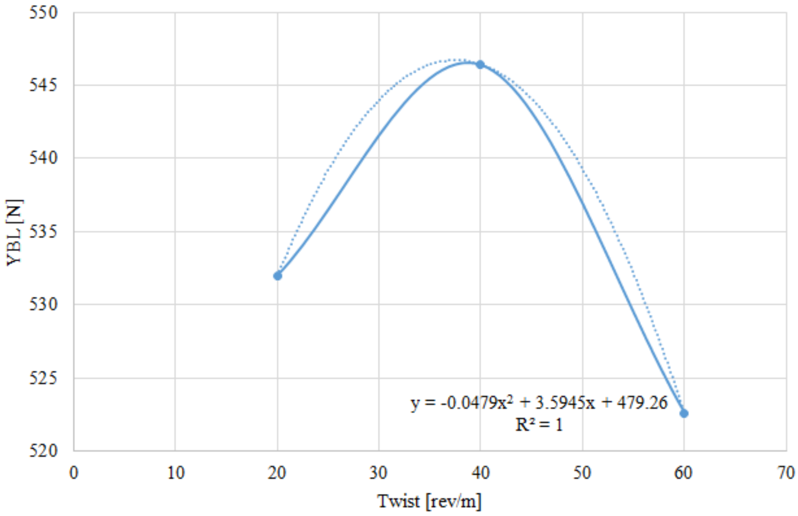

Figure 10. Square model for optimal stitch, HMPE.

	Square Model	**Experimental**	
	Maximum Load [N]	**Maximum Load [N]**	**Strain [%]**
Polyamide - 95 [rev/m]	222.2745	222.45 ± 1.23	20.60 ± 0.40
Polyester - 56 [rev/m]	181.5232	182.68 ± 2.11	13.24 ± 0.36
HMPE - 38 [rev/m]	546.6834	548.60 ± 15.95	2.87 ± 0.08

Table 3. Experimental results for the optimal torsion group of each material.

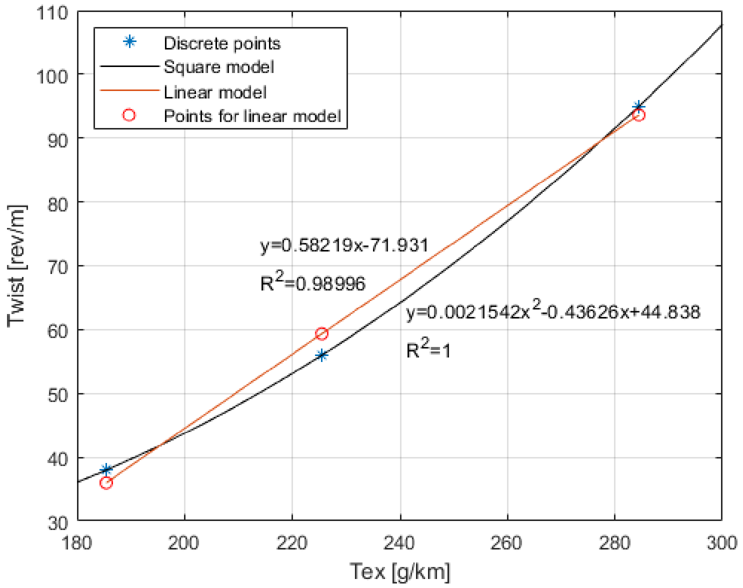

Figure 11. Mathematical model, optimal torsion as a function of linear density.

3.5. Curve ratio for optimal torsion and Tex

As described in Section 2.5, and considering that there are reasons for the optimal torsion to be related to the linear density, a mathematical model related these variables. There are, therefore, 3 discrete data sets, relating to polyamide (284.4 Tex; 95 rev/m), polyester (225.5 Tex; 56 rev/m) and HMPE (185.4 Tex; 38 rev/m). Thus, to force a perfect coefficient of determination ($R^2 = 1$), a square model of these discrete data sets is made. The mode system can be set up in its matrix form to determine the coefficients of the quadratic equation, and can be solved by the Gauss method, obtaining Equation (10).

$$\begin{aligned} y &= \frac{16790}{7794237} \cdot x^2 - \frac{3400351}{7794237} \cdot x + \frac{10590325}{236189}, \\ y &\cong 2.1542 \cdot 10^{-3} \cdot x^2 - 0.43626 \cdot x + 44.838. \end{aligned} \tag{10}$$

The coefficient that accompanies the square term is very small, which allows a linear model approximated by the method of least squares to be satisfactory. The programming was done in Octave, and the curves, equations and coefficients of determination indicated in Figure 11 were obtained.

The linear model is obtained using the least-square method [27] and returns the equation of the straight line shown in Equation (11).

$$y = 0.58219 \cdot x - 71.931 \tag{11}$$

As can be seen, the model allows to consider the interrelationship between the linear density and a certain optimal torsion. However, if the norm standard recommendation is observed, it states that a reduction in torsion leads to an increase in linear density, and in the constructed model, exactly the opposite is verified, that the increase in linear density causes the optimal torsion to also increase for the maximum break value. In other words, the standard recommendation can contribute to a lower performance of polymeric multifilaments, but it should always be emphasized that the standard norm recommendation is generalised, here, we are describing a model for specific synthetic polymeric materials.

4. Conclusions

In this study, it is evident that the amount of twists applied to the specimens influences the Yarn Break Load results. The gradual increase in twist densifies the multifilament, making its breakage more homogeneous. A consequence of this densification is also an increase in the breaking load up to a certain optimal twist. In this study, optimal twists were determined for: polyamide (95 turns per metre), polyester

(56 turns per metre) and HMPE (38 turns per metre). After the optimal twist, the addition of torsion causes the shear forces to increase and consequently causes it to reach lower breaking values.

Another conclusion is related to the relationship between linear density and optimal torsion (Figure 11). The prescribed mathematical model proves to be very satisfactory both in the form of a quadratic model and a linear model. The model obtained in the study demonstrates that the increase in linear density causes the twist optimal value to increase up to the maximum breaking force, which is exactly the opposite of the recommendation of the standard ISO 2062 standard for yarn breaking load testing. That is, the standard makes a general recommendation that is comprehensive, and that does not optimise the performance of the material in terms of breaking strength.

In this study, the torsion effect for the YBL test was evaluated. Likewise, future studies can be carried out with the same purpose of evaluating the torsion effect in other multifilament mechanical tests, such as creep, fatigue, and abrasion.

Acknowledgements

The authors would like to express their gratitude to the Federal University of Rio Grande and the POLICAB Stress Analysis Laboratory for supporting this study.

References

[1] E. Hage Jr. Aspectos históricos sobre o desenvolvimento da ciência e da tecnologia de polímeros. *Polímeros* **8**(2):6–9, 1998. `https://doi.org/10.1590/S0104-14281998000200003`.

[2] W. D. Callister Jr. *Ciência e engenharia de materiais*. Editora LTC, Rio de Janeiro, 7th edn., 2008.

[3] D. S. D. Rosa. *Correlação entre Envelhecimentos Acelerado e Natural do Polipropileno Isotático (PPi)*. Ph.D. thesis, Universidade Estadual de Campinas, 1996.

[4] H. A. Mckenna, J. W. S. Hearle, N. O'hear. *Handbook of fibre rope technology*. Elsevier, 2004.

[5] L. A. Santos. *Desenvolvimento de cimento de fosfato de cálculo reforçado por fibras para uso na área médico-odontológica*. Ph.D. thesis, Universidade Estadual de Campinas, 2002.

[6] H. da Costa Mattos, F. Chimisso. Modelling creep tests in HMPE fibres used in ultra-deep-sea mooring ropes. *International Journal of Solids and Structures* **48**(1):144–152, 2011. `https://doi.org/10.1016/j.ijsolstr.2010.09.015`.

[7] M. B. Bastos, L. F. Haach, D. T. Poitevin. Prospects of synthetic fibers for deepwater mooring. In *Rio Oil and Gas 2010*, IBP2745_10. 2010.

[8] S. Leite, P. E. Griffin, R. Helminem, R. D. S. Challenges and achievements in the manufacturing of DWM polyester tether ropes for the Chevron Tahiti projects – Gulf of Mexico. In *Rio Oil and Gas 2010*, IBP2291_10. 2010.

[9] Y. Chevillotte, Y. Marco, G. Bles, et al. Fatigue of improved polyamide mooring ropes for floating wind turbines. *Ocean Engineering* **199**:107011, 2020. `https://doi.org/10.1016/j.oceaneng.2020.107011`.

[10] C. J. M. Del Vecchio. *Light Weight Materials for deep Water Moorings*. Ph.D. thesis, University of Reading, UK, 1992.

[11] C. Berryman, R. Dupin, N. Gerrits. Laboratory study of used HMPE MODU mooring lines. In *Offshore Technology Conference*, OTC-14245-MS. 2002. `https://doi.org/10.4043/14245-MS`.

[12] I. Corbetta, F. Sloan. HMPE mooring line trial for scarabeo III. In *Offshore Technology Conference*, OTC-13272-MS. 2001. `https://doi.org/10.4043/13272-ms`.

[13] E. L. V. Louzada, C. E. M. Guilherme, F. T. Stumpf. Evaluation of the fatigue response of polyester yarns after the application of abrupt tension loads. *Acta Polytechnica CTU Proceedings* **7**:76–78, 2017. `https://doi.org/10.14311/APP.2017.7.0076`.

[14] V. Sry, Y. Mizutani, G. Endo, et al. Consecutive impact loading and preloading effect on stiffness of woven synthetic-fiber rope. *Journal of Textile Science and Technology* **3**:1–16, 2017. `https://doi.org/10.4236/jtst.2017.31001`.

[15] E. S. Belloni, F. M. Clain, C. E. M. Guilherme. Post-impact mechanical characterization of HMPE yarns. *Acta Polytechnica* **61**(3):406–414, 2021. `https://doi.org/10.14311/ap.2021.61.0406`.

[16] D. M. Cruz, E. S. Belloni, F. M. Clain, C. E. M. Guilherme. Analysis of impact cycles applied to dry polyamide multifilaments and immersed in water. *Rio Oil and Gas Expo and Conference* **20**(2020):199–200, 2020. `https://doi.org/10.48072/2525-7579.rog.2020.199`.

[17] I. Melito, E. S. Belloni, M. B. Bastos, et al. Effects of mechanical degradation on the stiffness of polyester yarns. *Rio Oil and Gas Expo and Conference* **20**(2020):176–177, 2020. `https://doi.org/10.48072/2525-7579.rog.2020.176`.

[18] L. Cofferri, C. E. M. Guilherme, F. T. Stumpf. Application of the stepped isothermal method to evaluate creep behavior in high-modulus polyethylene yarns. In *27º Congresso Internacional de Transporte Aquaviário, Construção Naval e Offshore*. 2018. `https://doi.org/10.17648/sobena-2018-87587`.

[19] L. Caldeira, P. Lucas, F. Chimisso. Creep comparative behavior of HMPE (high modulus polyethylene) multifilaments when submitted to changing conditions of temperature and load. In *Youth Symposium on Experimental Solid Mechanics*, pp. 99–102. 2010.

[20] Y. Rao, R. J. Farris. A modeling and experimental study of the influence of twist on the mechanical properties of high-performance fiber yarns. *Journal Of Applied Polymer Science* **77**(9):1938–1949, 2000. `https://doi.org/10.1002/1097-4628(20000829)77:9<1938::AID-APP9>3.0.CO;2-D`.

[21] International Organization for Standardization. Textiles – Standard atmospheres for conditioning and testing (ISO Standard No. 139), 2005.

[22] American Society for Testing and Materials. Standard test methods for linear density of textile fibers (ASTM Standard No. D1577), 2018.

[23] W. W. Hines, D. C. Montgomery, D. M. Goldsman, C. M. Borror. *Probabilidade e estatística na engenharia*. Editora LTC, Rio de Janeiro, 4th edn., 2006.

[24] P. A. Barbetta, M. M. Reis, A. C. Bornia. *Estatística: para cursos de engenharia e informática*. Atlas, São Paulo, 2010.

[25] P. A. Morettin, S. Hazzan, W. O. Bussab. *Cálculo – Funções de uma e várias variáveis*. Editora Saraiva, São Paulo, 3rd edn., 2012.

[26] International Organization for Standardization. Textiles – Yarns from packages – Determination of single-end breaking force and elongation at break using constant rate of extension (CRE) tester (ISO Standard No. 2062), 2009.

[27] O. Helene. *Método dos Mínimos Quadrados com Formalismo Matricial*. Livraria da Física, São Paulo, 2006.

Acta Polytechnica **62**(5):549–557, 2022
`https://doi.org/10.14311/AP.2022.62.0549`

DETERMINATION OF FAN DESIGN PARAMETERS FOR LIGHT-SPORT AIRCRAFT

Jan Klesa

Czech Technical University, Faculty of Mechanical Engineering, Department of Aerospace Engineering, Karlovo náměstí 13, Prague 2, Czech Republic

correspondence: `jan.klesa@fs.cvut.cz`

Abstract. This paper is focused on the preliminary design of an electric fan for light-sport aircraft. Usage of electric motors brings some advantages compared to piston engines, especially small size and the independence of power on shaft RPM. A 1D compressible fluid flow model is used for the determination of the performace. The influence of various system parameters is analysed. Results for the case of the UL-39 ultralight aircraft are presented. Finally, input parameters for the fan design are determined according to this analysis. This can be then used as input data for the standard fan (axial compressor) design procedure.

Keywords: Ducted fan, electric propulsion, axial compressor.

1. Introduction

Electric propulsion for aircrafts became a research topic in the last years, which is motivated by the huge progress in low-weight electric power systems. Electric flight was already developed in the 1960s for radio controlled model aircraft, e.g., work of Fred Militky [1]. The progress in battery technology (from NiCd to lithium-based batteries), electric motors (from simple DC brush motors with ferrite magnets, later neodymium magnets, and today brushless DC motors) and control electronics led to the increase of model performance and size.This led to the possibility of building manned electrical aircrafts in the last decade, e.g., projects of Airbus, Pipistrel, Extra, Jihlavan, etc.

Today, the technology is advanced enough to build a small fully-electric aircraft. The electric propulsion brings some advantages, especially possible drag reduction due to the lower volume and cross-section of electric motors in comparison with turboprop and piston engines. This allows to decrease the nacelle size (for multiple engine aircraft) and better fuselage nose shape (for single engine aircraft). However, cooling the electric components requires relatively large cooling systems because of the low temperature difference. The main disadvantage remains the source of the electric energy. Batteries are relatively heavy and have a low energy density as compared with aircraft fuel [1]. Another problem is the long time necessary for recharging the batteries between flights. Refuelling is usually much faster and does not require a high power electric line connection at the airport. Thus, some hybrid system using standard aircraft fuel (e.g., Jet-A1) or hydrogen is necessary for a long range/high endurance aircraft. In this case, electricity is made onboard by means of an electric generator powered by turboshaft engine or APU. In this case, energy can be stored in the high energy density medium, but the overall efficiency is lower due to the chain of necessary energy transformations. Both systems are under development for use in aviation, e.g., Honeywell [2] or Rolls-Royce [3].

A ducted fan is used on electric-powered "jet" aircraft, e.g., Airbus E-Fan. A ducted fan allows the transformation of the electric energy to the propulsive thrust at high flight velocity, where a propeller is inefficient. It became a dynamic research area in the last years due to the efforts of building electric or hybrid-electric transport aircrafts.

However, ducted fans or ducted propellers have a lower performance at low flight speeds for multiple reasons:

- Higher outlet velocity which causes lower propulsive efficiency.
- Higher losses in the propulsion system due to the friction at duct walls.
- Higher fuselage (nacelle) drag.
- Higher drag when flying with the engine off-regime.

But there is also some motivation for fan-powered low-speed aircraft, which can have various advantages:

- Safety, because rotating parts are covered by the duct, and so the risk of damage or injures can be lower than for a conventional propeller.
- Possible noise reduction.
- “Jet-feeling” - fan-powered aircraft can be used for low-cost training of jet pilots.

The preliminary design and a comparison of a ducted fan with a propeller was presented in [4]. This paper is based on the experience with the long developement of the UL-39 aircraft at the Department of Aerospace Engineering of the Czech Technical University in Prague. A more general approach with a compressible fluid flow model is used, which means

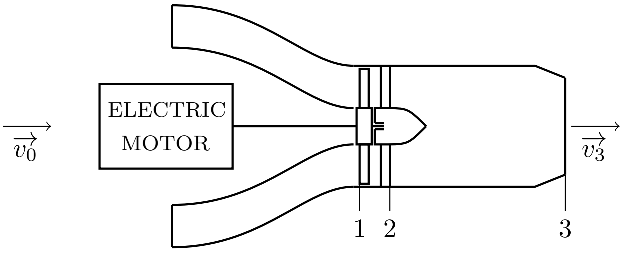

Figure 1. Propulsion system scheme.

Free atmosphere	0
Plane in front of the fan	1
Plane behind the fan	2
Nozzle exit	3

Table 1. Section definitions.

that this approach can also be used for a much faster aircraft than the UL-39.

The aircraft and also its propulsion system must fullfill legal requirements. For Czech ultalight aircraft, it is certification specification UL-2 [5] (requirements of the German certification specification LTF-UL are very similar [6]). This brings the requirement that the aircraft has to take-off on a given distance, this creates requirement for thrust at low speeds so that the acceleration is adequate.

2. Methods

The simulation model is based on a modified approach from [4] based on experience from the developement and testing of the UL-39 aircraft. A compressible fluid model is used so that this method can be used for a faster aircraft than the ultralight cathegory. An approach to the fan design based on the comparison of various configurations for the complete flight velocity envelope is used due to certification specification requirements, which are contradictory to the requirement of high cruise speed as shown later in this paper, and led to the necessary modification of the approach presented in [4]. An iterative method in MATLAB is used for the solution of the system of equations. The result of the method is the fan design point which can then be used for the fan design by standard procedures, see e.g. [7] and [8].

2.1. Physical model

The aim of the first step is to find parameters of the propulsion system in design conditions, which were determined according to the experience with the UL-39 aircraft testing and operation [9]. It is a 1D compressible fluid flow model. Input parameters used for the fan design phase can be found in Table 2. The fan has to be placed into the available space in the fuselage, which limits the maximal fan diameter and determines the length of the exhaust duct. Figure 1 and Table 1 explain the numbering of different planes in the propulsion system.

Due to the complexity of the equations, a numerical iterative approach is used for the solution. Input parameters are the fan diameter D_1 and nozzle cross-section ratio A_1/A_3. The thrust curve, i.e. dependence of the thrust T on the flight velocity v_0, is then determined for every combination of D_1 and A_1/A_3. The fan hub-to-tip radius ratio is set to 0.5, i.e. the blade length is half of the fan radius. Then the fan cross-section A_1 can be determined according to

$$A_1 = \frac{3}{4}\frac{\pi D_1^2}{4}. \tag{1}$$

Engine power P	200 kW
Flight velocity range v_0	0–100 m s^{-1}
Air density ρ	1.225 kg m^{3}
Atmospheric pressure p_{s0}	101 325 Pa
Intake duct pressure loss coefficient ζ_{01}	0.1
Fan efficiency η_{fan}	0.85
Outlet duct wall friction factor λ_{23}	0.013
Outlet duct length L	1.5 m
Air ratio of specific heats κ	1.4
Air specific gas constant r	287 J kg^{-1} K^{-1}
Air specific heat at constant pressure c_p	1004.5 J kg^{-1} K^{-1}

Table 2. Input parameters for the propulsion system.

The total pressure in the free atmosphere in front of the aircraft is detemined by the standard formula from flight Mach number M_0 by

$$p_{t0} = p_{s0}(1 + \frac{\kappa - 1}{2}M_0^2)^{\frac{\kappa}{\kappa-1}}, \tag{2}$$

where the flight Mach number M_0 is

$$M_0 = \frac{v_0}{a_0} \tag{3}$$

and the speed of sound in the atmosphere a_0 is

$$a_0 = \sqrt{\kappa r T_{s0}}. \tag{4}$$

The total temperature can be deremined in a similar way

$$T_{t0} = T_{s0}\left(1 + \frac{\kappa - 1}{2}M_0^2\right). \tag{5}$$

The total pressure in the intake duct is computed by means of a loss coefficient ζ_{01} and the fan axial velocity v_1

$$p_{t1} = p_{t0} - \frac{\zeta_{01}\rho_1 v_1^2}{2}, \tag{6}$$

where $\zeta_{01} = 0.1$ (based on CFD simulations from [10]). The total pressure recovery coefficient (see [11]) cannot be used in this case due to the low flight speed (data from literature sources are suitable for a faster aircraft). Heat exchange in the intake duct is neglected, thus the total temperature remains the same

$$T_{t1} = T_{t0}. \tag{7}$$

The static temperature in front of the fan is

$$T_{s1} = T_{t1} - \frac{v_1^2}{2c_p}, \tag{8}$$

the speed of sound is then

$$a_1 = \sqrt{\kappa r T_{s1}}, \tag{9}$$

and the Mach number

$$M_1 = \frac{v_1}{a_1}. \tag{10}$$

The static pressure can then be calculated from the Mach number

$$p_{s1} = p_{t1}\left(1 + \frac{\kappa - 1}{2} M_1^2\right)^{-\frac{\kappa}{\kappa-1}}. \tag{11}$$

The density and the air mass flow are then computed according to

$$\rho_1 = \frac{p_{s1}}{r T_{s1}}, \tag{12}$$

$$\dot{m}_1 = \rho_1 v_1 A_1. \tag{13}$$

It is assumed that the whole engine power P is used by the fan, i.e. the total temperature is increased in the following way

$$T_{t2} = T_{t1} + \frac{P}{c_p \rho_1 A_1 v_1}. \tag{14}$$

The total temperature for isentropic compression due to the fan is

$$T_{t2i} = T_{t1} + \frac{\eta_{Fan} P}{c_p \rho_1 A_1 v_1}. \tag{15}$$

Then, the total pressure becomes

$$p_{t2} = p_{t1}\left(\frac{T_{t2i}}{T_{t1}}\right)^{\frac{\kappa}{\kappa-1}}, \tag{16}$$

and the fan pressure ratio is

$$\Pi_{12} = \frac{p_{t2}}{p_{t1}}. \tag{17}$$

The stagnation density behind the fan is

$$\rho_{t2} = \frac{p_{t2}}{r T_{t2}}. \tag{18}$$

The critical air density (for choked flow state) behind the fan is

$$\rho_{c2} = \rho_{t2}\left(\frac{\kappa + 1}{2}\right)^{-\frac{1}{\kappa-1}}, \tag{19}$$

and the corresponding critical velocity is

$$v_{c2} = \sqrt{\frac{2(\kappa - 1) c_p T_{t2}}{\kappa + 1}}, \tag{20}$$

and then, the critical flow density is

$$(\rho v)_{c2} = v_{c2} \rho_{c2}. \tag{21}$$

M_2 is computed so that the mass flow through the duct remains constant. i.e. $(\rho v)_1 = (\rho v)_2$. The speed of sound behind the fan is

$$a_2 = v_{c2}\sqrt{\frac{\kappa + 1}{2}\left(1 + \frac{\kappa - 1}{2} M_2^2\right)^{-1}}. \tag{22}$$

Then, the flow velocity is calculated from the Mach number M_2

$$v_2 = M_2 a_2, \tag{23}$$

and the air density becomes

$$\rho_2 = \rho_{t2}\left(1 + \frac{\kappa - 1}{2} M_2^2\right)^{-\frac{1}{\kappa-1}}. \tag{24}$$

The total pressure at the nozzle exit 3 is computed from the exhaust duct loss coefficient ζ_{23}

$$p_{t3} = p_{t2} - \zeta_{23}\frac{\rho_2 v_2^2}{2}. \tag{25}$$

The value of the loss coefficient ζ_{23} is determined according to the information from [12]. The flow density at the nozzle exit is computed from the condition of constant mass flow

$$(\rho v)_3 = \frac{(\rho v)_2}{\frac{A_3}{A_1}}. \tag{26}$$

The total temperature behind the fan remains constant

$$T_{t3} = T_{t2}. \tag{27}$$

The total air density at the nozzle exit is

$$\rho_{t3} = \frac{p_{t3}}{r T_{t3}}. \tag{28}$$

The critical (choked) air density in the nozzle exit is

$$\rho_{c3} = \rho_{t3}\left(\frac{\kappa + 1}{2}\right)^{-\frac{1}{\kappa-1}}, \tag{29}$$

and the corresponding critical air velocity is

$$v_{c3} = \sqrt{\frac{2(\kappa - 1) c_p T_{t3}}{\kappa + 1}}, \tag{30}$$

and the critical flow density is

$$(\rho v)_{c3} = \rho_{c3} v_{c3}. \tag{31}$$

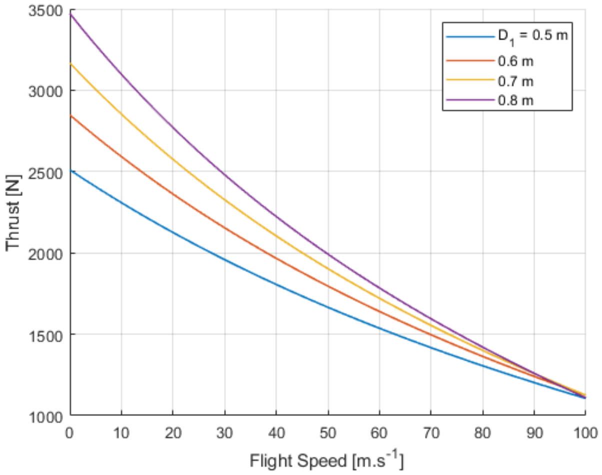

Figure 2. Thrust over flight speed for different fan diameters D_1, nozzle contraction ratio $A_1/A_3 = 1$.

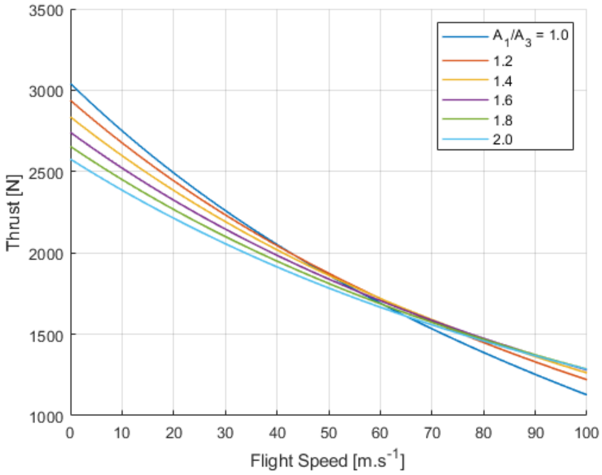

Figure 3. Thrust over flight speed for different nozzle contraction ratios A_1/A_3, fan diameter $D_1 = 0.66$ m.

The static temperature in the nozzle exit is

$$T_{s3} = T_{t3}\left(\frac{p_{s0}}{p_{t3}}\right)^{\frac{\kappa-1}{\kappa}}, \tag{32}$$

the corresponding speed of sound is

$$a_3 = \sqrt{\kappa r T_{s3}}, \tag{33}$$

and the flow velocity is

$$v_3 = M_3 a_3. \tag{34}$$

The nozzle exit Mach number M_3 is determined from the relation between static pressure p_{s3} and total pressure p_{t3}

$$p_{s3} = p_{t3}\left(1 + \frac{\kappa-1}{2}M_3^2\right)^{-\frac{\kappa}{\kappa-1}}. \tag{35}$$

The thrust of the propulsion system is determined from the momentum conservation law

$$T = \dot{m}\left(v_3 - v_0\right), \tag{36}$$

where the air mass flow is

$$\dot{m} = \rho_1 A_1 v_1. \tag{37}$$

Finally, the propulsion efficiency is defined by the standard formula

$$\eta = \frac{T v_0}{P}. \tag{38}$$

An iterative algorithm has to be used for the computation . A value $v_1 = 50\, m\, s^{-1}$ can be used as a guess for the first iteration.

Fan RPM is determined from the flow coefficient $\phi = v_{ax}/u$ which is assumed to be 0.5

$$n_m = \frac{120 v_1}{\pi D_1}. \tag{39}$$

3. Results

Thrust cuves (i.e. dependence of the thrust on the flight velocity) for different fan diameters D_1 and nozzle contraction ratios A_1/A_3 are presented in Figures 2 and 3. An increase in fan diameter D_1 (see Figure 2) causes a thrust increase for the given velocity range, however, this influence diminishes with increasing flight velocity as expected from the general theory of aerospace propulsion. The influence of nozzle contraction ratios A_1/A_3 on thrust (see Figure 3) is similar. Lower A_1/A_3 leads to a higher thrust at a lower flight velocity, but reduces the flight performance at a higher velocity. The influence of the fan diameter D_1 and nozzle contraction ratio A_1/A_3 on the efficiency is presented in Figures 4 and 5. The efficiency is relatively low in comparison with the standard propeller due to the small fan cross-section area and also due to the viscous losses in the duct system.

Another important parameter for the fan design is the axial velocity v_1 presented in Figures 6 and 7. It is clearly visible that there is a strong dependence of the fan axial velocity v_1 on constant electric motor power. Both parameters, i.e. fan diameter D_1 and nozzle contraction ratio A_1/A_3, have a strong influence on v_1. The dependence of the fan pressure ratio on the flight velocity and fan diameter is presented in Figure 8. The fan RPM for the same situation is presented in Figure 9 (the assumption of constant $\phi = v_{ax}/u = 0.5$ is used).

Based on the above-mentioned results, the dependencies of fan pressure ratio Π, thrust T, fan axial velocity v_1 and fan RPM n_m on the fan diameter D and nozzle contraction ratio A_1/A_3 for static case (i.e. $v_0 = 0\,\mathrm{km\,h^{-1}}$, take-off) and for maximum flight velocity (i.e. $v_0 = 300\,\mathrm{km\,h^{-1}}$), are presented in Figures 10–17. Based on this and the fuselage geometry, a fan diameter of $D_1 = 0.66$ m was selected. The ratio A_1/A_3 is determined from the relative thrust shown in Figure 18. The relative thrust is defined as the ratio T/T_{ref}, where the reference value T_{ref} is

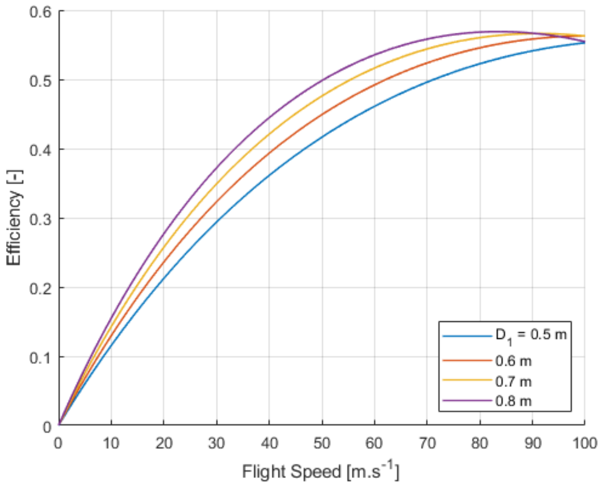

Figure 4. Efficiency of the propulsion system for different fan diameters D_1, nozzle contraction ratio $A_1/A_3 = 1$.

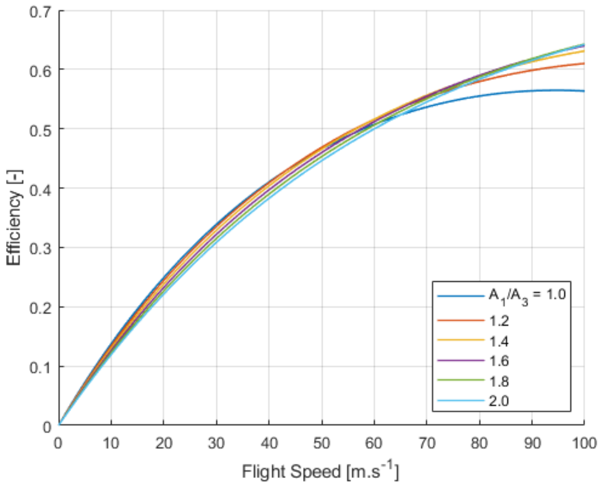

Figure 5. Efficiency of the propulsion system for different nozzle contraction A_1/A_3, fan diameter $D_1 = 0.66$ m.

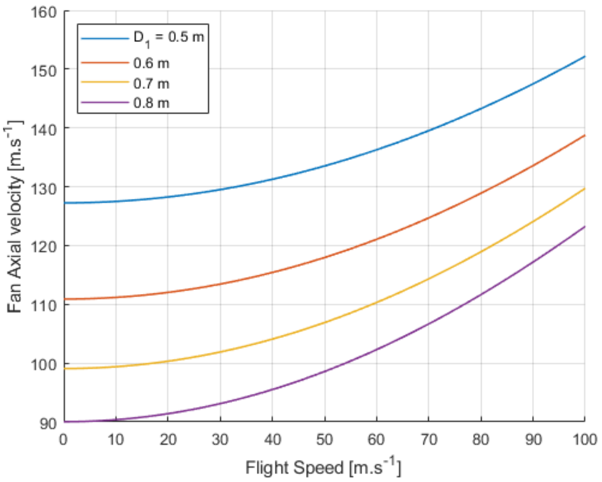

Figure 6. Fan axial velocity component over flight speed for different fan diamenters and $A_1/A_3 = 1$.

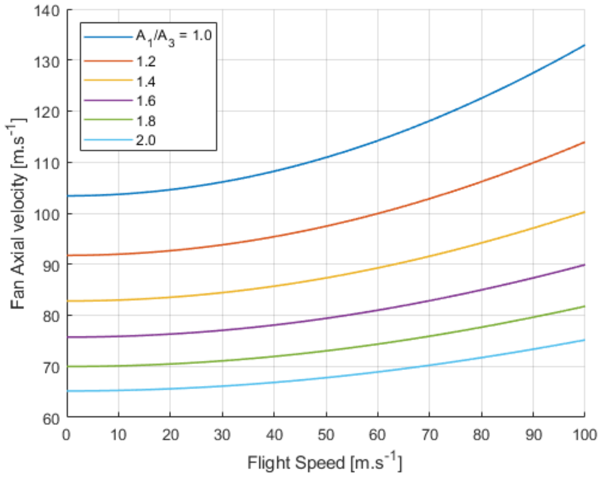

Figure 7. Fan axial velocity component over flight speed for different nozzle contraction ratios A_1/A_3, fan diameter $D_1 = 0.66$ m.

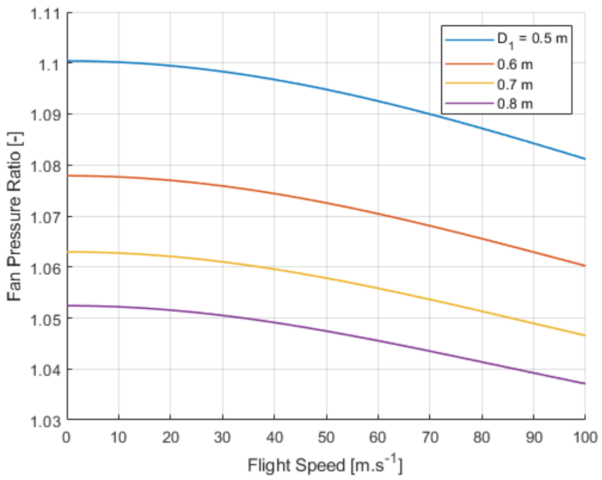

Figure 8. Fan pressure ratio over flight speed for different fan diamenters and $A_1/A_3 = 1$.

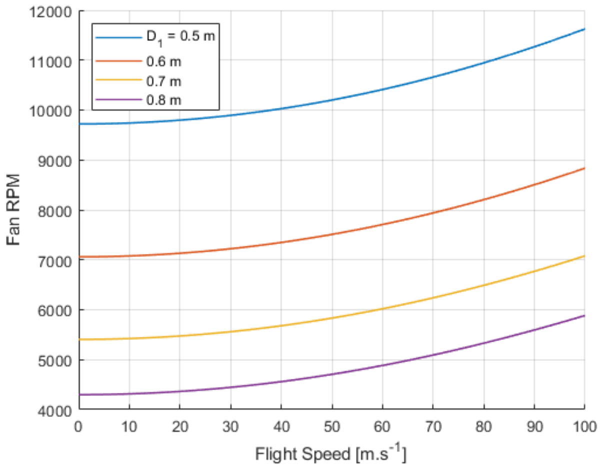

Figure 9. Fan RPM over flight speed for different fan diamenters and $A_1/A_3 = 1$.

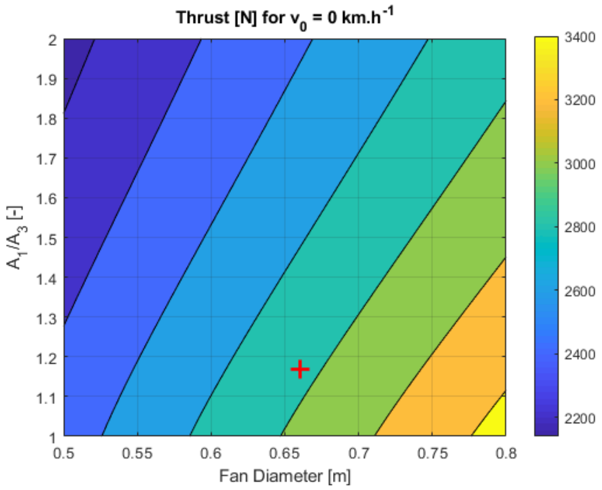

Figure 10. Dependence of static thrust on fan diameter and nozzle contraction ratio A_1/A_3. The selected fan design point parameters are marked by red cross.

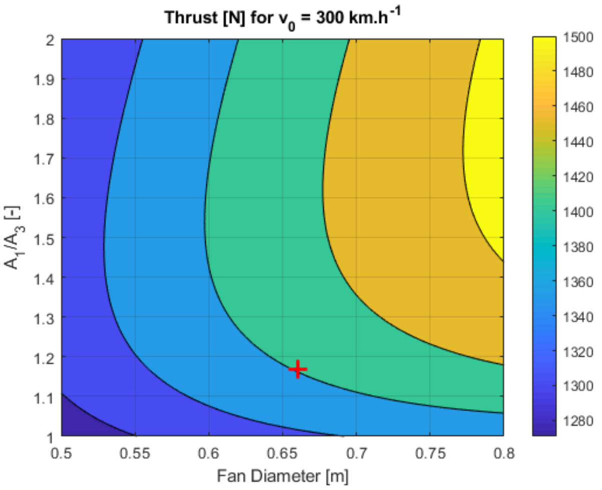

Figure 11. Dependence of thrust at flight speed $v_0 = 300\,\mathrm{km\,h^{-1}}$ on fan diameter and nozzle contraction ratio A_1/A_3. The selected fan design point parameters are marked by red cross.

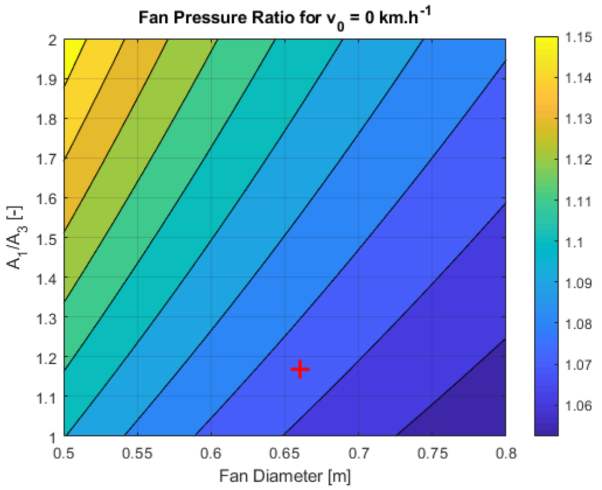

Figure 12. Dependence of fan pressure ratio at flight speed $v_0 = 0\,\mathrm{km\,h^{-1}}$ on fan diameter and nozzle contraction ratio A_1/A_3. The selected fan design point parameters are marked by red cross.

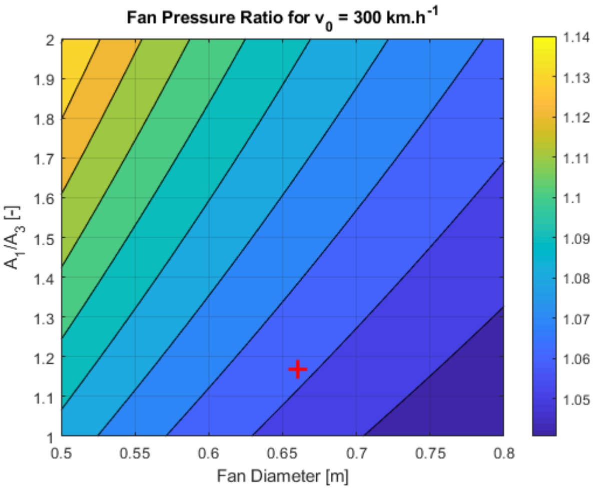

Figure 13. Dependence of fan pressure ratio at flight speed $v_0 = 300\,\mathrm{km\,h^{-1}}$ on fan diameter and nozzle contraction ratio A_1/A_3. The selected fan design point parameters are marked by red cross.

the maximum thrust for each velocity. The optimal value is the maximum of relative thrust mean value for flight velocity $0\,\mathrm{km\,h^{-1}}$ and $300\,\mathrm{km\,h^{-1}}$. This gives an optimal value of A_1/A_3 equal to 1.17. The resulting performance of the propulsion system is then determined for this case, see Figures 19 and 20. Also, the dependence of the fan design parameters on the flight velocity is computed, i.e. fan pressure ratio Π in Figure 21, fan axial velocity v_0 in Figure 22 and fan RPM n_m in Figure 23.

4. Discussion

The presented results show that the high static thrust requirement is in conflict with the high cruise speed requirement (i.e. high thrust at high flight velocity) as expected from the general aircraft propulsion theory. This is clearly visible in Figure 18. The UL-39 light-sport aircraft is used as an example for this computation; the results for similar aircrafts are expected to be comparable. That is why the optimal system configuration is set by means of relative thrust. The outputs of this method are the fan design parameters presented in Table 3.

5. Conclusions

The results of the propulsion system simulation for ducted fan aircraft are presented. A compressible fluid flow model is used so the described procedure can be used for a wider range of flight velocities in comparison with a simple, incompressible flow model (e.g. [4]). The procedure is described and results are presented for the example of the UL-39 aircraft. The requirements for the propulsion system are contradictory, i.e. short take-off distance and high maximal

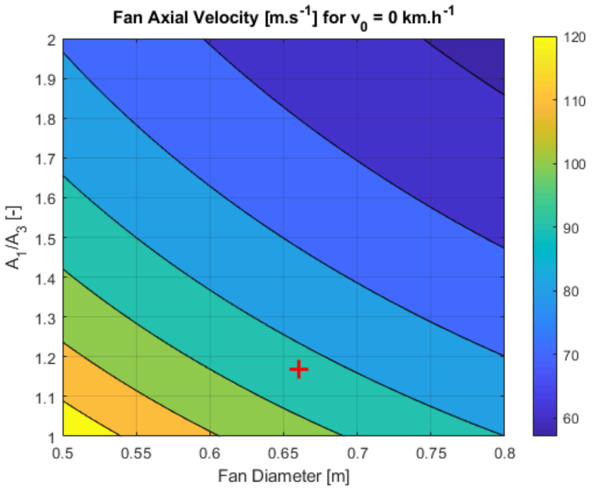

Figure 14. Dependence of fan axial velocity component at flight speed $v_0 = 0\,\mathrm{km\,h^{-1}}$ on fan diameter and nozzle contraction ratio A_1/A_3. The selected fan design point parameters are marked by red cross.

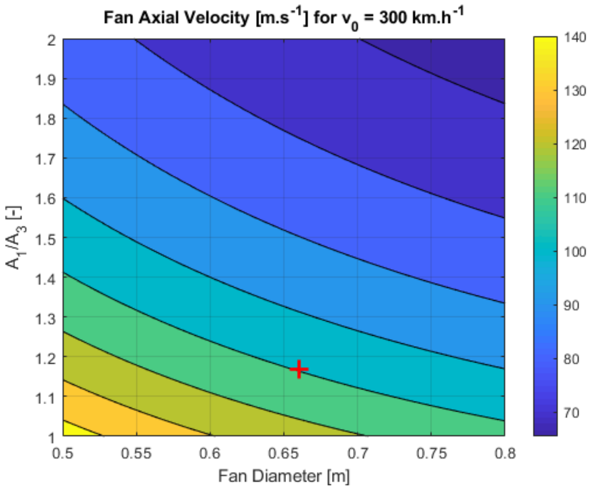

Figure 15. Dependence of fan axial velocity component at flight speed $v_0 = 300\,\mathrm{km\,h^{-1}}$ on fan diameter and nozzle contraction ratio A_1/A_3. The selected fan design point parameters are marked by red cross.

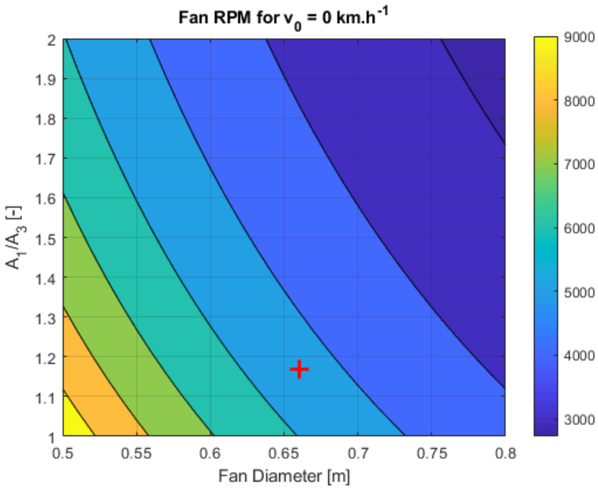

Figure 16. Dependence of fan RPM at flight speed $v_0 = 0\,\mathrm{km\,h^{-1}}$ on fan diameter and nozzle contraction ratio A_1/A_3. The selected fan design point are marked by red cross.

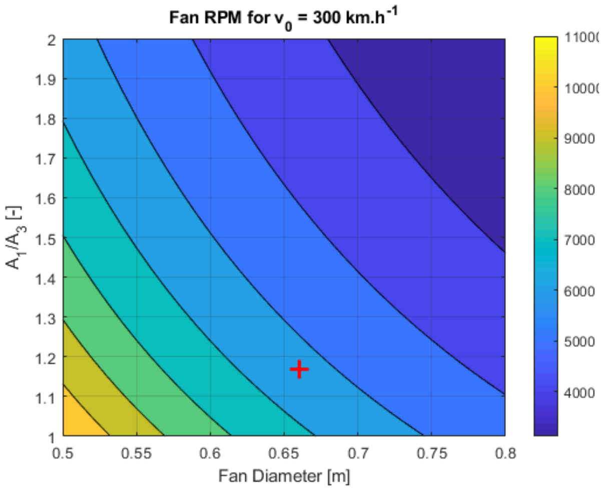

Figure 17. Dependence of fan RPM at flight speed $v_0 = 300\,\mathrm{km\,h^{-1}}$ on fan diameter and nozzle contraction ratio A_1/A_3. The selected fan design point parameters are marked by red cross.

Fan pressure ratio Π	1.062
Fan diameter D	660 mm
Electric motor RPM	6340
Air axial velocity at fan v_{ax}	$109.54\,\mathrm{m\,s^{-1}}$
Fan air mass flow $\dot{m}$	$33.46\,\mathrm{kg\,s^{-1}}$
Expected thrust at $300\,\mathrm{km\,h^{-1}}$ T	1401.9 N
Expected efficiency at $300\,\mathrm{km\,h^{-1}}$ η	0.584

Table 3. UL-39 fan design parameters for flight speed $300\,\mathrm{km\,h^{-1}}$ at sea level international standard atmosphere and electric motor power 200 kW.

flight velocity. This leads to the necessity of a trade-off for chosing the optimal system configuration. The influence of various design parameters on the propulsion performance is presented for the expected range of flight velocities. The proposed selection of the optimal variant is based on the maximum of mean relative thrust for the static case (i.e. flight velocity of $0\,\mathrm{km\,h^{-1}}$) and the expected high speed cruise (i.e. flight velocity of $300\,\mathrm{km\,h^{-1}}$). The presented procedure and the results can be used for a ducted fan design for an electric powered aircraft.

List of symbols

a	Speed of sound $[\mathrm{m\,s^{-1}}]$
A	Cross-section area of a duct $[\mathrm{m^2}]$
c_p	Specific heat at constant pressure $[\mathrm{J\,kg^{-1}\,K^{-1}}]$
D_1	Fan diameter [m]
L	Duct length [m]

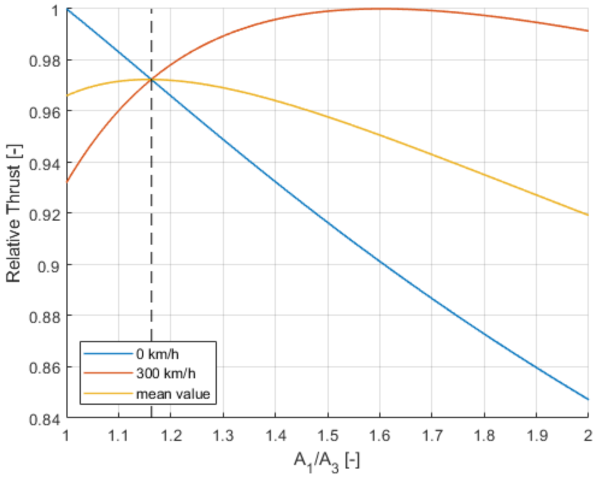

Figure 18. Dependence of relative thrust on nozzle contraction ratio A_1/A_3 at flight speed 0 and 300 km h^{-1}. The selected nozzle contraction ratio $A_1/A_3 = 1.17$ is marked by dashed line.

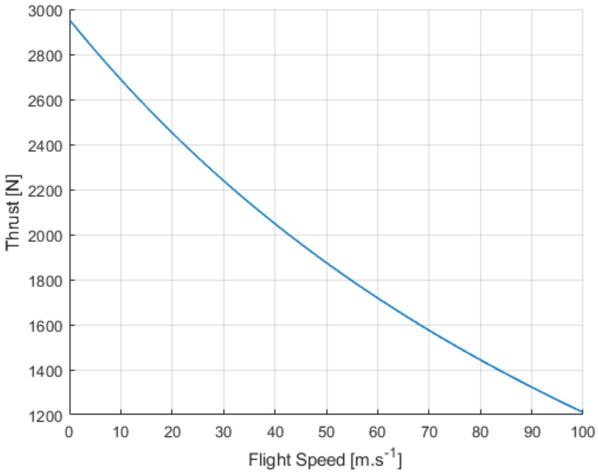

Figure 19. Thrust over flight speed for chosen fan parameters, i.e. $D_1 = 0.66$ m and $A_1/A_3 = 1.17$.

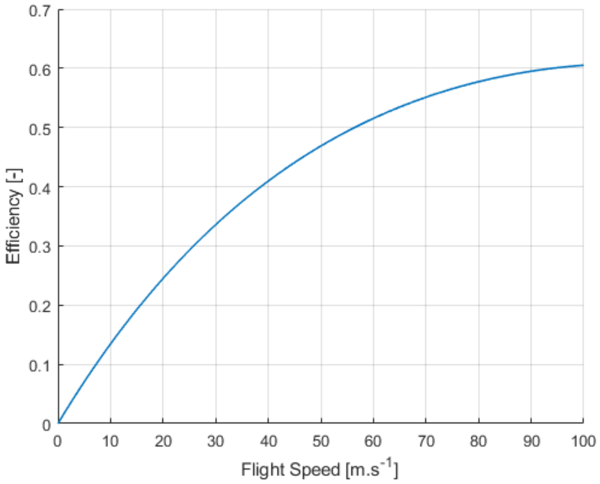

Figure 20. Propulsive efficiency over flight speed for chosen fan parameters, i.e. $D_1 = 0.66$ m and $A_1/A_3 = 1.17$.

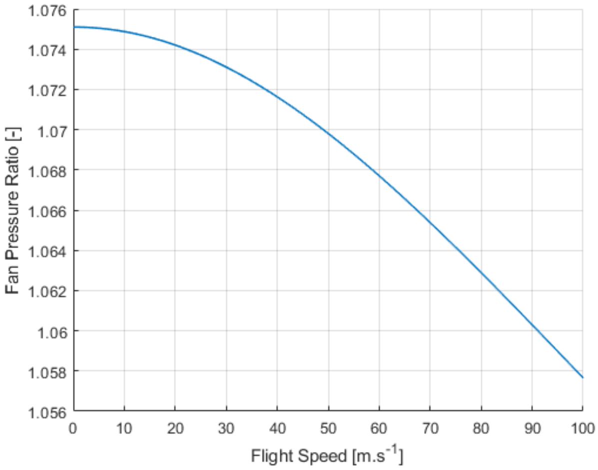

Figure 21. Fan pressure ratio over flight speed for chosen fan parameters, i.e. $D_1 = 0.66$ m and $A_1/A_3 = 1.17$.

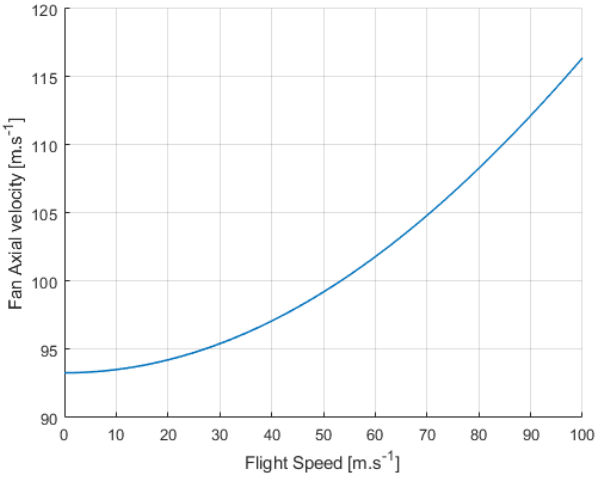

Figure 22. Fan axial velocity component over flight speed for chosen fan parameters, i.e. $D_1 = 0.66$ m and $A_1/A_3 = 1.17$.

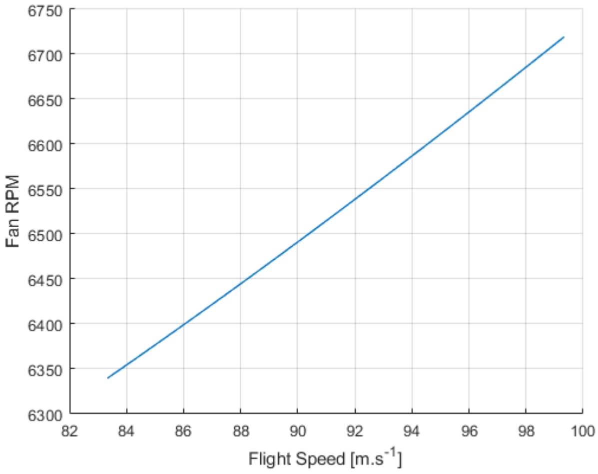

Figure 23. Fan RPM over flight speed for chosen fan parameters, i.e. $D_1 = 0.66$ m and $A_1/A_3 = 1.17$.

$\dot{m}$	Air mass flow $[\mathrm{kg\,s^{-1}}]$
M	Mach number
n_m	Fan RPM [RPM]
p_s	Static pressure [Pa]
p_t	Total pressure [Pa]
P	Engine power [W]
r	Air specific gas constant $[\mathrm{J\,kg^{-1}\,K^{-1}}]$
T	Thrust [N]
T_t	Total temperature [K]
T_s	Static temperature [K]
v	Velocity $[\mathrm{m\,s^{-1}}]$
η	Efficiency
ζ	Pressure loss coefficient
κ	Ratio of specific heats
λ	Wall friction factor
Π_{12}	Fan Pressure ratio
ρ	Air density $[\mathrm{kg\,m^{-3}}]$
(ρv)	Flow density $[\mathrm{kg\,m^{-2}\,s^{-1}}]$
$(\rho v)_c$	Critical flow density $[\mathrm{kg\,m^{-2}\,s^{-1}}]$

ACKNOWLEDGEMENTS

This work was supported by Technology Agency of the Czech Republic, grant No. FV40263.

REFERENCES

[1] M. Hepperle. Electric flight – Potential and limitations. *Energy Efficient Technologies and Concepts of Operation* (STO-MP-AVT-209), 2012. Accessed 2022-10-26, `https://elib.dlr.de/78726/`.

[2] Electric & hybrid-electric propulsion, 2022. Accessed 2022-10-26, `https://aerospace.honeywell.com/us/en/products-and-services/product/hardware-and-systems/electric-power/hybrid-electric-electric-propulsion`.

[3] Rolls-Royce plc. Rolls-royce advances hybrid-electric flight with new technology to lead the way in advanced air mobility, 2022. Accessed 2022-10-26, `https://www.rolls-royce.com/media/press-releases/2022/22-06-2022-rr-advances-hybrid-electric-flight-with-new-technology.aspx`.

[4] S. D. V. Weelden, D. E. Smith, B. R. Mullins. Preliminary design of a ducted fan propulsion system for general aviation aircraft. In *AIAA 34th Aerospace Sciences Meeting and Exibit*, 96-0376. `https://doi.org/10.2514/6.1996-376`.

[5] Letecká amatérská asociace ČR. UL 2 - Část I., 2019. Accessed 2022-10-26, `https://www.laacr.cz/SiteCollectionDocuments/predpisy/UL2%20%C4%8D%C3%A1st%20I_26.3.2019.pdf`.

[6] Deutscher Aero Club. Lufttüchtigkeitsforderungen für aerodynamisch gesteuerte Ultraleichtflugzeuge LTF-UL vom 15.01.2019 und Änderung vom 28.02.2019 (NfL 2-459-19), 2019. Accessed 2022-10-26, `https://www.daec.de/fileadmin/user_upload/files/2019/Luftsportgeraete_Buero/LTF/LTF-UL_2019.pdf`.

[7] N. A. Cumpsty. *Compressor Aerodynamics*. Krieger Publishing Company, 2nd edn., 2004.

[8] R. O. Bullock, I. A. Johnsen. *Aerodynamic Design of Axial Flow Compressors*. NASA-SP-36. NASA Lewis Research Center, Cleveland, OH, 1965.

[9] R. Theiner, J. Brabec. Experience with the design of ultralight airplane with unconventional powerplant. *Proceedings of the Institution of Mechanical Engineers, Part G; Journal of Aerospace Engineering* **232**(14):2721–2733, 2018. `https://doi.org/10.1177/0954410018774117`.

[10] J. Hejna. *Intake Desing for Experimental Fan*. Master's thesis, Czech Technical University in Prague, 2021. Accessed 2022-10-26, `http://hdl.handle.net/10467/96889`.

[11] S. Farokhi. *Aircraft Propulsion*. John Wiley & Sons, 2nd edn., 2014.

[12] S. Albrig. *Angewandte Strömungslehre*. Akademie-Verlag, 5th edn., 1978.

Acta Polytechnica **62**(5):558–566, 2022
https://doi.org/10.14311/AP.2022.62.0558

Published by the Czech Technical University in Prague

PERFORMANCE ASSESSMENT OF STEEL TRUSS RAILWAY BRIDGE WITH CURVED TRACK

Michal Venglár*, Katarína Lamperová, Milan Sokol

Slovak University of Technology, Faculty of Civil Engineering, Department of Structural Mechanics, Radlinského 11, 810 05 Bratislava, Slovakia

* corresponding author: michal.venglar@stuba.sk

Abstract. Non-destructive Structural Health Monitoring techniques can be incorporated into bridge integrity management by assessing structural conditions. This paper describes a performance assessment of a steel truss railway bridge in Bratislava using vibration-based techniques as a further part of maintenance in addition to standard visual inspections. To obtain the necessary data, a multipurpose measuring system was used. Various types of data were measured, e.g. accelerations, strains, and displacements. The advantage of the multipurpose measuring system was that the traffic over the bridge was not restricted, even though the bridge carries only a single curved track. Two test campaigns were conducted to assess the performance of the bridge. One campaign was devoted to measuring ambient vibrations in order to perform the operational modal analysis, and the second was carried out to measure strains and displacements during a train passage. The results show a successful system identification of the structure using ambient vibrations; and a finite element model was verified and validated by a comparison of strains and displacements, as well as by modal parameters. According to the results obtained, the structural health of the investigated bridge was satisfactory.

Keywords: System identification, performance assessment, steel truss bridge, ambient vibration, train passage, FEM model, curved track.

1. Introduction

Bridges represent critical components of transportation networks, whether road or railway. Therefore, administrators of railway networks around the world are the most responsible for ensuring the integrity of the networks with railway bridges being an integral part of these networks. In many countries, only visual inspections are periodically carried out on bridges to detect structural deviations. To illustrate on the example of Slovakia: The Railways of the Slovak Republic (ŽSR) have their own rules of bridge inspection and the standard visual inspection of every bridge is carried out by the employees of ŽSR once every three years, unless the bridge is in poor condition (according to the rating index). Maintenance activities can be prioritised accordingly. However, the results of visual inspections depend on the skill of the inspectors and can be strongly affected by human errors and, therefore, sometimes not be reliable. In addition to that, they are time-consuming [1]. However, an interesting project “Methods for achieving sustainability of industrial heritage steel bridges” with ID: DG18P02OVV033 is being solved in the Czech Republic to check and verify the state of steel bridges, as well as to ensure integrity of the important parts of networks. The book [2] shows some results of that project. Main failures are also summarised there, e.g. fatigue cracks, corrosion (loss of material), extreme deflections caused by various accidents, malfunction of supports, or simple degradation during operation. As a result of this state, additional testing techniques, such as structural health monitoring (SHM) [3, 4] are required. According to [5], SHM could be combined with and supplement visual inspections, which, however, cannot be omitted. According to [6], the information obtained by SHM should also be used in decision-making of administrators, and interdisciplinary cooperation is necessary. At the same time, information must be based on thoughtful measurements and analyses, and not on subjective estimates. Besides that, the costs of experimental tests are negligible as compared to bridge renovation costs [7].

In recent years, various approaches to SHM have been established, for example, classical SHM (described in the following paragraph) or inverse SHM approach (with moving sensors) used mainly on railway bridges [8–10]. However, researchers also study the possibility of using low-cost sensors as stationary real-time systems [11]. In the research field of vibration-based SHM methods [12–19], the system identification is mentioned as the first step [20] to determine the current health of the structure [21]. The task involves the identification of a dynamic system, which is described by specific stiffness, damping, and mass parameters [22, 23]. After that, various damage detection and localisation algorithms can be used [24].

Therefore, in this paper, the initial system identification of the observed steel truss railway bridge (Figure 1) is described and the first results are stated to represent a background for future measurements and decision-making by the administrators. The paper also details the preparation and the performance

Figure 1. Steel truss railway bridge in Bratislava.

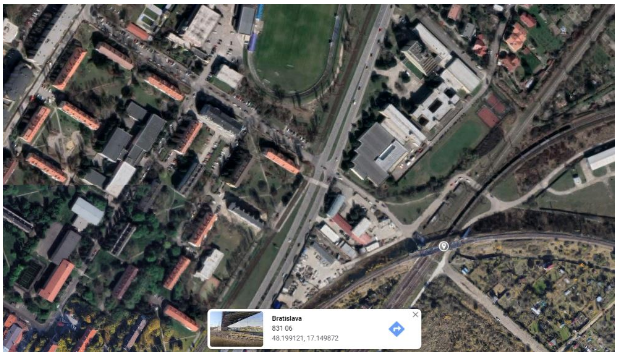

Figure 2. Location of the steel truss railway bridge in Bratislava, from [25].

of dynamic tests (together with the quasi-static one) carried out during the first phase of the investigation. In this case, the fact that the track on the bridge is curved also posed a problem. As a result of this curvature, the overall stress distribution, especially on the bridge deck elements, but also on the main girders, depends not only on the weight of a particular train but also on its speed and the corresponding horizontal centrifugal force.

The paper consists of several sections: Section 2 describes the bridge; Section 3 deals with the preparation of experimental measurements, e.g. the characterisation of the FEM model and the placement of sensors; Section 4 is devoted to the analyses of measured accelerations; the strains are compared with numerical calculations; Section 5 discusses the results. Finally, the main conclusions are presented in Section 6.

2. Bridge description

The steel bridge is located at kilometer 6.124 of the main connection between Bratislava and Žilina and crosses over the four tracks of the line no. 120 (see Figure 2). The track connects the stations Bratislava – Vineyards and Bratislava – East on the line no. 609. The load-bearing structure of the single span-bridge (the total span is 56 m) consists of two main truss girders with a lower open bridge deck. The bridge deck consists of floor beams (with a length of 6.3 m) and stringers (with a length of 5.6 m). The structure has pinned supports on the side of the Bratislava – East station (Figure 1, on the left side and Figure 3, on the right side) and rollers towards the Bratislava – Vineyards station.

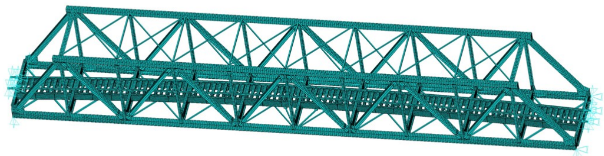

Figure 3. Initial FEM model with curved track.

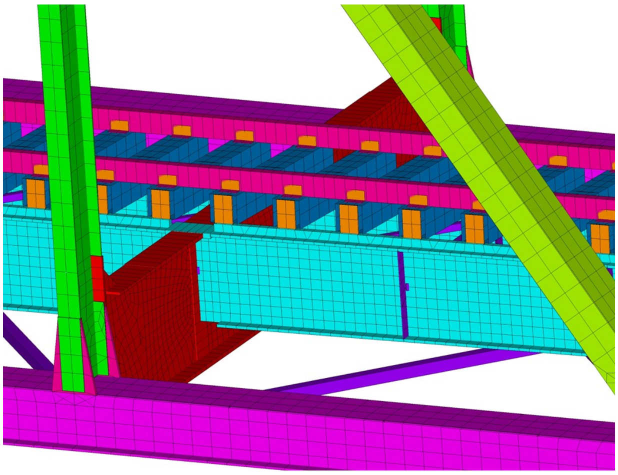

Figure 4. Detail of the FEM model with curved track.

The substructure consists of reinforced concrete supports with sloping wing walls. The bridge carries a single-track railway (Figure 3) (which is curved with a radius of 400 m and is also elevated) with a speed limit of 80 km h^{-1}.

3. Preparation and execution of tests

Dynamic tests were performed twice in a one-month period. According to [26], the sensor configuration is the key factor of the entire testing process. Therefore, the bridge was equipped with various sensors, for example, accelerometers, strain gauges, and thermocouples. IBIS-S interferometric radar was also used to measure bridge displacements. These sensors and devices were used to form a multipurpose measuring system [27]. The measurements were preceded by a review of available project documentation and preparation of the initial finite element method (FEM) model. The initial modal analysis was performed using this FEM model to determine the optimal placement of the accelerometers. A quasi-static analysis was also carried out numerically to obtain expected stresses on the stringers, where strain gauges were installed as half-bridge completions.

3.1. FEM model

The detailed numerical model (Figure 3) of the bridge was prepared. A special attention was paid to modelling the surface bridge deck, which was guided along a curve. To monitor stresses in detail in any place, the load-bearing components (lower and upper chords, diagonal members, floor beams, stringers, and bracings)

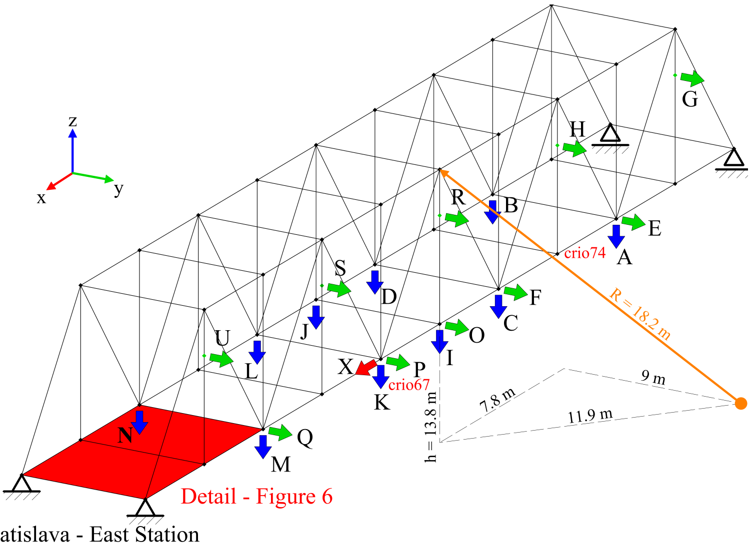

Figure 5. Locations of accelerometers and IBIS-S radar along the bridge.

were mostly modelled as shell elements of appropriate dimensions (according to the documentation). In addition, rails and sleepers were also modelled for a proper load distribution (Figure 4).

The materials used are described in the following Table 1.

Material	E [GPa]	Poisson's ratio [-]	Density [kg m^3]
Steel	210	0.30	7850
Wood	13	0.40	800

Table 1. Characteristics of the materials used.

The weight of the entire structure, including rails, sleepers, and other non-bearing parts of the structure such as sidewalks and railings, is approximately 240 tons. The non-bearing structure parts were modelled as added mass.

3.2. Sensor network

The chosen positions of the accelerometers (Figure 5) were determined from the initial modal analysis performed on the FEM model described above.

The acceleration was measured in the vertical directions (in the direction of Z axis) by ten sensors to identify the vertical bending and torsional mode-shapes. In addition, ten other sensors were positioned in the horizontal direction. These were used to analyse horizontal (in the direction of the Y axis) and torsional mode-shapes. The last two sensors were used to determine whether the sliding supports work properly. In order to eliminate future environmental effects on modal parameters, temperature sensors were placed in proximity of the chosen accelerometers. Six contact thermocouples were positioned evenly along the bridge. The other two sensors measured air temperature. Furthermore, several strain gauges (Figure 6) were attached to the second stringers from the side of the fixed supports (the station Bratislava – East).

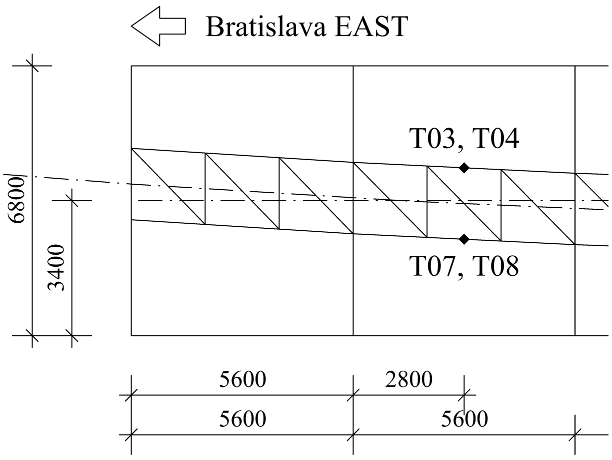

Figure 6. Locations of strain gauges on the bridge.

3.3. Interferometric radar IBIS-S

The IBIS-S interferometric radar represents a device suitable for measuring displacements of several points along the structure. The radar transmits microwave frequencies in short pulses and, based on the time difference between the transmitted and received signals, the displacements of multiple points of the structure are determined [28]. Depending on the intensity of the reflected signal, a measurement accuracy of 0.1 mm can be easily achieved. The use of radar interferometry is, therefore, highly suitable for measuring the response of bridges without traffic restrictions.

Although it is possible to measure at several locations at the same time, in this case, for the sake of simplicity, attention was paid to measuring displacements in one location only. The interferometric radar was oriented toward the upper joint of the main truss girder. The exact measured point (Figure 7) is located

Figure 7. Exact point of the bridge structure monitored by IBIS-S radar.

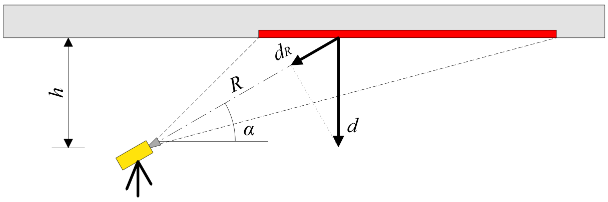

Figure 8. Projection of the measured displacement d_R.

on the main girder of the bridge, in the middle of the span.

The radar measures displacements (changes in distance) in the radial direction d_R (Figure 8). The radial displacement d_R can be projected into the direction of the effective displacement d (in this case in the vertical direction) according to (1).

$$d = \frac{d_R}{\sin\alpha} = d_R \frac{R}{h} \tag{1}$$

The position of the radar is marked with an orange dot in Figure 5. The orange arrow shows the radial distance R between the measured point and the radar. In this case, R was approximately 18.2 m.

3.4. Performance of the dynamic tests

As mentioned above, measurements were performed over two days, one month apart. The temperature reached 5 °C at the time of the first observation and 10 °C on the second day of the test.

One campaign was devoted to measuring ambient vibrations in order to perform the operational modal analysis, and the second to measuring strains and displacements during train passages. In the course of the measurements, the IBIS-S radar was located near the abutment with fixed supports (Figure 5).

The displacement measurements were performed in a dynamic mode with a sampling frequency of 200 Hz and a resolution of the measured points equal to 0.75 m.

The traffic on the bridge is usually not very heavy; therefore, many records of ambient vibrations were logged using the multichannel data acquisition (DAQ) system. Hence, dynamic properties could be extracted from the ambient data. Additionally, the passages of locomotives and cargo trains were recorded during the second campaign. The stiffness parameter of the FEM model was verified by a quasi-static test of the passing train. The behaviour of the bridge deck, mainly of the most loaded stringers, was compared to the calculated stresses.

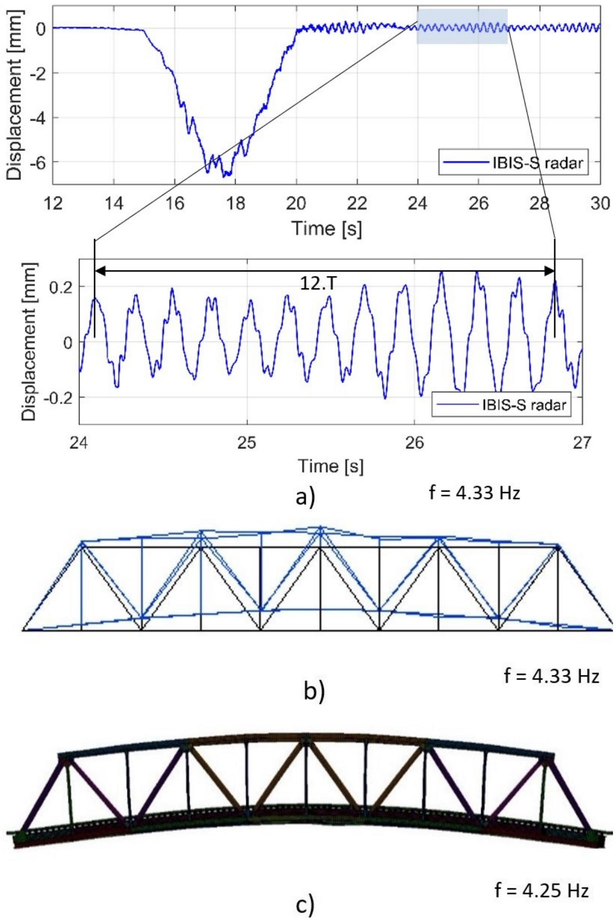

Figure 9. The second identified natural frequency a) vertical displacements caused by the train passage b) mode-shape from the measured accelerations, and c) mode-shape obtained by the FEM model.

4. Bridge performance assessment

4.1. Analyses of measured data

Ambient vibration data were prepared using the codes for pre-processing and processing (using stochastic subspace identification – SSI), as mentioned in [29]. The data were then used similarly in the ModalVIEW software as in [30]. The discrete-time Fourier transform (DTFT; described in [31]) was used to identify natural frequencies from the measured displacements in order to compare them to those identified from the measured accelerations.

As can be seen in Figure 9 a), the displacements were extracted after the train (the single locomotive

Mode-shape no.	Description	Calculated freq. [Hz]	Measured freq. [Hz]	Cross-MAC [-]
1	in Y direction	2.48	2.56	0.99
2	in Z direction	4.25	4.33	0.99
3	in Y direction	4.50	4.78	0.98
4	in Y direction	6.16	6.48	0.99
5	around X axis	7.11	7.42	1.00
6	in Y direction	8.33	8.85	0.96
7	in X direction	9.39	–	–
8	in Z direction	11.31	11.09	0.95
9	in Y direction	11.37	11.91	0.92

Table 2. Comparison of identified mode-shapes and corresponding natural frequencies, as well as Cross-MAC values.

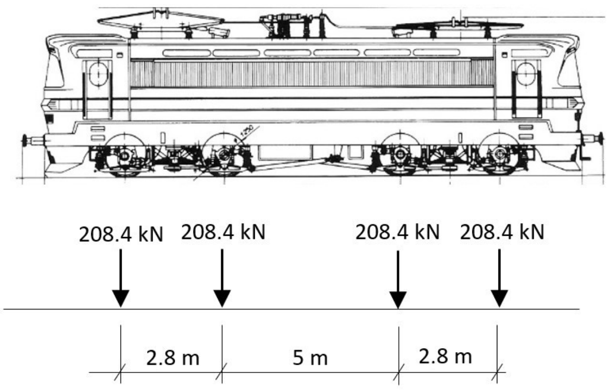

Figure 10. Locomotive type 240 with axle loadings and spacings.

Mode-shape no.	Description	Identified damping [%]
1	in Y direction	1.32
2	in Z direction	2.34
3	in Y direction	0.76
4	in Y direction	1.43
5	around X axis	1.39
6	in Y direction	0.85

Table 3. Identified damping ratios for individual mode-shapes.

240 – Figure 10) left the bridge, that is, between 24–27 s. The train speed during this passage (in the first campaign) was approximately 40 km/h. This is also described in Section 4.3 in more detail.

4.2. System Identification

Natural frequencies and damping were identified using the SSI method. It can be seen in Table 2 that the calculated and obtained natural frequencies are in good agreement. Furthermore, Cross-MAC values were calculated similarly as in [32], and the values obtained ensured that a model update of the initial FEM was unnecessary. This can prove that the bearing structure has not shown any critical damage (malfunction of the supports or extreme deflections of members) since it was opened in 1976. Moreover, the real structure shows slightly greater parameters of stiffness. Identified damping ratios (Table 3) are valuable information for a future part of the study, when the remaining fatigue life will be calculated.

4.3. Quasi-static test

The above-mentioned fact that the stiffness was slightly greater was also confirmed by the measurement of displacement. For example, the measured displacement during train passages (quasi-static part of the displacement in the middle of the bridge, on the side of the outer curve of the railway) reached approximately 6.3 mm representing approximately 95 % of the quasi-static displacement calculated using influence lines.

The eccentricity of the vertical load (uneven distribution of the vertical load on the individual rails) must also be taken into consideration in the calculations due to the centrifugal force Q_h, which arises because the railway track is curved. The eccentricity of the vertical load e was calculated according to the geometry in Figure 11:

$$e = \frac{u}{s} h_C, \tag{2}$$

where h_C is the value of the centrifugal forces above the top plane of the rails and u is the value of the height difference between two rails. According to [33], the height h_C is 1.8 m. The parameter s is the track gauge and, in most cases in Slovakia, has a value equal to 1.435 m. The magnitude of the centrifugal forces depends on the speed of the train [33] and is given as:

$$Q_H = \frac{Mv^2}{r}, \tag{3}$$

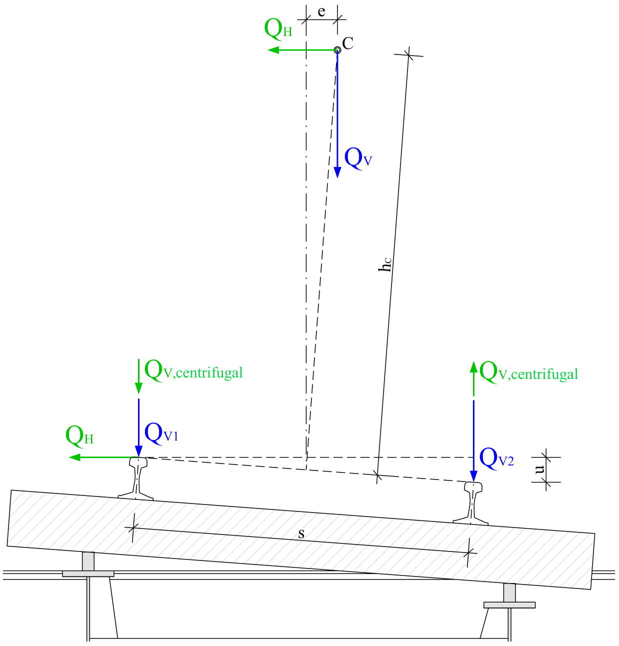

Figure 11. Scheme of quasi-static axle forces.

where M is the mass per axle, v is the speed of the passing train, and r is the radius of the track curve. Vertical forces $Q_{V,centrifugal}$ were calculated according to:

$$Q_{V,centrifugal} = \frac{Q_H h_c}{s}. \tag{4}$$

The redistribution of the total vertical axle force Q_V was determined according to the following equation:

$$Q_{V1} = \frac{Q_V(\frac{s}{2} - e)}{s} \tag{5}$$

$$Q_{V2} = \frac{Q_V(\frac{s}{2} + e)}{s}, \tag{6}$$

where Q_{V1} is the vertical axle force for the inner curve of the track (rail with a smaller radius), and Q_{V2} is the vertical axle force for the outer curve. Due to the geometry of the track (Figure 11), the rail in the inner curve would be subjected to a load higher by 46 % higher under static action or at extremely low speeds [33]. However, the size of the load on individual rails is significantly affected by the value of centrifugal forces. The load on the rail on the outer curve increases with increasing speed. Unlike bridges with straight rails, the expected response of the structure may be different on the side closer to the outer curve and on the side closer to the inner curve. The railway locomotive – type no. 240 is 16 m long, and Figure 10 shows the axle load and axle spacing of the locomotive used for the quasi-static test. The total weight is 85 tons.

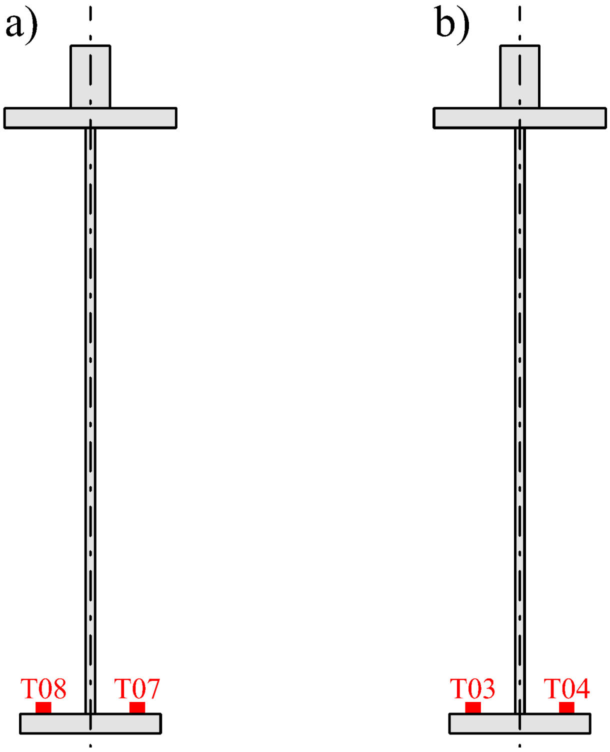

Figure 12. Strain gauges (T03, T04, T07 and T08) attached to the second stringers a) outer b) inner.

4.4. Comparison of the strain on the stringers

The same locomotive was used to calculate the strain on the stringers. The influence lines calculated by the numerical model were utilised to perform the quasi-static analysis. It can be seen in Figure 12 that the strain gauges were installed on the bottom flange of the second stringers in the middle of the span.

Figs. 13 and 14 show the comparison between calculated and measured stresses during the train passage. The outer stringer (Figure 13) shows a better agreement between the calculation and the measurement. As a result, there is no evidence that the investigated part of the bridge deck is damaged (e.g., by corrosion). In the case of the inner stringer (Figure 14), the difference is up to 25 % . It can be seen that the measured stresses are smaller than the calculated ones. This is due to the fact that some non-structural parts (rails, sleepers) also carry a part of the load and it is likely that the thickness of the steel elements is slightly greater than assumed in the analysis – the geometry in FEM analysis was taken from the design values. Other possible reasons should be investigated in more detail in the future. We generally consider the agreement between the measured and calculated stresses to be very good. The difference in the accuracy of the agreement of the results between Figs. 13 and 14 may be caused by an inaccurate determination of the train speed, which influences the distribution of the load between the outer and inner stringer. This can be seen in small differences when the minimum

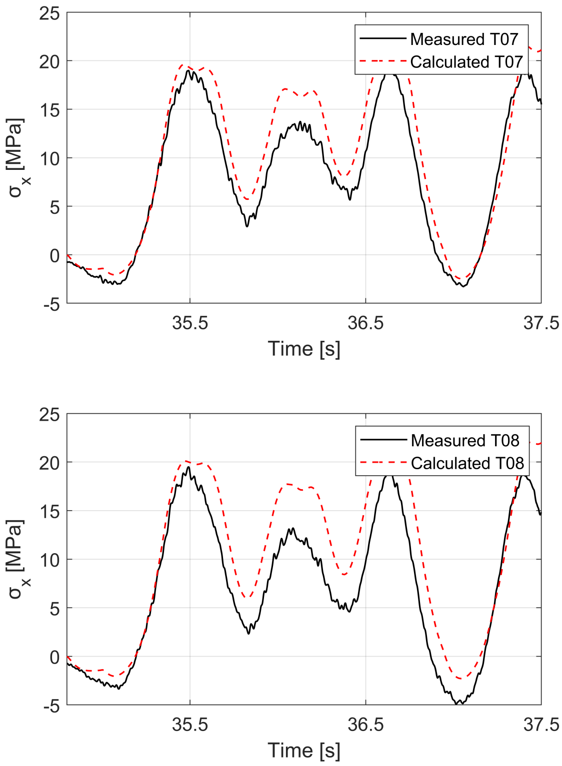

FIGURE 13. Comparison of normal stresses on the outer stringer – strain gauges: T07 (top) and T08 (bottom).

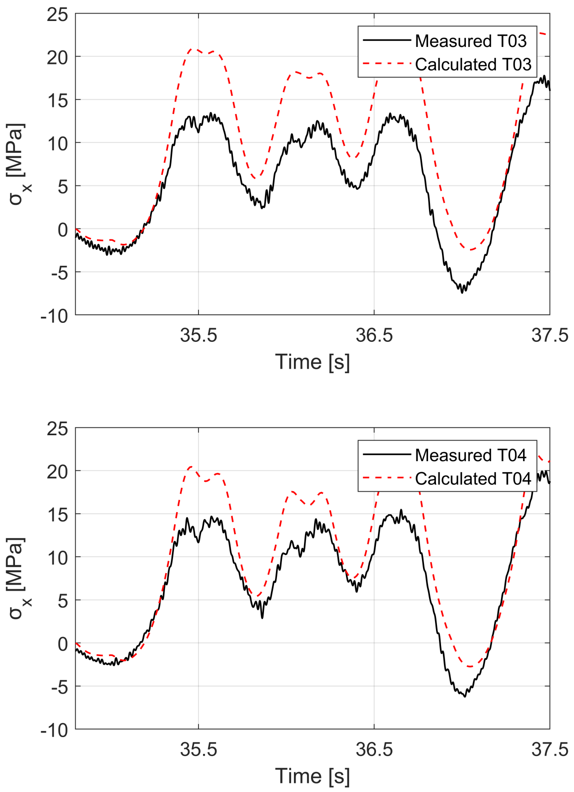

FIGURE 14. Comparison of normal stresses on the inner stringer – strain gauges: T03 (top) and T04 (bottom).

values occur. At a time of about 35.25 s, there is a good agreement, and at a time of 36.75 s, the measured minimum of stresses occurs a little earlier. This result points to the importance of considering multiple details in structural health monitoring.

4.5. COMPARISON OF DISPLACEMENTS

Figure 15 shows a comparison of the measured and calculated displacements of the monitored point of the structure (Figure 7). In this case, the resulting values arise due to the passage of a train consisting of only two connected locomotives (both no. 240, Figure 10). During the second measuring campaign, the locomotives moved at a speed of approximately 4.6 km/h. Due to the fact that the bridge was not closed, the trains' speeds were random. However, the slow passage was very useful, allowing a comparison of the measured data with the quasi-static analysis. The difference between the test and analysis values is only 4 %, which is a very satisfactory result. Because the speed and geometry of the track is known, it is possible to estimate the displacement on the opposite side of the bridge cross-section. This consideration concerns only the estimation of the maximum displacement on the bridge. In this case, the value at this point should be 11 % higher than at the measured point (Figure 16).

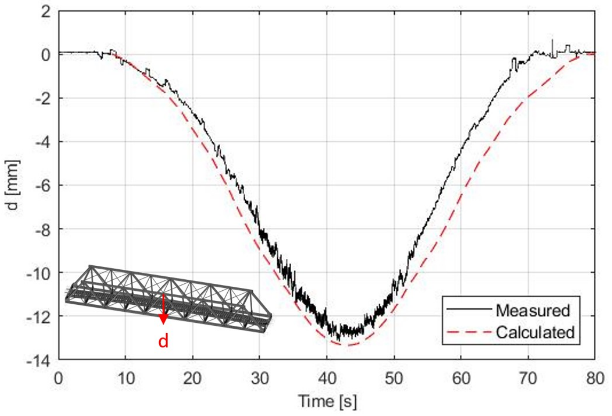

FIGURE 15. Comparison of measured and calculated displacement.

This value could be verified, e.g. by synchronized measurement with two radars on both sides of the structure or by a radar on one side and another measuring device on the other side of the bridge. These results show that we can relatively accurately determine the deflections of any load that occur during the measurement on the bridge using this method of measurement and a subsequent analysis. The results show that an agreement between the measured and calculated values can be achieved up to a level of ±5 %. The presented results proved the above-mentioned results from the operational modal analysis. Any larger difference between the measured and calculated values can lead to the acquisition of important data on the incorrect response of the bridge, and, consequently,

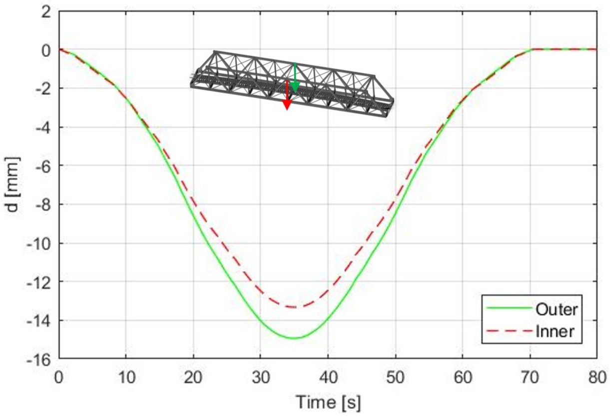

Figure 16. Comparison of maximum displacements on both sides of the cross-section.

such a result can serve as an impulse for the responsible authorities that something is wrong with the bridge and it needs due attention.

5. Discussion

The results obtained confirm that the system identification was successful thanks to the satisfactory measurements performed as well as an accurate FEM model. Damping ratios represent highly valuable information. The remaining fatigue life can be evaluated in the future using the values obtained. It is necessary to state that the FEM model was prepared in more detail (rails were also modelled), and the documentation was, fortunately, sufficient. Due to this, the results of the initial FEM model were comparable to those of the measurements. The results can also be used to estimate possible deviations of the variance between the measurement results and numerical analysis, which, in our case, reaches 5 % for displacements and about 15–25 % for stresses. The possible reasons of differences in strains should be investigated in more detail in the future. It is also highly valuable that a good agreement of the results was achieved, even though it was a complicated case where the track is led over a bridge in a curve. As previously mentioned, measurements with radars on both sides of the structure can be carried out in the future to verify uneven displacements also experimentally. IBIS-S radars have the possibility to synchronize two or more radars.

6. Conclusions

In this study, a performance assessment of a curved track steel rail bridge was performed. In order to do that, a FEM model had to be created. Then, all measurements were performed without interruptions to the traffic over and under the bridge. This fact can prove to be an added value (performed in the presented way) for administrators of the infrastructure, as it allows for obtaining complementary information (in addition to the visual inspection) about the structure without any disruptions. The data acquired and analysed show that it is not necessary to update the FEM model. All comparisons show an exact agreement between the real behaviour and the state modelled according to the available documentation and visual inspections. Because of that, the verified and validated FEM model can be used for a prediction analysis in the future. Consequently, it can be stated that there is no indication of any serious damage to the investigated structure after almost 50 years of operation (at the time of the tests). These results can also be used as a comparative base for future repetitions and as an additional information for the decision makers at ŽSR.

Acknowledgements

The authors gratefully acknowledge the contribution of the Scientific Grant Agency of the Slovak Republic under the grant VEGA no. 1/0230/22.

References

[1] S. C. Siriwardane. Vibration measurement-based simple technique for damage detection of truss bridges: A case study. *Case Studies in Engineering Failure Analysis* **4**:50–58, 2015. `https://doi.org/10.1016/j.csefa.2015.08.001`.

[2] P. Ryjáček, T. Rotter, V. Stančík, et al. *Metody pro zajištění udržitelnosti ocelových mostních konstrukcí industriálního kulturního dědictví [Methods for Achieving Sustainability of Industrial Heritage Steel Bridges]*. First printing. Czech Technical University in Prague, Prague, 2022. ISBN 978-80-01-06990-5.

[3] C. Comisu, N. Taranu, G. Boaca, M. Scutaru. Structural health monitoring system of bridges. *Procedia Engineering* **199**:2054–2059, 2017. `https://doi.org/10.1016/j.proeng.2017.09.472`.

[4] H. Ceylan, K. Gopalakrishnan, S. Kim, et al. Highway infrastructure health monitoring using micro-electromechanical sensors and systems (MEMS). *Journal of Civil Engineering & Management* **19**(1):188–201, 2014. `https://doi.org/10.3846/13923730.2013.801894`.

[5] P. Haardt, R. Holst. Monitoring during life cycle of bridges to establish performance indicators. In *The Value of Structural Health Monitoring for the reliable Bridge Management*, p. 1–9. 2017. `https://doi.org/10.5592/CO/BSHM2017.4.2`.

[6] M. Limongelli. SHM for informed management of civil structures and infrastructure. *Journal of Civil Structural Health Monitoring* **10**(5):739–741, 2020. `https://doi.org/10.1007/s13349-020-00439-8`.

[7] T. Plachý, M. Polák, P. Ryjáček. Assessment of an old steel railway bridge using dynamic tests. *Procedia Engineering* **199**:3053–3058, 2017. `https://doi.org/10.1016/j.proeng.2017.09.555`.

[8] A. Malekjafarian, E. O'Brien, P. Quirke, C. Bowe. Railway track monitoring using train measurements: An experimental case study. *Applied Sciences* **9**(22):4859, 2019. `https://doi.org/10.3390/app9224859`.

[9] S. Lorenzen, H. Berthold, M. Rupp, et al. *Bridge Safety, Maintenance, Management, Life-Cycle, Resilience and Sustainability*, chap. Deep learning based indirect monitoring to identify bridge natural frequencies using sensors on a passing train, pp. 401–409. CRC Press, 2022. `https://doi.org/10.1201/9781003322641-46`.

[10] S. Urushadze, J. Yau, Y. Yang, J. Bayer. Theoretical and experimental verifications of bridge frequency using indirect method. In *Conference Proceedings of the Society for Experimental Mechanics Series*, pp. 153–158. 2020. `https://doi.org/10.1007/978-3-030-12115-0_20`.

[11] S. Quqa, L. Landi, P. P. Diotallevi. Real time damage detection through single low-cost smart sensor. In *Eccomas Proceedia COMPDYN*, pp. 3914–3925. 2019. `https://doi.org/10.7712/120119.7196.19614`.

[12] P. F. Giordano, M. P. Limongelli. Response-based time-invariant methods for damage localization on a concrete bridge. *Structural Concrete* **21**(4):1254–1271, 2020. `https://doi.org/10.1002/suco.202000013`.

[13] K. Gkoktsi, A. Giaralis, R. P. Klis, et al. Output-only vibration-based monitoring of civil infrastructure via sub-nyquist/compressive measurements supporting reduced wireless data transmission. *Frontiers in Built Environment* **5**:111, 2019. `https://doi.org/10.3389/fbuil.2019.00111`.

[14] E. Giordano, N. Mendes, M. G. Masciotta, et al. Expeditious damage index for arched structures based on dynamic identification testing. *Construction and Building Materials* **265**:120236, 2020. `https://doi.org/10.1016/j.conbuildmat.2020.120236`.

[15] S. Quqa, L. Landi, P. P. Diotallevi. Instantaneous modal identification under varying structural characteristics: A decentralized algorithm. *Mechanical Systems and Signal Processing* **142**:106750, 2020. `https://doi.org/10.1016/j.ymssp.2020.106750`.

[16] R. P. Finotti, A. L. Bonifácio, F. S. Barbosa, A. A. Cury. Evaluation of computational intelligence methods using statistical analysis to detect structural damage. *Mecánica Computacional* **34**(22):1389–1397, 2016.

[17] M. Sysyn, U. Gerber, O. Nabochenko, et al. Indicators for common crossing structural health monitoring with track-side inertial measurements. *Acta Polytechnica* **59**(2):170–181, 2019. `https://doi.org/10.14311/AP.2019.59.0170`.

[18] M. Sysyn, O. Nabochenko, U. Gerber, et al. Common crossing condition monitoring with on board inertial measurements. *Acta Polytechnica* **59**(4):423–434, 2019. `https://doi.org/10.14311/AP.2019.59.0423`.

[19] M. Sysyn, O. Nabochenko, F. Kluge, et al. Common crossing structural health analysis with track-side monitoring. *Communications – Scientific letters of the University of Zilina* **21**(3):77–84, 2019. `https://doi.org/10.26552/com.C.2019.3.77-84`.

[20] Y. Serhat Erdogan, F. Necati Catbas, P. Gundes Bakir. Structural identification (St-Id) using finite element models for optimum sensor configuration and uncertainty quantification. *Finite Elements in Analysis and Design* **81**:1–13, 2014. `https://doi.org/10.1016/j.finel.2013.10.009`.

[21] H.-P. Chen, Y.-Q. Ni. *Structural Health Monitoring of Large Civil Engineering Structures*, chap. 5 Modal Analysis of Civil Engineering Structures, pp. 91–121. 2018. `https://doi.org/10.1002/9781119166641.ch5`.

[22] D. Thorby. *Structural Dynamics and Vibration in Practice*, chap. 13 Vibration of Structures, pp. 367–385. Butterworth-Heinemann, Reading, 2018. `https://doi.org/10.1016/B978-0-7506-8002-8.00013-4`.

[23] T. Grigorjeva. Numerical analysis of the effects of the bending stiffness of the cable and the mass of structural members on free vibrations of suspension bridges. *Journal of Civil Engineering & Management* **21**(7):948–957, 2015. `https://doi.org/10.3846/13923730.2015.1055787`.

[24] R. Wendner, A. Strauss, A. Krawtschuk, et al. Assessment of engineering structures based on influence line measurements & model correction approach. In *Proceedings of the 9th International Probabilistic Workshop*. 2011. `https://www.researchgate.net/publication/323343059_Assessment_of_Engineering_Structures_based_on_Influence_Line_Measurements_Model_Correction_Approach`.

[25] Google. Bratislava - Raca. [2022-08-02], `https://www.google.sk/maps`.

[26] V. Dertimanis, E. Chatzi. Sensor networks in structural health monitoring: From theory to practice. *Journal of Sensor and Actuator Networks* **9**(4):47, 2020. `https://doi.org/10.3390/jsan9040047`.

[27] M. Venglár, K. Lamperová, D. Beutelhauser. *Bridge Safety, Maintenance, Management, Life-Cycle, Resilience and Sustainability*, chap. Application of multipurpose measuring system on various bridges – pros and cons, pp. 324–331. CRC Press, 2022. `https://doi.org/10.1201/9781003322641-36`.

[28] J. Gocal, L. Ortyl, T. Owerko, et al. *Determination of displacements and vibrations of engineering structures using ground-based radar interferometry*. First printing. Wydawnictwa AGH, Krakow, 2013.

[29] M. Venglár, M. Sokol. Case study: The Harbor Bridge in Bratislava. *Structural Concrete* **21**(6):2736–2748, 2020. `https://doi.org/10.1002/suco.201900190`.

[30] J. Krejčí, P. Beneš. A comparison of two modal analysis methods: An impact hammer versus laser vibrometry. *Acta Polytechnica* **60**(5):420–427, 2020. `https://doi.org/10.14311/AP.2020.60.0420`.

[31] L. Wang, S. Lie, Y. Zhang. Damage detection using frequency shift path. *Mechanical Systems and Signal Processing* **66-67**:298–313, 2016. `https://doi.org/10.1016/j.ymssp.2015.06.028`.

[32] M. Sokol, M. Venglár. System identification of a composite beam. *Pollack Periodica* **12**(3):43–54, 2017. `https://doi.org/10.1556/606.2017.12.3.5`.

[33] SÚTN. STN EN 1991-2 Eurocode 1: Actions on structures. Part 2: Traffic loads on bridges, national annex EN 1991-2/NA, 2006.

Acta Polytechnica **62**(5):567–573, 2022
`https://doi.org/10.14311/AP.2022.62.0567`

REDUCTION OF PAVEMENT THICKNESS USING A SUBGRADE LAYER TREATED BY DIFFERENT TECHNIQUES

Raquim N. Zehawi*, Yassir A. Kareem, Emad Y. Khudhair

University of Diyala, College of Engineering, Highway and Airport Engineering Department, Baquba 32001, Iraq
* corresponding author: `raquim_zehawi@uodiyala.edu.iq`

Abstract. A range of stabilisers for poor quality subgrade soils have been developed to promote road constructions. Many of them are becoming more popular depending on their effectiveness. The purpose behind this research is to identify the relative efficacy of many physical and chemical stabilisation techniques for enhancing the properties of three types of local Iraqi subgrade soils. The comparison of the samples is based on the CBR tests. The AASHTO (1993) flexible pavement design was used to compute the pavement thickness requirements. The soil samples A, B and C have a natural CBR values of 3.8, 3.9 and 4, respectively, on which the physical stabilisers of Powdered rock (PR), grained recycled concrete (GRC), and recycled crumb rubber grains (CR) were employed, while Quicklime (QL) and activated fly ash (AFA) were both utilised as chemical stabilisers. The stabilisation with 15 % of AFA proved to be the most applicable method for soil types A and B for reducing the pavement thickness requirements by 51 % and 32 %, respectively, with a reasonable financial feasibility for both. The same feasibility is proven when stabilising soil type C with 15 % of GRC, which reduces the pavement thickness by 25.7 %.

Keywords: Flexible pavement, AASHTO flexible design method, CBR, physical stabilizers, chemical stabilizers.

1. Introduction

There are several highway pavement distresses, some of which can be attributed to subgrade soils' inadequate support. Such cases often result from the sensitivity to a high-water content, low specific gravity, and low shear strength, along with many undesirable characteristics of highway pavement subgrade soils. Subgrade strength is often assessed by many kinds of tests conducted either in the field or in the lab, tests like the field density and the California Bearing ratio (CBR) value [1].

To achieve an optimal performance of a flexible pavement, the design method must depend on cost effective, proper, and readily existing subgrade layer components. Soft soil in a subgrade layer, for example, needs very special improvements to ensure the suitability for constructing a supporting layer for flexible pavement layers. The process of stabilising subgrade soil is both efficient and cost effective in most cases, because road paving materials are generally less expensive than replacing the existing subgrade with stronger materials [2].

The process of stabilisation could be mechanical, chemical, or a combination of both. The mechanical stabilisation is usually performed by guaranteeing the proper arrangement of soil particles either by compacting the soil layer by vibrations to rearrange the soil particles, or by adopting some advanced methods such as soil nailing with the use of barriers. The chemical methods are usually achieved through the use of a stabilising agent such as cementation substances causing a chemical reaction with soil particles.

In the case of soft natural soil, such as clayey peat, silt or organic soil, the majority of stabilising mechanisms may be used [3]. Fine-grained granular soils are the best for stabilisation. This is due to the huge ratio of the surface area to the diameter of the particles. During such a stabilisation process for soils that has the potential of swelling danger, the physio-synthetic within and around the clay particles . As a result, the treated CL soil showed an increase in the CBR value, which may signify the enhancement of the quality of the subgrade and, consequently, an increase in the carrying capacity of the pavement [4].

Over the last few decades, non-traditional soil stabilising additives have been introduced at a rapid rate. Due to their affordability, quick treatment times, and ease of use, these stabilisers are becoming more popular [5–7].

The aim of this research is to study the effect of soil stabilisation for road subsoil whose resistance strength was measured by a CBR experiment, and to study the effect of this resistance index on the design of pavement thickness by the AASHTO method. Five physical and chemical additives were used – quicklime, activated fly ash, powdered rock, grinded recycled concrete, and crumb rubber.

2. Literature review

The subgrade's quality has a significant impact on the design of the pavement as well as its life time and performance. The highway pavements, which are constructed on problematic soil usually demonstrate poor performance and unpredictable behaviour due to the influence of the subgrade soil type [8]. Shrinkage-driven fissures may be in-filled with sediment over a geological time scale, resulting in subgrade irregularities. It is worth noting that in the field of geotechnical soil stabilisation, the substructure of the paved highway is subject to all the usual soil stabilisation laws. According to Asad et al. [9], who studied the stabilisation of subgrade consisting of low plastic clayey soil (CL), when lime additive is used in a percentage ranging from 0 % to 6 %, then the unconfined compressive strength (UCS) of the stabilised soil increases from 46.08 psi to 103.27 psi. Increasing the percentage of the additive above 6 % decreases the UCS [9]. The explanation of the UCS increase of soil is due to the increased flocculation induced by lime in the treated clayey soil. Many properties of the lime-treated soil were observed to be improved, such as the plasticity index of soil decreasing and the soil type transforming from clay with a low plasticity to silty soil. The swelling of the treated soil is omitted and the soil becomes un-expanded soil. The CBR of the lime-treated soil is increased. This increase in CBR value has the potential to reduce both the cost and total thickness of the multi-layer pavement.

According to Karim et al. [10], who studied the effect of fly ash addition on the geotechnical properties of the soil, which is soft clay. The addition of fly ash lowers the specific gravity of the treated soil because the specific gravity of fly ash is lower than the specific gravity of the soil. The plasticity of the treated soil is reduced. The maximum dry density (MDD) of the soil is reduced while the optimum water content (OWC) of the treated soil is increased, which solves many of the issues with the untreated soil [10]. The UCS of the soil increased with increasing fly ash percentages. The CBR of soil increased from 90.1 % at 5 % fly ash to 538.3 % at 20 % fly ash and after the 20 % fly ash increase, the CBR decreases. Also, the compressibility of the soil decreases. In this study, it was found that 20 % of fly ash is the optimum percentage. Many other studies concluded similar results by the addition of approximate percentages of fly ash [11–13].

Kumar & Biradar utilised the quarry-dust as a physical additive, which has been collected from a quarry at Srikakulam in India. The samples were blended with waste materials at different percentages of which the SG is 2.68, the OMG is 9.3 % and the MDD is 17.02 kN/m^3. It was found that the plasticity of the soil treated by this substance was reduced because the quarry dust is a non-plastic material. The MDD of the modified soil was increased by 5.88 % when adding 40 % of quarry dust. But beyond the 40 % the MDD of soil began to decrease. The CBR of the soil also increased, and after the 40%, it also started to decrease. It was found by this study that the 40 % of quarry dust is the optimum percentage [14].

The use of grained recycled concrete (GRC) as an additive has been proven to enhance the properties of soft soils [15, 16]. Saeed and Rashed assessed experimentally the ability to use demolished waste concrete (DWC) as a mechanical (physical) stabiliser that is added for treating expansive soil geotechnically. The plasticity of the treated soil was reduced as the (DWC) is a non-cohesive material. The swelling potential (which includes both the swelling percentage and the swelling pressure) decreased with the increase in DWC up to 12 %, but above this percentage, no significant decrease in swelling potential was noticed. According to their opinion, both the MDD and the OMC of the soil were reduced because of the presence of fine sand in the substance. The strength of the soil represented by UCS increased up to 12 % of DWC cured for 28 days and the behaviour of the soil changed from flexible to brittle with the increment of this substance. The CBR of the soil treated by 12 % of DWC increased from 4.27 % to 24.14 %. It was concluded by this study that grained recycled concrete (GRC) is economical, environment-friendly, and effective for treating adverse properties of expansive soils [17].

Many researches dealt with the addition of crumb rubber to improve the properties of soft soils in terms of CBR and MR. values and to enhance their support of flexible pavements [5, 18]. Ravichandran et.al. tested the use of crumb rubber grains of waste tires in the stabilisation process of weak soils. It was found that the CBR value of the treated soil increased up to 10 % of tire rubber grains, and above this percentage, the CBR decreased. Increased CBR value of stabilised soil can greatly lower the overall pavement thickness and, as a result, the entire cost of road construction. The permeability of the treated soil denoted by the coefficient of permeability was increased. It was concluded at the end of this study that the use of rubber grains as a stabiliser presents a low-cost stabilisation technology that considerably decreases the current waste tire disposal problem [19].

In this research, five additives are used; quicklime, activated fly ash, powdered rock, grained recycled concrete, and crumb rubber. All these additives are mixed with three soil samples representing the subgrades of three main highways connecting Baquba city. The experimental work is conducted on these mixtures to determine the effect of these additives on increasing the strength of soils in terms of CBR values and, consequently, the expected reduction in highway pavements.

3. Materials used

3.1. Soil

Three samples of soil were used in this study and all of them were extracted from flexible pavement road soil subgrades. They were brought from three different locations at Diyala governorate in the middle of Iraq. The first soil sample (denoted soil A) was brought from the subgrade of Baquba-Khalis highway (Latitude 33° 48′ 27.43″ N and Longitude 44° 35′ 0.32″ E).

Property	**Soil A**	**Soil B**	**Soil C**
Natural water content [%]	40	32	28
Liquid Limit [%]	48	35	34
Plastic Limit [%]	15	15	20
Plasticity Index [%]	33	20	14
Gravel [%]	0	0	0
Sand [%]	0.7	5	15
Silt [%]	38.3	36	40
Clay [%]	61	59	45
Specific Gravity (GS)	2.67	2.71	2.75
USCS Soil Classification	CL	CL	CL
AASHTO Soil Classification	A-7-6 (35)	A-6 (29)	A-6 (11)
Maximum Dry Density [kN/m^3]	17.5	18.6	19.1
Optimum Moisture Content [%]	17.7	16.5	16

Table 1. Properties of the collected soil samples.

The second soil sample (soil B) was brought from the subgrade of Baquba-Al Sabtiya highway (Latitude 33° 47′ 7.59″ N and Longitude 44° 37′ 22.36″ E) . The third soil sample (soil C) was brought from the University of Diyala-Khan Bani Saad highway (Latitude 33° 40′ 29.32″ N and Longitude 44° 35′ 7.66″ E). Table 1 shows some index properties of the collected soil samples.

3.2. Additives

3.2.1. Quicklime (QL)

The type of lime employed in this study was the un-slaked lime, often known as quicklime, which is obtained from limestone. This material was manufactured by the Azerbaijan Lime Chemical Company in Iran. Its particles , determined by a sieve analysis, is 850 microns (sieve No. 20).

3.2.2. Activated fly ash (AFA)

Type F fly ash employed in this study is a soil stabiliser, but it lacks cementation and pozzolanic qualities, which were compensated by adding the Sulfate-Resistant Portland Cement, which is manufactured by Al-Geser manufacturing company in the governorate of Kerbela in southern Iraq. The fly ash used in this investigation was produced in India.

3.2.3. Powdered rock (PR)

This material was obtained from a local quarry in Diyala province by grinding the local sand stone according to the Iraqi specification (2715) [20]. Its particle size, determined by a sieve analysis, is 0.075 mm.

3.2.4. Grained recycled concrete (GRC)

This material was made from the leftovers of concrete cubes that were used for research engineering purposes in the University of Diyala's College of Engineering's Structural Testing Laboratory, where it was crushed in a specific local mill for this purpose. Its particle size, determined by a sieve test, is 0.45 mm. The tested specific gravity of the material was found to be 2.7.

3.2.5. Crumb rubber grains (CR)

For obtaining this material, worn tires were cut into small pieces with a grain size of one to two millimeters in diameter maximum. The specific gravity is 0.91, the compacted void ratio ranges between (0.9–1.3) while the uncompacted void ratio ranges between (1.2–2.4) and Poisson's ratio is 0.5.

4. Experimental work

4.1. Preparation of treated soil samples

In this research, the five above-mentioned additives were added to soil samples (A, B, and C). An optimum ratio of each additive was selected depending on previous researches on similar types of soils in order to enhance their properties in terms of the CBR value [2, 5, 16]. The percentages of these stabilisers were; 9 % of quicklime, 15 % of activated fly ash, 25 % of powdered rock, 15 % of grained recycled concrete, and 4 % of crumb rubber grains [6, 10, 19]. These percentages were added to each soil sample and subjected to the CBR test before and after the addition.

4.2. CBR test

The CBR test is one of the important empirical tests for evaluating the strength of the subgrade soil and one of the input parameters in determining the flexible pavement thickness according to AASHTO design method. This test was conducted according to ASTM D1883-21. The test included the preparation and compaction of the test sample at the maximum dry density and then immersed in water path for 4 days as recommended in the specifications. Then, the samples were extracted from the water and allowed to drain, and then tested using CBR loading machine with a penetration rate of 1.25 mm/min [21].

5. Pavement design

In order to find out the optimal subgrade soil improvement strategy, a test with a unified set of parameters for the flexible pavement was used according to the AASHTO design method [22] and conducted on all soil types included in this study. The design parameters as adopted by the local directorate of highways and bridges Diyala governorate are detailed in Table 2. Table 3 shows the compositions and coefficients of each pavement layer according to its properties.

Parameter	**Parameter's value**
Pavement Lifetime	15 Years
Traffic ESAL (80 kN)	2×10^6
Reliability (R)	99 %
Standard deviation (So)	0.49
Initial Serviceability (Pi)	4.5
Terminal Serviceability (Pt)	2.5
State of Water Drainage	poor

Table 2. The adopted unified design parameters .

Parameter	**Subbase**	**Base**	**Surface**
Materials	Granular soil	Crushed stone	Asphalt concrete
Structural coefficient	a3 = 0.1	a2 = 0.14	a1 = 0.44
Drainage coefficient	m3 = 0.8	m2 = 0.8	–

Table 3. The compositions of pavement layers and coefficients.

The chosen flexible pavement is a three-layered system, which is composed of a wearing layer on the top, a base layer underneath it and a sub-base layer in the bottom. This three-layered system is supported by the subgrade soil. This system is assumed to be fixed, while the impacts of the soil improvements on the total thickness of the pavement is going to be investigated. The results of the calculation of each pavement layer thickness using the AASHTO method can be seen in Table 4 which shows the required thicknesses over each layer of the natural soils before the improvements.

Many relations that correlate the MR value to the CBR value were developed due to the importance of this topic [23, 24]. The following equation is used in this method for the calculation of the resilient modulus (MR) of the subgrade that uses the structural number (SN) of the pavement layer, according to the AASHTO method [25, 26]:

$$\text{MR (psi)} = 1500 \times \text{CBR}, \quad \text{for CBR} \leq 10\,\%. \tag{1}$$

The subgrade soil strength measured with the CBR value before and after treatment changes the bearing capacity values of the subgrade and a new flexible pavement thickness is calculated to investigate the impact of the five improvement techniques on the flexible pavement's total depth before and after the treatment and the percentage reduction for each treatment.

6. Results and discussion

The results indicated that all three low plasticity soil samples A, B, and C having the CBR values of 3.8, 3.9, and 4, respectively, have responded to the stabilisation process. Despite the difference between their CBR values being small, these samples have highly different characteristics for they were brought from different locations as stated earlier. These differences could be noticed in their responses to the stabilisation processes in terms of the increase in CBR values. This increment would result in reducing the road pavement's thickness requirements, and consequently make a financial profit due to the low cost of the stabilisation process as compared to the high cost of pavement construction.

The tests revealed that soil sample A responded very well to the stabilisation processes and the CBR value increased from 3.8 % to 30 % by adding the optimum percentages of AFA, QL, and PR, while the addition of GRC and CR increased the CBR value to 20 %.

Soil sample B also showed an enhanced CBR value, which has increased from 3.9 % to about 19 % by the addition of PR and GRC. A lesser increment in CBR was observed for the addition of other additives, about 14 %.

As for soil sample C, for which the smallest increase was observed, the CBR value increased from 4% to 11% by adding GRC and CR while other additives didn't increase the CBR to more than 7.5 %.

In order to determine the effect of these enhancements in stabilised soils on the pavement thickness, the calculations according to the AASHTO flexible design method were repeated to find out the required total pavement thickness for all treatments for each soil type. The results are shown in Figure 1. At the same time, the financial impact has been determined in which the net profit is calculated by subtracting the cost of the additive's application process from the amount of costs saved due to the reduction of the pavement layer thickness. The financial details are shown in Table 5.

The results reveal that the biggest reductions found for soil A, in which the total pavement thickness requirement is reduced from 39 in to 19 in i.e. 51 %. Lesser reduction can be observed for treated soil sample B, in which the total pavement thickness is reduced

Parameter	Soil A	Soil B	Soil C	Subbase	Base	Asphalt
MR [Psi]	5760	5925	6000	13500	31800	450000
Structural Number SN	6.4	6.2	6	3.8	2.6	–
Total thickness [in]	39	37	35	18	6	–

TABLE 4. Design thicknesses above each layer on natural soils.

Additive	Soil	Stabilization cost [\$/m^2]	Pavement reduction [cm]	Reduction cost [\$/m^2]	Benefit [\$/m^2]	B/C ratio
9% QL	A	3.64	50.8	15.24	11.6	3.19
9% QL	B	3.64	33.02	9.906	6.266	1.72
9% QL	C	3.64	12.7	3.81	0.17	0.05
15% AFA	A	2.26	50.8	15.24	12.98	5.74
15% AFA	B	2.26	30.48	9.144	6.884	3.05
15% AFA	C	2.26	15.24	4.572	2.312	1.02
25% PR	A	7.5	48.26	14.478	6.978	0.93
25% PR	B	7.5	38.1	11.43	3.93	0.52
25% PR	C	7.5	10.16	3.048	-4.452	–
15% GRC	A	2.72	45.72	13.716	10.996	4.04
15% GRC	B	2.72	35.56	10.668	7.948	2.92
15% GRC	C	2.72	22.86	6.858	4.138	1.52
4% CR	A	6.03	45.72	13.716	7.686	1.27
4% CR	B	6.03	33.02	9.906	3.876	0.64
4% CR	C	6.03	20.32	6.096	0.066	0.01

TABLE 5. Financial feasibility analyses.

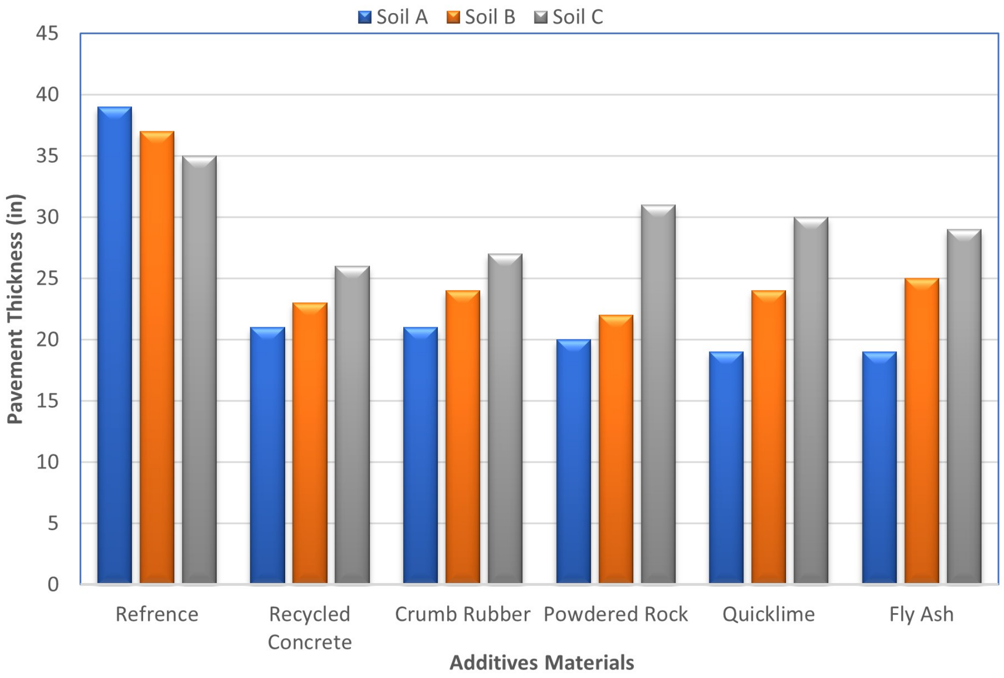

FIGURE 1. Effect of subgrade improvement on the pavement thickness.

by approximately 40 % from 37 in to 22 in. Soil sample type C has the worst results in this regard as the pavement thickness was reduced by no more than 25.7 % from 35 in to 26 in.

These results are very close , if not better, to the improvement achieved by Shubber & Saeed and Amakye et al. [27, 28], the variations in results are mostly due to the type of the treated soil.

The financial analyses showed another sequence of preferences among additives in terms of the benefit to cost ratio. For the soil type A, although; the addition of QL and AFA resulted in an identical pavement thickness reduction, they returned B/C ratios of 3.19 and 5.7, respectively, and, similarly, the addition of GRC and CR resulted in an identical reduction in pavement thickness, yet their B/C ratios were 4.4 and 1.27, respectively. Adding the PR resulted in a 0.93 B/C ratio, which is unacceptable despite its relatively high pavement reduction.

Likewise in soil type B, the highest reduction in pavement thickness was produced by the addition of PR , yet, financially, it is unacceptable due to the B/C ratio of 0.52. the same result was observed for CR, which returned a B/C ratio of 0.62. In this type of soil, the most financially efficient additives are AFA and GRC, yielding B/C ratios of 3.05 and 2.92, respectively.

For soil type C, most of these additives are not financially efficient producing B/C ratio lesser than 1, except for AFA and GRC for, yielding B/C ratios of 1.02 and 1.52, respectively.

7. Conclusions and recommendations

In this paper, three Iraqi local subgrade soil samples were stabilised using five different additives. these samples were tested for the CBR value both before and after the treatment in order to examine the extent to which these additives could enhance the soil support capability for the flexible pavement by utilising the AASHTO flexible pavement design guide. The most important conclusions drawn from the results of this research are as follows:

(1.) All three subgrade soil samples responded well to the stabilisation process, but to a varying extent.

(2.) The best reduction in the pavement thickness was about 51 %, achieved for soil (A) by a stabilisation with 15 % of AFA. At the same time, this process returns the highest financial feasibility.

(3.) The highest reduction in pavement thickness in soil B is approximately 47 %, achieved by a stabilisation with 25 % of PR, but it was found financially unacceptable for yielding a B/C ratio lesser than 1, while the most financial return in this soil is achieved by using 15 % of AFA that returns a 3.05 B/C ratio.

(4.) The smallest response to the stabilisation was observed for soil (C), in which the highest reduction in the pavement thickness is achieved by stabilisation with 15 % of GRC , resulting in a pavement thickness reduction of 26 % and it was proved to have the highest financial return with a 1.52 B/C ratio.

(5.) It is recommended to study the environmental impacts on the stabilised subgrade soils, especially water infiltration, and their effect on road pavements.

List of symbols

GS	Specific gravity
CL	Low plasticity clayey soil
MR	Resilient modulus
UCS	Unconfined compressive strength
MDD	Maximum dry density
OWC	Optimum water content
GRC	Grained recycled concrete
DWC	Demolished waste concrete
ASTM	American society for testing and materials
SN	Structural number

References

[1] H. M. Park, M. K. Chung, Y. A. Lee, B. I. Kim. A study on the correlation between soil properties and subgrade stiffness using the long-term pavement performance data. *International Journal of Pavement Engineering* **14**(2):146–153, 2013. `https://doi.org/10.1080/10298436.2011.633167`.

[2] O. A. Abd-Allah. *The effect of soil improvements on pavement fail-ures along Diyala Governorate Highways*. Master's thesis, 2021.

[3] N. A. Patel, C. B. Mishra, D. K. Parmar, S. B. Gautam. Subgrade soil stabilization using chemical additives. *International Research Journal of Engineering and Technology* **02**(04):1089–1095, 2015.

[4] E. Segun, O. Moses, S. Akinlabi. Geotechnical and microstructural properties of cement-treated laterites stabilized with rice husk ash and bamboo leaf ash. *Acta Polytechnica* **61**(06):722–732, 2021. `https://doi.org/10.14311/AP.2021.61.0722`.

[5] O. A. Abd-Allah, S. H. A. Awn, R. N. Zehawi. Improvement of soft clay soil using different types of additives. *IOP Conference Series: Earth and Environmental Science* **856**(1):012010, 2021. `https://doi.org/10.1088/1755-1315/856/1/012010`.

[6] Z. Al-Khafaji, H. Al-Naely, A. Al-Najar. A review applying industrial waste materials in stabilisation of soft soil. *Electronic Journal of Structural Engineering* **18**(2):16–23, 2018. `https://doi.org/10.56748/ejse.182602`.

[7] J. Vesely. Numerical modelling of the soil behaviour by using newly developed advanced material model. *Acta Polytechnica* **57**(1):58–70, 2017. `https://doi.org/10.14311/AP.2017.57.0058`.

[8] R. Baadiga, U. Balunaini, S. Saride, M. R. Madhav. Effect of geogrid type and subgrade strength on the traffic benefit ratio of flexible pavements. *Transportation Infrastructure Geotechnology* pp. 1–31, 2021. `https://doi.org/10.1007/s40515-021-00203-5`.

[9] A. Asad, A. Hussain, A. Farhan, et al. Influence of lime on low plastic clay soil used as subgrade. *Journal of Mechanics of Continua and Mathematical Sciences* **14**(1):69–77, 2019. `https://doi.org/10.26782/jmcms.2019.02.00005`.

[10] H. H. Karim, Z. W. Samueel, A. H. Jassem. Influence of fly ash addition on behavior of soft clayey soil. *Engineering and Technology Journal* **38**(5):698–706, 2020. `https://doi.org/10.30684/etj.v38i5A.426`.

[11] R. Kishor, V. P. Singh. Evaluation of expansive soil amended with fly ash and liquid alkaline activator. *Transportation Infrastructure Geotechnology* pp. 1–22, 2022. `https://doi.org/10.1007/s40515-022-00240-8`.

[12] A. Thomas, K. Kumar, L. Tandon, O. Prakash. Effect of fly ash on the engineering properties of soil. *International Journal of Advances in Mechanical and Civil Engineering* **2**(3):16–18, 2015.

[13] B. Lekha, G. Sarang, A. Shankar. Effect of electrolyte lignin and fly ash in stabilizing black cotton soil. *Transportation Infrastructure Geotechnology* **2**(2):87–101, 2015. `https://doi.org/10.1007/s40515-015-0020-0`.

[14] U. A. Kumar, K. B. Biradar. Soft subgrade stabilization with quarry dust-an industrial waste. *International Journal of Research in Engineering and Technology* **03**(08):409–412, 2014. `https://doi.org/10.15623/ijret.2014.0308063`.

[15] M. A. Al-Obaydi, M. D. Abdulnafaa, O. A. Atasoy, A. F. Cabalar. Improvement in field CBR values of subgrade soil using construction-demolition materials. *Transportation Infrastructure Geotechnology* **9**(2):185–205, 2022. `https://doi.org/10.1007/s40515-021-00170-x`.

[16] O. Ahmed, S. H. A. Awn, R. N. Zehawi. Improving California bearing ratio (CBR) using chemical and physical treatments for Diyala soils. *Diyala Journal of Engineering Sciences* **14**(2):42–51, 2021. `https://doi.org/10.24237/djes.2021.14204`.

[17] S. B. Saeed, K. A. Rashed. Evaluating the uses of concrete demolishing waste in improving the geotechnical properties of expansive soil. *Journal of Engineering* **26**(7):158–174, 2020. `https://doi.org/10.31026/j.eng.2020.07.11`.

[18] H. A. Hasan, L. H. A. Mohammed, L. G. G. Masood. Effect of rubber tire on behaviour of subgrade expansive Iraqi soils. *IOP Conference Series: Materials Science and Engineering* **870**(1):012066, 2020. `https://doi.org/10.1088/1757-899X/870/1/012066`.

[19] P. T. Ravichandran, A. S. Prasad, K. D. Krishnan, P. R. K. Rajkumar. Effect of addition of waste tyre crumb rubber on weak soil stabilisation. *Indian Journal of Science and Technology* **9**(5):1–5, 2016. `https://doi.org/10.17485/ijst/2016/v9i5/87259`.

[20] Central Organization for Standardization and Quality Control. Technical specifications for civil work, Ministry of Planning/Republic of Iraq, 2017.

[21] American Association of State Highway and Transportation Officials. Standard method of test for the California bearing ratio (AASHTO Standard No. T193), 2013.

[22] American Association of State Highway and Transportation Officials. *AASHTO Guide for Ddesign of pavement structures.* American Association of State Highway and Transportation Officials, Washington DC, 1993. ISBN 1-56051-055-2.

[23] M. Arshad. Development of a correlation between the resilient modulus and CBR value for granular blends containing natural aggregates and RAP/RCA materials. *Advances in Materials Science and Engineering* **2019**:8238904, 2019. `https://doi.org/10.1155/2019/8238904`.

[24] H. R. Heinimann. Pavement engineering for forest roads: Development and opportunities. *Croatian Journal of Forest Engineering:* **42**(1):91–106, 2021. `https://doi.org/10.5552/crojfe.2021.860`.

[25] A. A. Hussein, Y. M. Alshkane. Prediction of CBR and MR of fine-grained soil using DCPI. In *Proceedings of the 4th International Engineering Conference on Developments in Civil & Computer Engineering*, pp. 268–282. 2018. `https://doi.org/10.23918/iec2018.20`.

[26] N. J. Garber, L. A. Hoel. *Traffic and highway engineering.* Cengage Learning, 2009. ISBN 0495082503.

[27] K. H. H. Shubber, A. A. Saad. Subgrade stabilization strategies effect on pavement thickness according to AASHTO pavement design method. (Review). *IOP Conference Series: Materials Science and Engineering* **737**(01):012145, 2020. `https://doi.org/10.1088/1757-899X/737/1/012145`.

[28] S. Y. O. Amakye, S. J. Abbey, C. A. Booth, J. Oti. Road pavement thickness and construction depth optimization using treated and untreated artificially-synthesized expansive road subgrade materials with varying plasticity index. *Materials* **15**(08):2773, 2022. `https://doi.org/10.3390/ma15082773`.

LaTeX class errors and warnings

- **Warning:** Article ‘akka‘ has [eprint] option
- **Warning:** Article ‘aruntas‘ has [eprint] option
- **Warning:** Article ‘can‘ has [eprint] option
- **Warning:** Article ‘carrera‘ has [eprint] option
- **Warning:** Article ‘dacruz‘ has [eprint] option
- **Warning:** Article ‘klesa‘ has [eprint] option
- **Warning:** Article ‘venglar‘ has [eprint] option
- **Warning:** Article ‘zehawi‘ has [eprint] option